The Galactic Center Lobe: New 14GHz GBT Observations

Miles Cannon Blanton

A dissertation submitted to the faculty of the University of North Carolina at Chapel Hill in partial fulfillment of the requirements for the degree of Doctor of Philosophy in the Department of Physics & Astronomy

Chapel Hill
2008

Approved by:

Wayne A. Christiansen, Advisor
Christian Iliadis, Reader
Sheila Kannappan, Reader
Daniel E. Reichart, Reader
James A. Rose, Reader

Abstract

Miles Cannon Blanton. The Galactic Center Lobe: New 14GHz GBT Observations

(Under the direction of Wayne A. Christiansen)

Outflows from nuclear winds are observed in dozens of galaxies and can have profound effects on galactic evolution and the state of the intergalactic medium. Nuclear winds may have different origin mechanisms, such as starbursts or accretion on the central engine, but regardless of how the energy is deposited into the nucleus, outflow from the expansion of very hot gas can result in a wind-blown superbubble. Periods of previous outflow in our own Galaxy have resulted in several structures interpreted as superbubbles; the Galactic Center Lobe (GCL), a 150pc-scale open, omega-shaped projection perpendicular to the Galactic Plane, more-or-less centered on the Galactic Center, is one such structure.

We have observed the GCL at 14GHz (2cm) with the Robert C. Byrd 100m Green Bank Telescope (GBT) with the original intent to obtain a more definitive constraint on the energetics of the GCL, but in the course of our observations have concluded that the 'walls' of the GCL itself are composed of two likely unrelated structures. We reduce and analyze new GBT data with new software and use a novel filtering technique to analyze existing multi-band data from the Nobeyama Radio Observatory 45m telescope, the NRAO Very Large Array, the Spitzer Space Telescope, and the Chandra X-ray Observatory. We propose that the nuclear outflow is manifested not in both spurs of the GCL, but in the western spur of the GCL and a new structure observed above the SgrB-complex. Additionally, the eastern wall of the GCL is interpreted as a jet-like extension of the Galactic Center Arc, and is seen to be interacting with the Double Helix Nebula in a manner inconsistent with a limb-brightened shell wall.

Acknowledgments

I would first like to thank my advisor, Dr. Wayne Christiansen, whose patience, insight, guidance and patience were invaluable to me in writing this thesis. He has helped me to start into this brave new world of research and radio astronomy. My thanks also to Dr. Jacqueline van Gorkom, who oversaw my first foray into astrophysics.

I would like to thank those individuals who contributed their advice (and sometimes their data) to helping me: Dr. Yoshiaki Sofue, Dr. Fared Yusef-Zadeh and Dr. Q. Daniel Wang for providing me with their original data for me to look at and include in this thesis and providing me with their thoughts about it's content; Dr. Lawrence Rudnick without whose filtering technique, and wise advice on applying it would have made this thesis far less interesting.

Thanks to my 'friends' at the GBT: Dr. Frank Ghigo, Dr. Tony Minter, and Dr. Jay Lockman for their help in wrangling the telescope and its data products.

I would also like to thank all the telescope operators at the GBT with whom I worked: Kevin Gum, Eric Knapp, Greg Monk, David Rose, Barry Sharp and Donna Stricklin, for not letting me break their telescope, and for showing me how to get snow off the darn thing from Chapel Hill!

To my parents, John & Eileen and Sallie, for raising me, loving me, and in particular my Dad for teaching me about gravity at age 10, when otherwise I would not have written this thesis.

To my other parents, Doug & Melva, for supporting me these last few years with food and love, and especially for giving me their most precious gift, their daughter.

To my wife, Nichole, for loving me and helping me stay on this trajectory.

Miles Cannon Blanton
July, 21 2008

Table of Contents

List of Figures

Chapter 1

Introduction

Outflows from nuclear winds are observed in dozens of galaxies. They have high energetics: $10^{54} - 10^{61}$ ergs or so. They are of importance for general galaxy evolution and the state of the intergalactic medium. Specifically, they may regulate the growth of bulges and "moderate the evolution of dwarf satellites" (Bland-Hawthorne & Cohen, 2003). These galactic winds may also be responsible for the early enrichment of the halo and outer disk of galaxies, and may account for the observed abundances in the thick disk and globular clusters. Most galactic outflows are "unambiguously active galactic nucleus (AGN) or starburst driven" (Veilleux *et al* 2005).

Galactic winds from the center of galaxies typically sweep out the local ISM. The classic signature of the nuclear winds is minor axis outflow of material; typically there is filamentation. They transport metal-enriched gas out of the galaxies, which may affect the chemical evolution of dwarf galaxies. They may also be responsible for reheating the IGM and enriching the ICM. Nuclear winds are a 'feedback' mechanism between star formation and the content of the ISM.

AGN outflow energy comes from the accretion of matter on the central black hole ranging in mass accretion rates of a fraction of a solar mass per year ($\sim 0.001 M_{\odot} \cdot yr^{-1}$ for low-luminosity AGNs), to about a solar mass ($\sim 1 M_{\odot} \cdot yr^{-1}$ for Seyfert galaxies) to more than 100 solar masses ($\sim 100 M_{\odot} \cdot yr^{-1}$ for quasars and powerful radio sources). Much of the energy generated may be funneled into the outflow. AGN winds are detected along the minor axis of the accretion disk, which is not necessarily perpendicular to the galactic disk (in disk galaxies). Magnetic phenomena almost certainly play a role in collimated outflows, although outflow from some 'radio quiet' galaxies are "loosely collimated and barely relativistic" (Veilleux *et al* 2005).

Starbursts are thought to be a possible driving force for nuclear galactic winds, and overlap

with the energetics of AGN ($10^{54} - 10^{58}$ ergs) (Stickland & Stevens 2000). Starbursts are periods of intense star formation in relatively short periods of time ($\sim 100 Myr$). Galaxies with highly active star formation may reasonably be expected to have high supernovae rates. As a result, a strong wind driven by multiple supernovae can arise in active regions (Chavalier & Clegg, 1985). Starbursts are important for galaxy evolution and formation, and also important for a wide variety of sizes of galaxies (indeed probably all). Similarly, they enrich the IGM because of mixing with the enriched contents of the winds from rapid SN turnover in starbursts and high mass stellar winds.

Starbursts must be sufficiently energetic to develop a supersonic wind. Typically, the supernovae rate must be sufficiently rapid, and the region sufficiently small, to cause a supersonic shock in the ambient matter density. The interaction with such a wind by orbiting clouds can result in streamers (filamentary structure) and X-ray emission (Chevalier & Clegg, 1985).

The SB(s)c galaxy NGC 3079 is one such galaxy observed to have a figure-8 pattern of radio structure and numerous optical filaments interpreted as a bi-conical outflow. The NGC 3079 bubble rises about 1.3kpc (15") above the galaxy's disk. Cecil *et al* (2001, 2002) observed NGC 3079 with the HST and the VLA and independently (in the two wavebands) determined that the superbubble was lofting gas out of the galaxy in a vortex. The superbubble is seen to have both a jet component and the signature of a nuclear wind, though it remains unclear if the wind is due to a starburst or the AGN. The observed filaments are likely the shock fronts between the unshocked ISM and the shocked wind.

In M82 (NGC 3034, an irregular disk galaxy), optical knots and filaments are observed to radially extend out from the disk, along its minor axis: a super-bubble. However, the filamentation is asymmetrical; the northern side of the optical filaments has a large opening angle, while the southern side is more collimated. This asymmetry is thought to be from the starburst being out of the plane of the galaxy, "slightly" (Shopbell *et al*, 1998). There is an extensive X-ray halo, and central X-ray emission that correlates with the asymmetric optical filamentation.

Regardless of the mechanism of energy deposition at the nucleus of a galaxy, the central energy source creates a bubble of very hot gas. The mechanical pressure overrides the ambient ISM pressure and creates an expanding bubble. The outflowing wind from the nuclear activity interacts with the ambient medium and any infalling material, forming a shockwave at the interface. If the energy is sufficient and/or the escape velocity of the galaxy is small enough then the wind-driven shockwave can escape from the galaxy. In gas-poor galaxies (or those with powerful central

sources), the bubble can expand well beyond the host galaxy, while in gas rich galaxies, the bubble may stagnate and collapse in too short a time to be seen.

In elliptical galaxies lacking extended disks, the nuclear winds will be uncollimated (c.f. Williams & Christiansen, 1985). In a disk galaxy, such as our Galaxy, the matter distribution falls off away from the disk. A nuclear wind will thus expand up out of a disk galaxy. Schiano (1985) provides a consistent dynamical framework for the structure of such a nuclear wind in a disk distribution of ambient, pre-blastwave material. There are five layers to Schiano's model: 1) the freely expanding central zone where the energy is deposited into the bubble, 2) the supersonic wind where the expansion into the exponential atmosphere pushes out into the ambient ISM perpendicular to the galactic disk, 3) the interface between the supersonic wind and the shocked ISM, 4) the thin shell of shocked ISM, 5) and the pre-shock, ambient ISM.

Many galaxies are observed to have dumb-bell shaped galactic scale outflows, and have been interpreted as bipolar cylinders, galactic scale jets, etc. Sofue (2000) interprets a similar structure in our Galaxy as evidence for outflow. The North Polar Spur (NPS) (along with its western and southern components) draws a large, dumb-bell (or hourglass) shape fluted at the galactic center. Sofue (2000) finds a bipolar hypershell model for the NPS that is consistent with an impulsive energy injection at the GC of about 10^{55-56} ergs lasting a few Myr or less occurring about 15Myr ago. This is the energy of about 10^5 Type II supernovae.

Furthermore, Sofue (2003) also suggests there is evidence for at least three recent outflow events in the last $10^5 - 10^6$ yrs in the Galactic Center Arc region and another event about 2×10^6yrs ago associated with the Galactic Center Lobe (the GCL, which is the focus of this thesis). Longer lived shells (e.g. much larger observed extent) reasonably require higher energies for their production ($\sim 10^{51}$ ergs for the smaller, newer events and up to 10^{56} ergs for super-large-scale shells), however, older shells may not be the result of just one event, but the accumulation of multiple events, reinforcing each other.

1.1 The Galactic Center Lobe (GCL)

The Galactic Center Lobe (GCL) is a radio feature located at the center of our Galaxy. It is about 1 degree in diameter with an open omega-shaped extension galactic north of the plane of the Galaxy. The GCL was first described by Sofue & Handa (1984), observed at 10.5GHz with the 45-m Nobeyama radio telescope. It is centered in galactic coordinates around (l,b)=(359.7,0.5), with each spur (the East and West spurs) centered at around l=360.2 and l=359.4 respectively

(see Fig. 1.1). The GCL was interpreted as having the same profile as a compressed shell, similar in form to observed energetic or explosive galactic outflows. The integrated flux density above $b \geq 0.2$ is 132 ± 10 Jy, and was observed to have an overall spectral index ($S \sim \nu^{-\alpha}$) compared to 5GHz, of about 0.1 when the diffuse non-thermal (α between 0.6 and 1) had been removed. Sofue (1985) interprets the GCL as HII gas at 5000K with a mass of $4 \times 10^5 M_{\odot}$.

The proposed models for the creation of this structure were: 1) a limb-brightened shock formed by a point explosion (Sofue 1984); 2) a magnetic "bubble" formed from expelled and twisted poloidal fields that loft plasma above the plane (Uchida *et al* 1985), (Shibata 1989); 3) a 'mini' nuclear jet, now quiescent, typically observed in AGN (Sofue *et al*, 1986).

Spectra observed of the assumed black hole at the Galactic Center, Sgr A*, result in a degeneracy of emission models (Malie & Falcke, 2001), but one such model indicates that emission from infalling gas, well below the Eddington limit, would result in mass-loss from a wind. Or else the accretion could lead to a jet, the infalling plasma would emit weakly, but would contribute to the outflow mechanism which emits strongly (esp. in X-ray). Sgr A* could be interpreted as a weak AGN where accretion ($\dot{M} \leq 10^{-8} M_{\odot} \cdot yr^{-1}$) powers the outflow.

Sofue's model (Sofue, 1984), followed earlier work by Kompaneets (1960) whose analytic theory for blast waves from point explosions in exponential atmospheres is a classic in the literature on the hydrodynamics of strong shocks. The Kompaneets/Sofue solution naturally results in an omega shaped shock envelope similar in form to the GCL. The cross-sections of the 10.5GHz GCL images suggested a shock compressed shell structure, i.e. a limb-brightened shell. Sofue (1984) derived an energy requirement of 10^{54} ergs to form the GCL, consistent with the energy available from the nuclear activity in a spiral system from Oort (1977), and an age of 2×10^6 yrs.

Uchida *et al* (1985) suggest a magnetohydrodynamic mechanism combining the effect of the rotating galactic center disk and the strong magnetic field at the center. As the disk rotates, and matter falls into the central regions, a poloidal magnetic field builds that "relaxes" out of the plane, taking plasma with it. Shibata (1989) performed more detailed simulations of this "sweeping-magnetic twist mechanism" and claimed that it agreed well with the morphology of the initial 10.5GHz observations and also adequately explains the observed magnetic structure in the Galactic Center Arc (GCA).

Also, Sofue (1985) noted that a poorly collimated jet would not produce the limb-brightened spurs peaked on either side of the GC, but rather a solid cylinder (or similar geometry). Of course, a combination of effects could be responsible for the GCL.

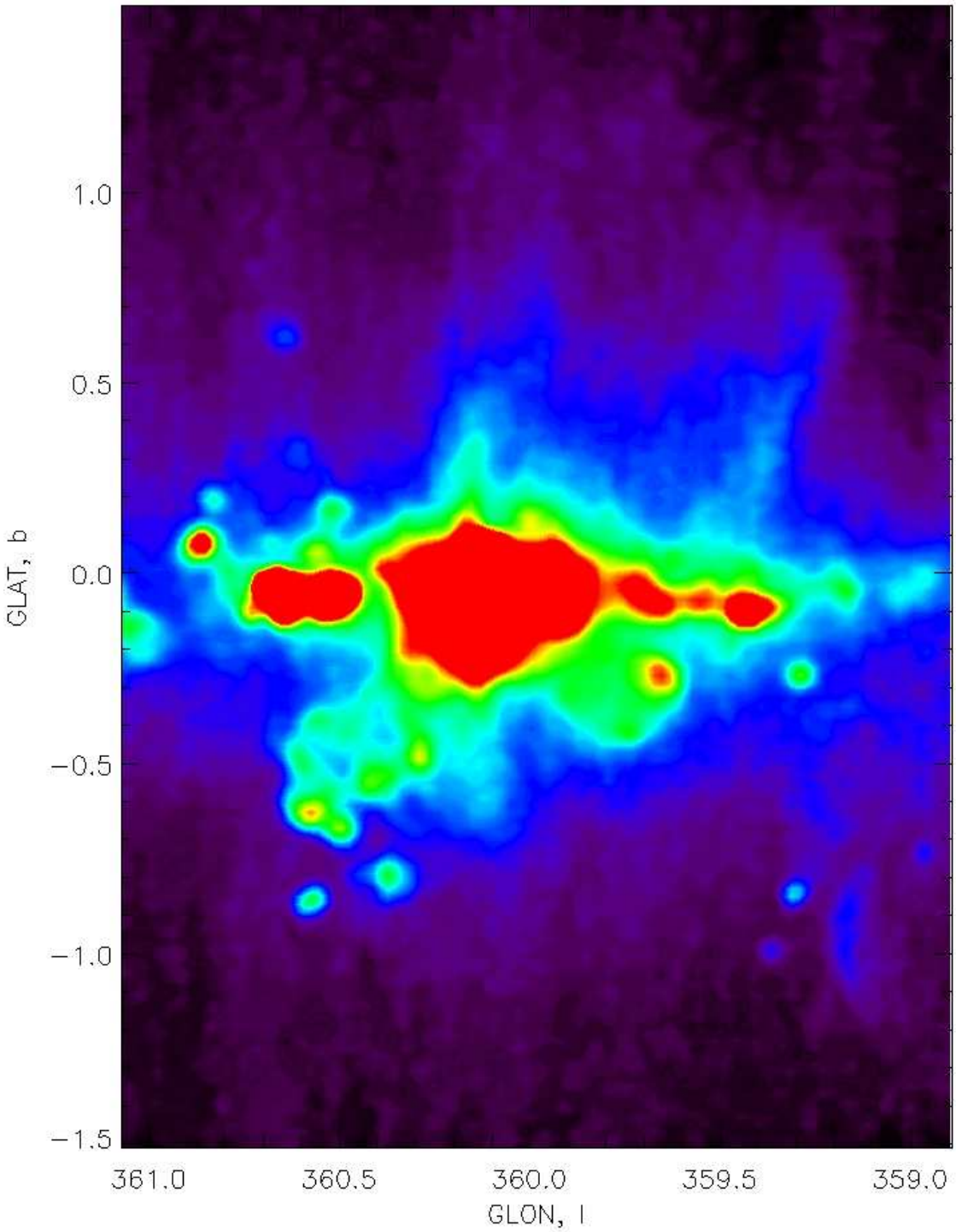

Figure 1.1: A false color image of the 10.5GHz Sofue image, the stronger emission from the core have been omitted to reveal the diffuse emission of the GCL

However these early models of the origin of the GCL failed to explain some inconsistencies with the observed structure of the GCL, namely the markedly different characteristics of the East and West spurs: the asymmetry of their locations relative to the Galactic Center, the lack of a southern galactic counterpart, the correlation with neighboring structures in the mid-infrared, and their spectral differences.

For example, the East and West spurs exhibit different spectral and polarization characteristics. The East spur has a non-thermal spectral index, and upwards of 40% polarization in radio (Tsuboi *et al* 1986). It also seems to be a hot-bed of magnetic interactions with the Galactic Center Arc. The West spur has a flatter, more thermal spectral index, near zero polarization and no obvious interaction with any galactic plane features. Furthermore, and perhaps most importantly, the East spur is three time closer (in projection) to the Sgr A complex than the West spur.

Earlier observations of the GCL in other wavebands did not detect much structure (e.g. Reich *et al*, 1987). However, Bland-Hawthorn & Cohen (2003) Midcourse Space Experiment (MSX) observations, at $8\mu m$, evoked an association between mid-infrared filamentary structures configured similar to the GCL: northward projecting spurs of IR emission, perpendicular to the galactic plane, more-or-less coincident with the spurs of the GCL. However, the resolution of the Sofue maps made it difficult to clarify the closeness of this association. Our original motivation for observing the GCL with the Green Bank Telescope (GBT) was to obtain better, higher frequency, higher resolution radio maps observed to complement the MSX maps, and recent low-frequency Very Large Array (VLA) maps as well. We hoped to obtain a more definitive constraint on the non-thermal synchrotron emitting populations in the 'spurs' and thus study the possible sites of particle acceleration and/or re-acceleration within the presumed shocks from the nuclear wind.

However, during the course of our studies a large quantity of high resolution Spitzer Space Telescope (both IRAC and MIPS instruments) and Chandra X-ray Observatory survey images also became available. As a result we now have evidence from merging the recent IR data with our own GBT images that the spurs of the GCL are indeed very different from one another, and likely have different creation mechanisms and histories, dictating that a new model of the GCL structures be explored.

1.2 Structure of this thesis

In this thesis we will present (ch.2) our new radio observations of the GCL with the GBT at 14GHz, along with a description of new software developed to reduce our GBT data. A novel

filtering technique developed by Rudnick (2002) is explored that is useful in removing atmospheric interference in our GBT observations and enables a re-analysis of the original Sofue 10.5GHz data. The results of our 14GHz map of the GCL are presented in ch.3 along with the results of the new analysis of the original Sofue data. We find that this filtering technique, when applied to Sofue's data, brings out new features that were not previously seen in his image map. In ch.4 pertinent archival and current data taken by others of the GC region are described and the important features relevant to our discussion are described. In ch.5 the correlations (or anti-correlations) between features in our GBT map (and Sofue's filtered map) and the relevant mid-infrared, radio and X-ray data are discussed. In ch.6 a new model for the Galactic Center Lobe that is more consistent with current observations than with previous models is explored. The new model addresses the inconsistencies between the East and West spurs of the GCL, and proposes an identification for a new feature discovered in the filtered Sofue map associated with the SgrB-complex. Ch.7 summarizes our work, and looks to the future.

Chapter 2

GBT Observations and Data Reduction

The GCL was observed with the 100m Robert C. Byrd Green Bank Telescope (GBT) located at the National Radio Astronomy Observatory (NRAO), in Green Bank, WV. According to the GBT website (http://www.gb.nrao.edu), this is "the world's largest fully steerable single aperture antenna." The GC was observed in January and March, 2007 and again in January 2008. We used the Digital Continuum Receiver (DCR) backend, and the Rcvr12_18 frontend (the Ku-Band receiver), centered at 14.075GHz with a band-width of 3.05GHz.

The data were taken in the RALongMap setting, which raster scanned the map in the direction of the Galactic Longitude (with the exception of our final observing epoch, where we added DecLatMap in order to basket weave, see below). We observed 11 separate days (epochs), with the final day in January 2008, which was a make-up day due to poor weather (see Table 2.1 for details). A typical observing regimen included atmospheric tipping scans at the beginning and end of each approximately 3 hour observing block, a primary and secondary calibration scan before and after observing the GCL, and the raster scan mapping of the particular segment of the GCL. On days where we had as much as six hours to observe, calibration and atmospheric scans were run twice through to minimize the time between calibration and tipping scans and the changing atmosphere.

The GBT supports very little software in service of data reduction for continuum and/or mapping procedures. The primary data reduction software is GBTIDL (http://gbtidl.nrao.edu/), however, it does not support continuum reduction nor any mapping, or imaging routines.

Table 2.1: Table of Observations, GBT 14GHz

Scan No.	Date	Int. Time	Duration (on source)
01	12/31/06	0.7 sec	1.5 hrs
02a	01/01/07	0.7 sec	0.9 hrs
02b	01/01/07	1.4 sec	0.4 hrs
03	01/03/07	1.4 sec	1.7 hrs
04a	01/04/07	1.4 sec	1.3 hrs
04b	01/04/07	1.4 sec	0.9 hrs
05	01/06/07	1.4 sec	1.5 hrs
06a [1]	01/12/07	1.4 sec	0.6 hrs
06b	01/12/07	1.4 sec	0.6 hrs
07	01/17/07	2.1 sec	1.1 hrs
08	01/18/07	2.1 sec	0.8 hrs
09 [2]	01/23/07	2.1 sec	N/A
10a	03/09/07	2.1 sec	1.2 hrs
10b	03/09/07	2.1 sec	1.0 hrs
101a	01/21/08	2.1 sec	2.2 hrs
101b	01/21/08	2.1 sec	2.2 hrs

[1]Same area as 06b, but with different parameters, we used the data only from 06b
[2]This day was lost to snow

Because of this lack of in-house software support, all the reduction software (except FITS file interfacing) were written by the author. To accomplish this task, I have taken an organic approach to writing the software. That is, I determined what was theoretically necessary to reduce my specific data and then wrote specific routines, not general reduction/analysis software. What follows is a description of the primary reduction and analysis routines that I wrote to interpret our GBT data and produce images and information from that data.

2.1 Reduction of GBT data and Software developed in IDL

2.1.1 SDFITS

The first step immediately following the observation was to convert the suite of fits-file data into a single-dish (SD) format. The internal NRAO program SDFITS is used to convert the suites of fits-files into SDFITS format. The SDFITS program compiles the numerous fits-files into a single compact file in *.SDFITS format. This format is convenient, compact and more readily usable by a variety of reduction programs. The GBT supports their own IDL-based reduction software, GBTIDL. The current version (as of this writing v. 2.3.1) does not have routines for continuum reduction and analysis, nor for On-The-Fly (OTF) mapping, such as my data. However, they incorporate the complete "IDL Astronomy User's Library" (http://idlastro.gsfc.nasa.gov/homepage.html), and a few routines for accessing, reading, and listing continuum OTF SDFITS data. As such, it is a

useful starting point for the routines I have written in IDL to reduce our data.

2.1.2 The Raw Data

All routines referenced henceforth are developed by us for this research. The first step in the reduction was to access and read into arrays the raw data and any corresponding time and coordinate data that is stored in the SDFITS file for each epoch of observing. The SDFITS file is arranged so that each data row contains the raw data of each raster scan of the map. The routine CONTGEN (for generic continuum data set), first opens the SDFITS file of a selected day of observing, reads the data size of each scan in the 'day' and creates 2 dimensional arrays to put the raw data into. CONTGEN only selects from the SDFITS file those data sets corresponding to the map itself; PEAKING and TIPPING are counterparts to CONTGEN for the peak scans and the tipping (calibration) scans respectively. CONTGEN calls the function CONTSIGREF2 to populate the data arrays. It selects each of the 8 channels of signal data (see below), and the coordinate/time data. The coordinate/time data are the galactic longitude and latitude (calculated inline with the raw data stream at the GBT backend), and the Alt, Az, Local Sidereal Time (LST) and Mean Julian Day (MJD) for each data point. CONTGEN then calls the function COORDCORRECT to calculate the RA and DEC values for each data point. RA and DEC are calculated directly from the Alt/Az and time/LST data points. An alternate calculation of the galactic coordinates is then calculated from these RA/DEC values. This alternate calculation of the galactic coordinates is done in order to calculate the galactic coordinates for the 2nd, offset, beam. The Ku-band's 2nd beam(2nd receiver) is offset from the 1st by 5.5 arcminutes in azimuth (+5'.5). Thus the inline calculation for galactic coordinates do not apply to the 2nd beam. Since the map is a raster scan, the raw data has every alternate row in reverse order relative to its neighboring rows. So, CONTGEN then invokes the function COLSWITCH, which reverses alternate rows starting with the second row of the data set; the reversal applies to any data array, whether image data, coordinate data, etc. In the raw data, the galactic longitude is centered on l=0, so that there are negative and positive longitudes. CONTGEN also moves this centering to l=360, so the data ranges from l$\sim$359 to l$\sim$361. This eliminates any mathematical concerns involving the negative sign and makes it easier to wrap the longitude coordinate for plotting. Finally, CONTGEN saves the intensity data in an 8-channel data cube array, and the coordinate data in a 10-channel data cube array for the coordinate/time data.

2.1.3 Noise-Diode Calibration

The next step is to calibrate the signal data against the injected noise calibrator. The data stream consists of two beam inputs (one for each received [beam]) and two circular polarizations (RR and LL). There is a noise diode for each beam, and the noise diode is switched in equal time between ON and OFF during an integration step. Thus there are 8 total channels of data (see Table 2.2).

Table 2.2: 8-channel data cube

Channel Name	Beam	Polarization	Noise Diode	T_{cal}
ONRR1	1	RR	ON	2.30K
OFFRR1	1	RR	OFF	-
ONLL1	1	LL	ON	3.01K
OFFLL1	1	LL	OFF	-
ONRR2	2	RR	ON	2.16K
OFFRR2	2	RR	OFF	-
ONLL2	2	LL	ON	3.26K
OFFLL2	2	LL	OFF	-

Each beam/polarization channel has its own noise diode with known noise between 2K and 4K. The noise temperature is stored in the SDFITS file. The program CALIB is used to calibrate the intensity counts and convert them into calibrated temperature data (in K). The calibrated data is calculated from the following formula:

$$T = (0.5) \times T_{cal} \times ((cal_{on} + cal_{off})/(cal_{on} - cal_{off}) - 1). \tag{2.1}$$

The difference between the signals with and without the noise injection is the scaling factor between the response of the system (in counts) to the known noise source. This factor is multiplied by the average signal, then half of the noise calibrator temperature is subtracted off. This is done to the tipping and peaking scans as well by, respectively, CALIBTIP and CALIBPEAK. The polarization data sets are then combined as a linear average:

$$T_{tot} = (0.5) \times (T_{LL} + T_{RR}). \tag{2.2}$$

2.1.4 The Atmosphere

Atmosphere removal and system temperature are handled in a single step, first the background temperature of the atmosphere is modeled and subtracted from the source images. The atmospheric temperature model is derived using the routines TIPFIT and MIXTIPFIT. Before and after each day's image scan (with the exception of day 2b due to horizon limits) a tipping scan

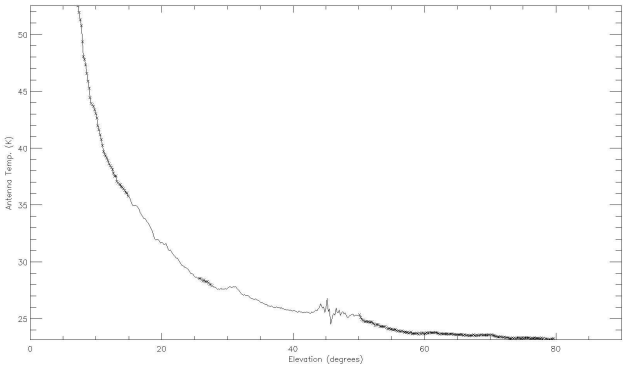

Figure 2.1: The 'Tipping-Scan' from the first day of observing, the regions used for atmospheric modelling are shaded. Note the terrestrial sources between about $30° - 50°$, these are removed in every tipping scan.

was performed which scanned the sky from near zenith ($\sim 80°$) to near horizon ($\sim 5°$). A section of the sky was selected to be free from large known radio sources (e.g. the Sun, Cas A, etc.), however, this is not very important because the tip scan was done in about 5 minutes therefore there was little time to accumulate flux from extra-atmospheric sources. There were, however, local, terrestrial phenomena. This can be observed consistently at around $30° - 50°$ of elevation in each of the scans (see Fig. 2.1). Additionally, as can be seen in Fig. 2.1, even near zenith (90° elevation), there is a system (baseline) temperature of about 24K for the day and scan shown. The system temperature is determined and included in the atmosphere model. From the tipping scans, a model of the effective temperature of the atmosphere before and after the image scans was made. As with the source data, the tipping scans were switched between the sky and the noise injected sky so that temperature calibration could be done. The temperature versus elevation was calculated, with the obvious terrestrial sources flagged from the data. As most of the observations were performed near sunrise, it was expected that the overall atmospheric temperature would change over the course of the observations. For each image scan a matte was made of the modeled contribution to the temperature data from the atmosphere as a function of the elevation of each image pixel. The matte was further modeled by applying a linear interpolation between the tipping models before and after the image scans. A linear extrapolation model was used to approximate atmospheric changes between the two tipping scan times. The matte is essentially an image of the modeled atmosphere over the same coordinate range as the image map. The matte was then subtracted from the image data.

2.1.5 Flux Calibration

The units of the noise-calibrated signal are now in K/beam (the Ku-band GBT feed's beam at 14GHz is ∼54"). Therefore flux calibration is a straightforward measurement of a known flux

calibrator with the telescope before and after the scans of the target source. The calibrators were observed before and after the target source to measure and account for any drift in the system. The calibrator used was the VLA calibrator source 1743-038 (B1950 coordinates). This is a compact radio source, but its flux drifts over a long period of time. The stated flux in the VLA calibrator manual is 3.8Jy. However, the online VLA calibrator manual has a JAVA applet that plots the most recent measurements for a desired calibrator. This applet states that the flux has ranged between about 6.5Jy and 4.2Jy between February 2006 and March 2007. Though in early 2007 is seemed to stay stable at about 5.5Jy. So, unfortunately, flux calibration could not reliably be done for this initial set of observations, however, relative fluxes from point-to-point in the map would be reliable as temperature (K) fluxes. Additionally, more reliable flux bootstrapping was done with the final epoch observing the 'HotSpot' (see below).

2.2 Reduction of the 'HotSpot' Observation

All of the data above b=0.5 was unusable due to poor weather when the data were taken. However, there was an interesting hotspot at the north edge of the observable image of the GCL-E. We chose to use our 'make-up' time to better observe this structure, and to experiment with 'basket-weaving' to help remove atmospheric effects.

The 'HotSpot' observation, taken in January 2008, is of a smaller patch of the overall image, where the GCL-E appears to deviate from its path. The region was scanned twice, once in the Galactic Longitude direction (like the rest of the overall map) and then again in the Galactic Latitude direction. This 'basket weaving' was done to get better signal-to-noise and also to help eliminate scanning effects that are so difficult to deal with in the overall map. Tipping and calibration scans were performed (with different calibrator sources than the overall map, since 1743-038 was variable over this time period); the RALongMap scans were made (in Galactic Longitude), then the tipping and calibration scans were repeated, followed by the DecLongMap scans in Galactic Latitude, ending with another round of tipping and calibration. This was done to have consistent tipping and calibration scans before and after each map of the same region.

Because the observing procedure was different than the overall map, the reduction procedure is a little different. Data packing and noise-diode calibration are the same, excepting that different calibrator sources were used. For undetermined reasons, the model atmosphere obtained by modeling the emission of the tipping scans as a function of airmass, was louder in the elevation range than the mapped data itself. In other words, the atmosphere where the tipping scan was

taken was louder than the region of the sky where the data was taken. So, for this reason, in the HotSpot region, instead of modeling the atmospheric emission as a function of elevation (or airmass), a line is fit to the smoothed data of airmass-to-intensity. The data were smoothed to a 20 pixel 2D Gaussian (compared to the map being about 60 pixels in extent). This is essentially a self-calibration procedure that uses the data itself to model the atmosphere. This model was subtracted from the data.

Prior to combining the images, further scanning and atmospheric effects were removed using a novel filtering algorithm developed by Rudnick (2002), the power of which is summarized below.

2.2.1 Rudnick's filtering technique

As is often the case in astronomy, astronomical images may contain information at many resolutions; a small-scale structure may be embedded in a variable background emission. It is instructive to study these structures separately. To this end an algorithm has been developed by Rudnick (2002) to separate (at arbitrary scales) small-scale and diffuse structure into two images, which have the property that they sum to the original image. This algorithm (hereafter referred to as Rudnick's Filtering Technique, RTF) combs an image, pixel-by-pixel, and replaces each pixel with the minimum value in a specified window around the image, created the 'eroded' image. This image is then scanned again, pixel-by-pixel, to find and replace each pixel with the maximum value in the filter window. This is referred to as 'dilation', and the dilation of the eroded image is called the 'open' image. The 'Filtered' image is defined as the original image minus the 'Open' image. The 'Filtered' image only contains structures that are smaller in scale (approximately) than the window used, and the 'Open' image only contains structures that are larger in scale (approximately) than the window used. The sum of the 'Open' and 'Filtered' images is the original image. The RFT is demonstrated in Fig. 2.2.

We have also used Rudnick's filtering technique to remove point sources in lieu of point-spread-function techniques. If the window used is sufficiently small (say 1 to 3 pixels), and the pixelsize of a typical point source is approximately the same size as the window used, then an application of RTF will result in an 'Open' image that is remarkably point-source free. In this case, if there are small-scale, but NOT point source structures present in the image, the 'Open' image will still retain the small-scale structure, but be free of point sources. This has been especially useful when analyzing the very high resolution Spitzer IRAC images for this thesis. In the following figure we show the application of Rudnick's filtering technique to the 8um Galactic Plane survey image

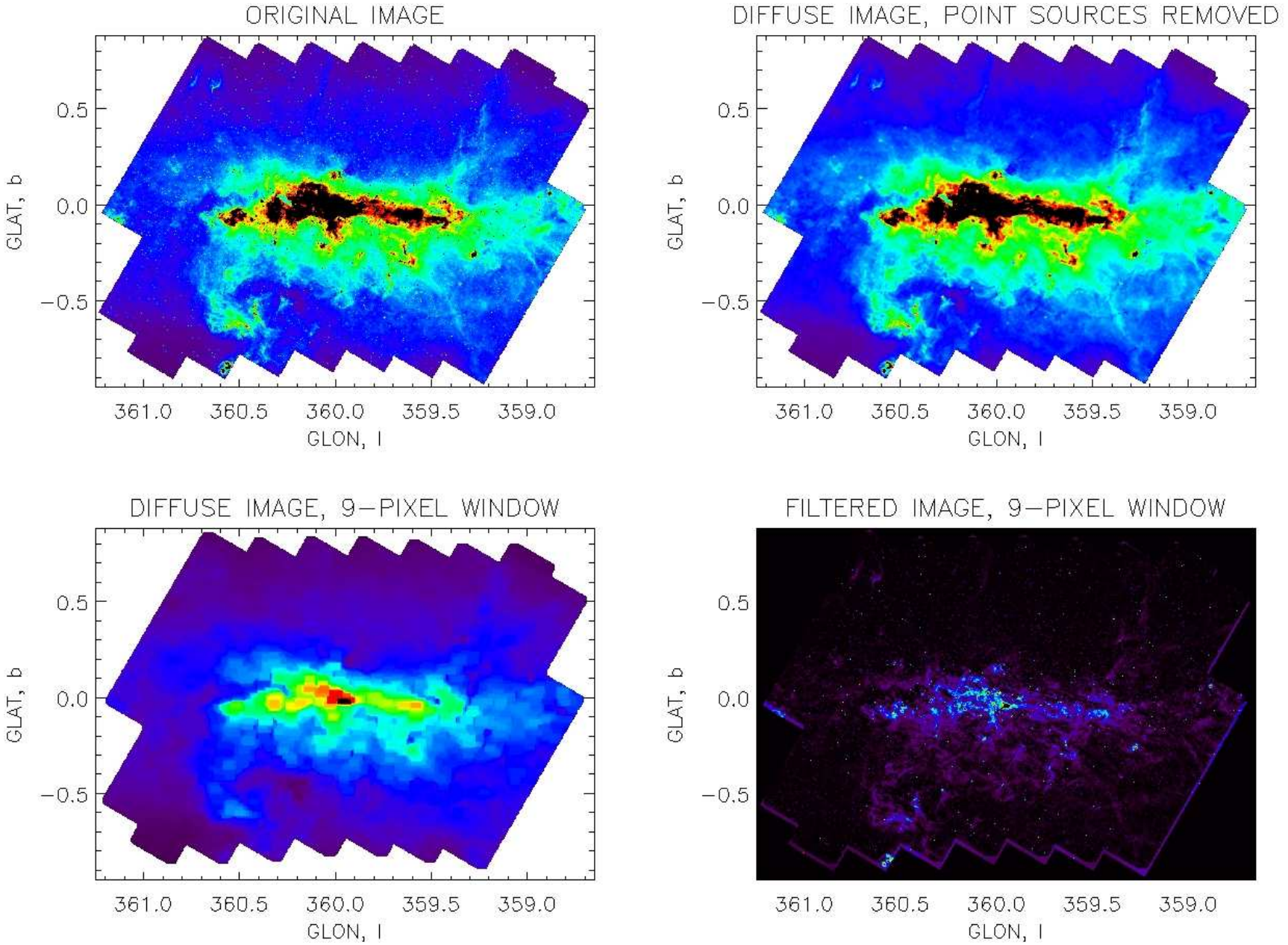

Figure 2.2: The Rudnick Filtering Technique (RFT) in practice. (top left) the original Spitzer 8 micron GC survey image. (top right) filtered with N=9 pixel (3.6 arcsec) radius window, open image (diffuse structure). (bottom left) filtered image showing fine structure. (bottom right) using a much smaller radius (N=1) to semi-remove point sources in lieu of PSF removal.

taken with Spitzer's IRAC instrument by Stolovy *et al* (2006). The top left image is the original image, the top right image is the 'Open' image and the bottom left image is the 'Filtered' image. A window of radius 9 pixels was used (corresponding to about 3.6 arcsec in the image). The final image (bottom right) is the original image filtered with a window of radius 1 pixel, to mostly remove point sources from the image. Rudnick's filtering technique is applied via the routine: RFILTER.

2.2.2 Combining 'HotSpot' images

The separate images of the HotSpot region were then filtered using Rudnick's filtering technique to remove additional scanning and atmospheric effects. This has the net result of removing diffuse features that are larger than 9 pixels (or 2.'3). Each image of the HotSpot region is then resized to the same pixel size, resulting in two 80x80 pixel images. Their coordinates are rectified so that each image has the same coordinate mesh. Then the images are averaged to get the final image of the region.

The final step in the image processing is to knit the usable region of the original map to the new data. During the process, the flux densities of the original map are made consistent (bootstrapped) with the new HotSpot region map. The original map is cropped at about b=0.5, because all data above this is unusable due to poor weather. This map is then filtered with Rudnick's filtering algorithm with a 9 pixel window radius. This effectively removes all large scale background emission. The HotSpot map is similarly filtered. The original map is then re-sized to match the pixel size of the HotSpot map, and its coordinates are rectified by the small, less than pixel size difference in coordinates so the pixels overlap properly. This does not result in a pointing error of more than half the new pixel size. The next step is to match the fluxes and flux-character of the original map to the deeper HotSpot map.

To match the fluxes and flux-character of the new map, the original map needs to be scaled, but in such a way as it does not amplify the noise in the original map. To match the 'character' of one map to the other, we equate the standard deviations of the overlap regions, and the mean flux density of the overlap regions. We apply this scaling to the overall map. To accomplish this let G be the original map, and R be the map to be matched to:

$$\begin{cases} H = (\frac{G}{mean(G)}) & \text{this factors G to a mean of 1} \\ J = H \times i + (1 - i) & \text{scales image by factor 'i', and returns mean to 1} \\ K = J \times mean(G) & \text{returns the scaled image back to original mean} \\ K = (G - mean(G)) \times i + mean(G) & \end{cases} \tag{2.3}$$

K retains the same mean as G, but its standard deviation can be varied. This can be 'tuned' to be whatever standard deviation desired. 'i' can be solved to so that the standard-deviation of K is the same as R. In the last term, replacing mean(G) with mean(R) also results in a matched mean, such that:

$$K2 = (G - mean(G)) * i + mean(R) \qquad \text{gives: mean(K2) = mean(R)} \tag{2.4}$$

The resultant map retains all of the observed features, but is now scaled so that its mean value is the same as the exemplar map R, and the standard deviation of each map is the same.

This algorithm is applied to the original GCL map, using the overlap region between the original map and the HotSpot region as the regions to match. The factor 'i' can be applied to the original map as a whole while only a subset region is used to determine the factor 'i'. I use a brute-force solving method that progressively tests numbers to isolate a value out to 10 decimal places for the factor 'i'. The reduction steps are demonstrated in Fig. 2.3.

2.2.3 Flux Calibration Revisited

The new GBT map, while clearly similar in structure to the Sofue map, differs significantly in important details. Therefore, an effort has been mounted to study the consistency between our GBT map and Sofue's map. The central radio source Sgr A* has a flat spectrum across many wavebands (Melia & Falcke, 2001). So the goal was to use this as a bootstrap calibration between our GBT map and Sofue's map. The most important consideration was the removal of the background in both Sofue's and our map. There are three reasons for this. First, confusion is high in this region anyway because of the crowded field, so diffuse and nearby sources would make calibration difficult. Second, Sofue had already applied a layer of background subtraction with his BGF technique [a modified unsharp masking]. Third, the mostly likely cause of being unable to calibrate our GBT map properly likely comes from the atmosphere, giving the map excessive

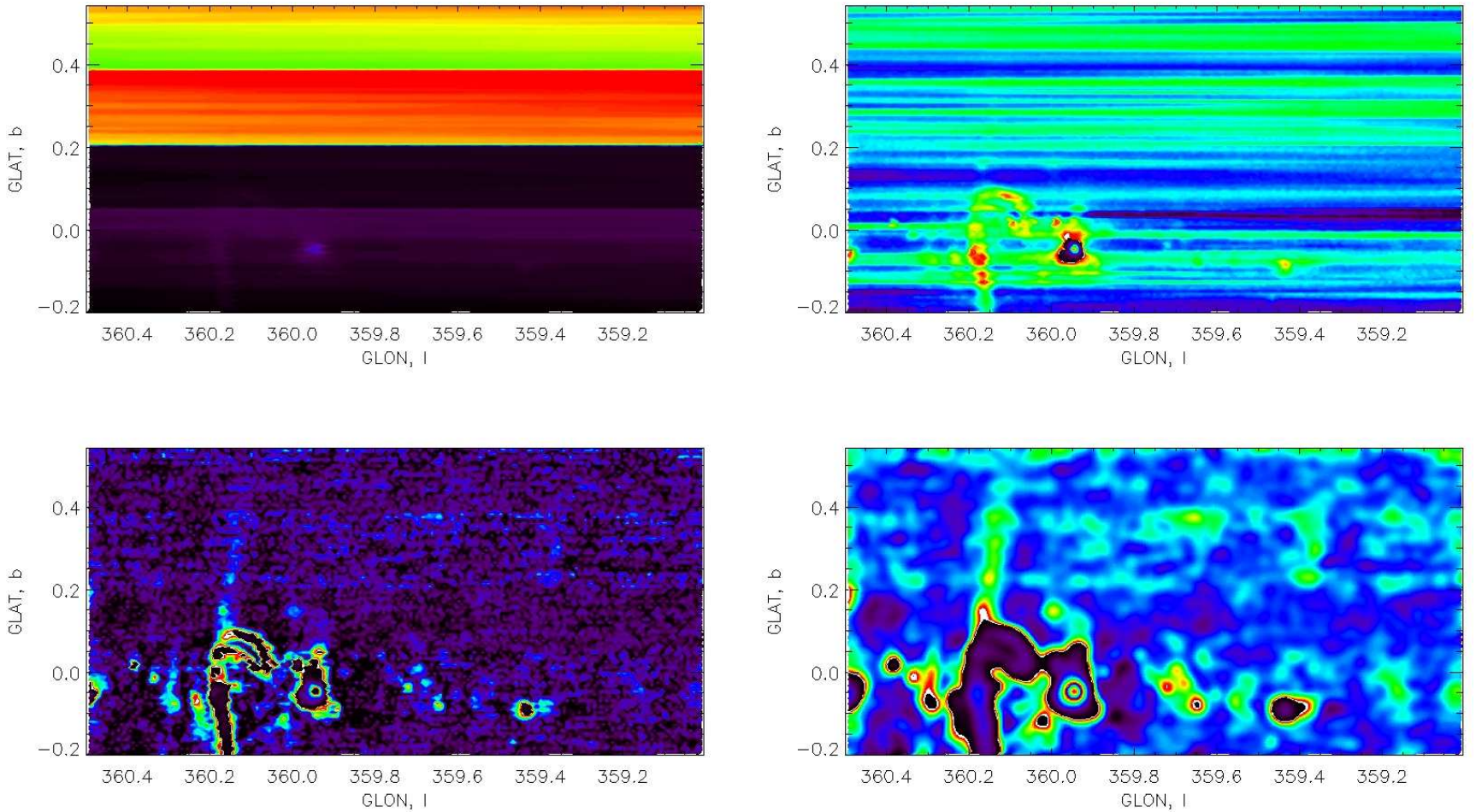

Figure 2.3: The several stages of the reduction of the first batch of data (without the 'HotSpot' observation) are presented. (top left) The Raw GBT 14GHz image, (top right) The noise calibrated, atmosphere and elevation corrected image, (bottom left) The RFT applied to remove atmospheric scanning effects, (bottom right) Gaussian smoothed (to 2' beam) final image

background than can be calibrated out.

Prior to attempting this recalibration of our GBT map, Sofue's map was further filtered to make it consistent with the processing that already done to our GBT map. This was done by applying the RFT to Sofue's data in order separate the diffuse from small-scale structure. Small scale in this case was a window size of 11 pixels to a radius of only 13', or approximately 3.5 beam-widths. So structures that were no larger than a few beam sizes were retained, larger structures were filtered out. This is consistent with our GBT map, which, when removing scanning effects, retained only such features smaller than a similar beam size. So, each map is now a map of the smaller scale structures above the noise, and not large scale, diffuse structure.

The first step in the re-evaluation of the calibration was to rework the maps so that they were consistent in pixel size, resolution, and rectification. In the routine SHAPEUP1, the finished GBT and Sofue maps were called, trimming the Sofue map to just the region in our map. First, the Sofue map was interpolated to match the pixel size and number of our GBT map, in this case approximately 500x300 pixels. Then each map was convolved to a 3.'6 Gaussian beam. This is the same beam size as the Nobeyama maps. Next, to ensure correct rectification, each map was repositioned so that the peaks of Sgr A* (the 'loudest' point in each map) were coincident, down to the pixel. Now the maps had the same pointing, the same resolution, and the same pixel size.

Next the scaling factor was determined to match the flux densities of Sgr A* in both maps using the routine FACTORSOFGBT. Here the crucial step is background subtraction. A slice through Sgr A* that also corresponded to relatively low background on either side of the source set the background for the images. To determine the background, the RFT was used to remove very large-scale structure using a window that was about half the width of the slice-length (in pixels). This removes the background component. The maxima from the slices were selected in the Sofue map and our GBT map. The scaling factor was max(Sofueslice)/max(GBTslice). This was approximately a factor of 2.

Now, the use of this scaling factor is tricky. This scaling factor relates the above-background flux of small-scale sources from our GBT map to the Sofue map. This factor cannot be used to scale the whole GBT map to be made consistent with the whole Sofue map, so making spectral index maps is not feasible with this method. However, the scaling factor can be used to compare flux density slices with their backgrounds removed. And this is what the routine SLICE2 does. This routine prompts the user to draw a slice on a portion of our GBT map, creates the slices in each map, removes the background in the same manner as the slices through Sgr A*, and then

multiplies our GBT slice by the scaling factor. After that the slices are plotted, and a spectral index between 14GHz and 10.5GHz along the slice is calculated. I use the standard S $\sim v^{-\alpha}$ spectral index relation, so, in shorthand, a negative spectral index, alpha, is typically a thermal source, and a positive spectral index is a non-thermal source. In this way, we can get an idea of the spectral index at the center of sources of interest, such as the walls of the GCL, the GC arc, and other GC plane features.

Chapter 3

14GHz GBT map and filtered 10GHz map

3.1 Our GBT 14GHz Map

The final map obtained at 14GHz with the GBT was convolved with a 2' beam to smooth out the noisy features (see Fig. 3.1), and to enhance the structure seen. The Galactic Center is the strongest feature in the map, though there is no detailed structure observed in the Sgr A complex. Projecting Galactic East from the Sgr A complex is an extension barely connecting to the arched structure known as the 'arched' filaments of the Galactic Center Arc (GCA). The two main divisions of the 'arched' filaments are clearly observed, with the northern filament being considerably brighter than the southern filament. These filaments join the 'vertical' filaments of the GCA, brightening slightly. The 'vertical' filaments appear more uneven than the 'arched' filaments, brightening as they cross the galactic plane (at b=-0.05). This brightening coincides with the well-known 'sickle' thermal feature. There are several layers of additional, fainter, emission directly east from the 'vertical' filaments. They form 'ripples' decreasing in size and strength away from the GCA. There is also a projection directly above the Sgr A complex that bends eastward and terminates on a point-like hotspot (referred to later as the thermal 'channel' structure).

The Eastern spur of the GCL (GCL-E) extends northward in galactic coordinates in a continuous extension of the Galactic Center Arc. There is no break in emission as it extends to GCL-E. The arm shows irregular compacted hotspots along the length of the arm until about b=0.35, where it dims after a hotspot. At b=0.45, the arm splits at a dimmer hotspot into two extensions,

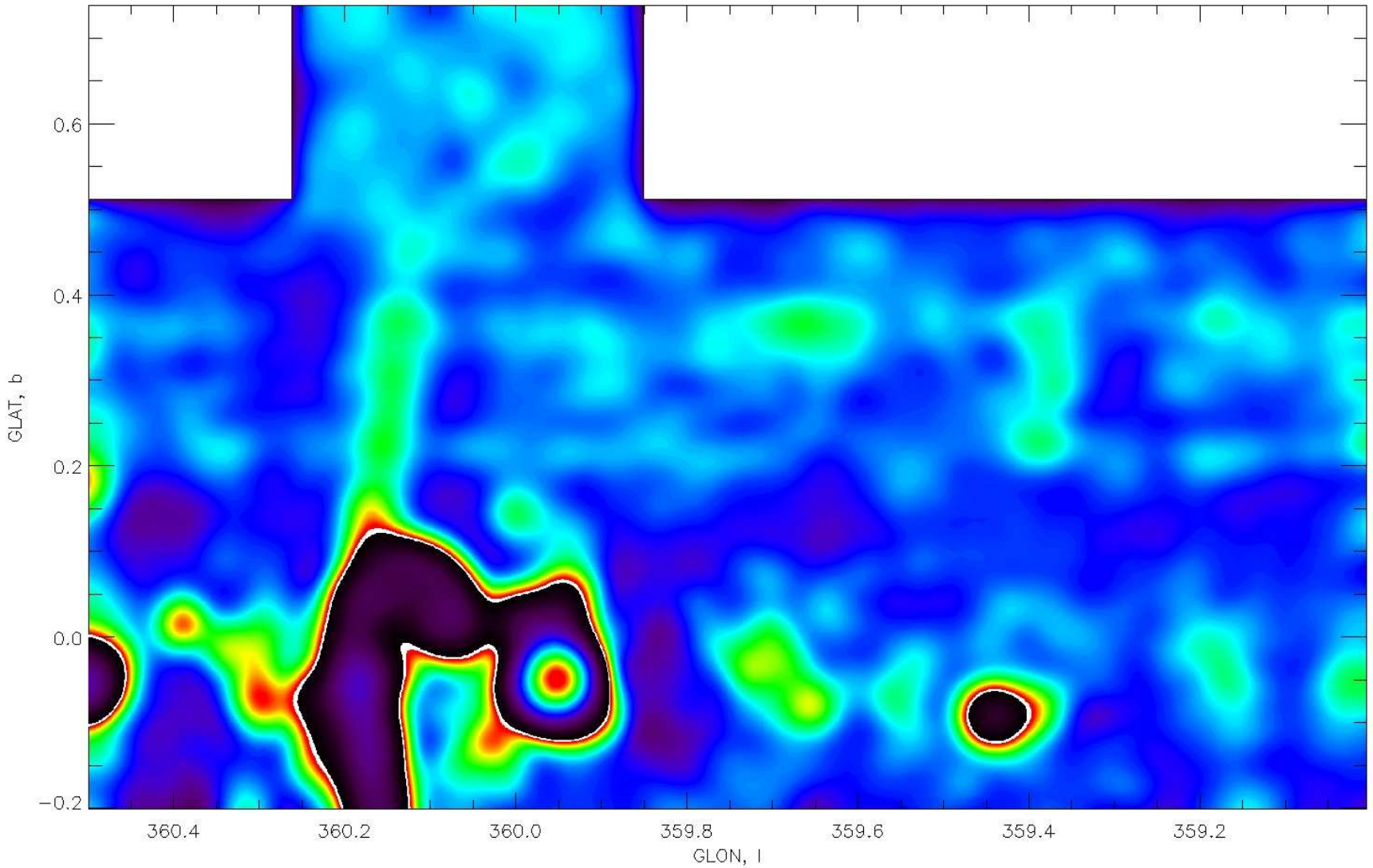

Figure 3.1: False color image of the final GBT map, including the 'HotSpot' region, convolved to 2' beam. Multiple transfer functions were used to display a variety of information over a large dynamic range.

to the East and West. At the vertex of this split is a bow-shock-shaped structure, which I have dubbed the 'paw' (since it looks like a paw print). There is a deep trough of close-to-background emission at (l,b)=(0.08, 0.56), the center of the 'paw'. The split in the arm curls around in a 'paw' pattern, around the emission trough. There are several compact emission regions around the circumference of the 'paw'. The Western side of the split continues north again at around b=0.6. The emission continues to the edge of the map.

The Sgr C complex contains little extended structure, but there is a slight projection, near the level of the background noise, that extends galactic north towards the Western spur of the GCL (GCL-W). GCL-W is not a continuous structure like the GCL-E, but begins suddenly at b=0.2. Nor does it extend continuously to the top of the GCL, it ends abruptly at b=0.4 - 0.45. The extent of the GCL-W is similarly splotchy in appearance with several distinct hotspots at (l,b)=(359.38, 0.23), (359.36, 0.28), and a more spread out hotspot at (359.40, 0.36). The northern boundary of the GCL-W in our data ends in an abrupt drop-off, angled NW. There is a diffuse 'finger' that extended to the NW on this drop-off, ending in another hotspot at (359.30, 0.45). The extent of our data on this side of the GCL ends at about b=0.5, above where the GCL-W emission ceases.

3.2 Noise Estimation

In order to estimate the noise in our image, we compare the intensity at each pixel with the maximum flux per unit area of the Sgr A complex. From this scaled map, 2 regions were chosen: (1) the region around the Sgr C complex and (2) a region with no obvious structure emission located between the spurs of the GCL. From these regions the background and rms noise was estimated. A 2D gaussian was fit to the Sgr C point source, and was subtracted from this $0.35^\circ \times 0.35^\circ$ region. The remaining mean background was 0.719% of the peak flux density of Sgr A, and the σ_{rms} noise was 0.189% of the Sgr A peak flux density. In the apparently source-free $0.26^\circ \times 0.20^\circ$ region, the mean background was 0.666% of the peak flux density of Sgr A, and the σ_{rms} noise was 0.147% of the Sgr A peak flux density. The average σ_{rms} is then taken as 0.168% of the peak flux density of Sgr A, and the mean background flux is taken as 0.693% of the peak Sgr A flux density.

The atmospheric scanning effects are manifest as low level intermittent horizontal stripes across the image. The brightest stripe interpreted as a scanning effect is located at about (l,b)=(359.6,0.4), has a mean brightness of 1.2% of the peak flux density of Sgr A and covers an area of about 34arcmin^2. Consequently, this 'stripe' shows an intensity $1.2\% - 0.693\% = 0.507\%$

above the background. This is a factor of 3 times greater than the random noise. This unremoved stripping induces a non-random uncertainty into our map which requires that any features in the vicinity of a stripe rise at least 6σ above the random noise in the map. For instance, much of the GCL-E structure lies at the cusp of this 6σ detection region, with only the hotspots located at b=0.15 and b=0.23 being well above the detection the 6σ limit (10σ and 7σ respectively). However, the atmospheric features setting this limit are *horizontal* features, and the GCL-E is a decidedly *vertical* feature, the GCL-E is well above the standard 3σ detection, thus the structure of the GCL-E is reliable.

Features in the 'HotSpot' region, however, because this mapping is a co-added image of cross coordinate observations (basket-weaving), are not infected with the stripping and, therefore, the usual 3σ criteria for detections is applicable. Specifically, in the 'HotSpot' region, the 'paw' feature is a faint structure, whose peak intensity is at a level of 3.26σ detection. Furthermore, corroboration of this structure morphology follows from multi-band correlation (see ch.5) and a detection limit of 3σ is used in this region.

3.3 Sofue's 10.5 GHz image and the Rudnick filter

I have obtained Sofue's original map (it is available for download on Dr. Handa's website: http://www.ioa.s.u-tokyo.ac.jp/ handa/pub/), and applied the RFT to better match the smaller scale features to our 14GHz GBT maps. The map covers about 2 degrees in Galactic Longitude, and 3 degrees in Galactic Latitude, centered on the Galactic Center. We apply a filter size of 9 pixels to the originally 111x151 pixel maps. The walls of the GCL are emphasized in the filtered map (see Fig. 3.2). The extended background is mostly removed, even better than with Sofue's Background Filtering Technique (BGF) developed in Sofue & Reich (1979). Even in the crowed field of the galactic plane, the diffuse background on the plane itself is substantially removed.

There are a number of substantive enhancements from the application of the RFT to Sofue's map. The GCL-E and the GCL-W are considerably enhanced; structures that were obscured by the diffuse background are sharpened. The ridge of the GCL-E appears more jet-like and shares the bloby structure observed in our GBT map; in particular they share a hotspot at about b=0.35. The GCL-E clearly deviates from its straight projection northward from the GCA. The deviation away from straight in the GCL-E occurs at precisely the location of the beginning of the 'paw' structure in the 14GHz map. Indeed, as the GCL-E proceeds west, then north, it follows the western rim of the 'paw', and confirms that this western extension continues north, until it mixes

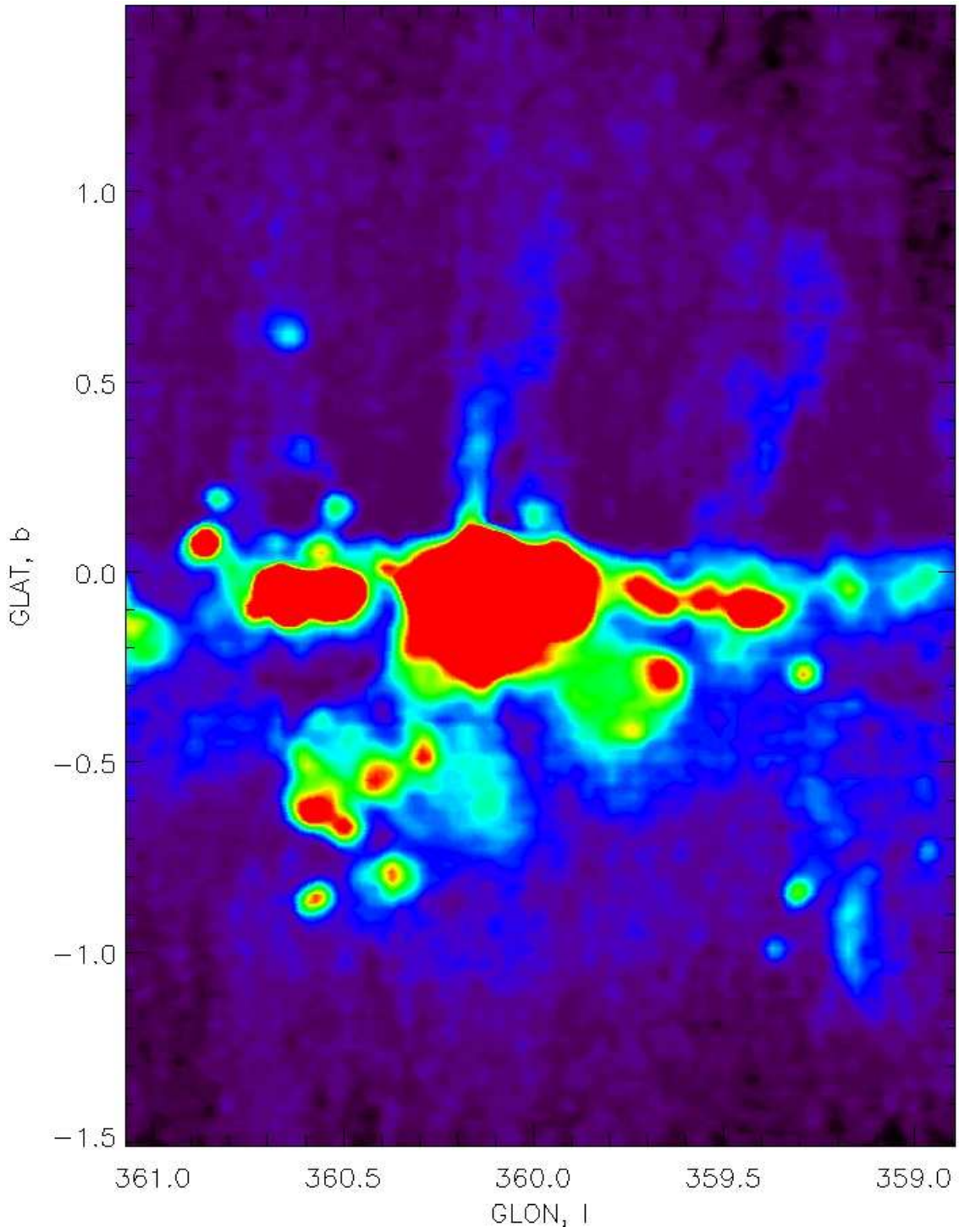

Figure 3.2: False color image of the RFT filtered 10.5GHz Sofue map. A filtering window of 9 pixels (radius [square]) = 10.'7 has been applied. High intensity contours have been suppressed to enhance the spurs of the GCL.

with the diffuse background at about b=1.0.

The GCL-W, in contrast to our 14GHz map, is a continuous extension stretching from almost the galactic plane to b=0.9. It does not, in this filtered map, connect explicitly with the galactic plane, however. There is a distinct disconnect between the GCL-W and the galactic plane. At the base of the GCL-W there is a small structure, at (l,b) = (359.55, 0.15), that seems to connect the GCL-W to the galactic plane, but this will be shown to be an unrelated structure, not a part of the GCL-W. In the unfiltered Sofue map, the GCL-W appears as a wide plateau of emission, but filtered, the plateau disappears, with a tongue of emission projecting east at b=0.5. The emission ridge is coincident with our 14GHz map, as is the angled edge of the 14GHz emission, but in the filtered Sofue map, the emission continues north instead of terminating at the hot spot observed in the 14GHz map. As the GCL-W continues north (in the filtered Sofue map), it widens and becomes more faint, ending with a slightly eastward curvature at b=0.9.

While the features of the GCL-E and GCL-W are enhanced by the RFT, we observe a previously unexamined feature above the SgrB-complex when the RFT is applied to Sofue's 10GHz map. Located at l=360.6, the SgrB-complex spur is a spur-like feature projecting northward, perpendicular to the galactic plane, similar to the GCL-E and GCL-W. This spur is fainter than the GCL-E or GCL-W. There is a large point source at (l,b)=(360.6,0.6). It is unclear whether this point source is a foreground or background object, or an object near the galactic center. This northern spur is located approximately the same distance (in projection) east of the galactic center as the GCL-W is located west of the galactic center.

Chapter 4

Summary of Multiband Observations

In analyzing the characteristics of the Galactic Center Lobe and related structures a multiband image comparison is required. Fortunately the astronomical community is well equipped to share archival data, usually from internet query and in a calibrated form. In this chapter several such images compiled from the archives are presented and described. We also discuss any further reduction that has been done in the process of this analysis. For each image, a description and background on the structures of interest to this thesis are given, namely: the GCL (and its East and West components), the Galactic Center Arc (GCA), the Nonthermal Radio Filaments (NRFs), the Double Helix Nebula (DHN) and other structures (see Fig. 4.1 for regions as displayed in the Sofue map). The NRFs are observed in several regions; the 'paw' feature is at the northern end of those maps focused on the GCL-E.

4.1 High Resolution Radio Images

4.1.1 VLA survey images

A wide-field 333MHz (90cm) VLA image of the Galactic Center (GC) was constructed by LaRosa *et al* (2000) to obtain the 'largest, highest dynamic range, high-resolution, long-wavelength VLA image.' The mosaic image was constructed from archival images from Pedlar *et al* (1989) and Anatharamaiah *et al* (1991) observed in spectral-line mode at 333MHz (90cm) with the B-, C-, and D-configurations of the VLA and a bandwidth of about 3MHz. The mosaic image stretches

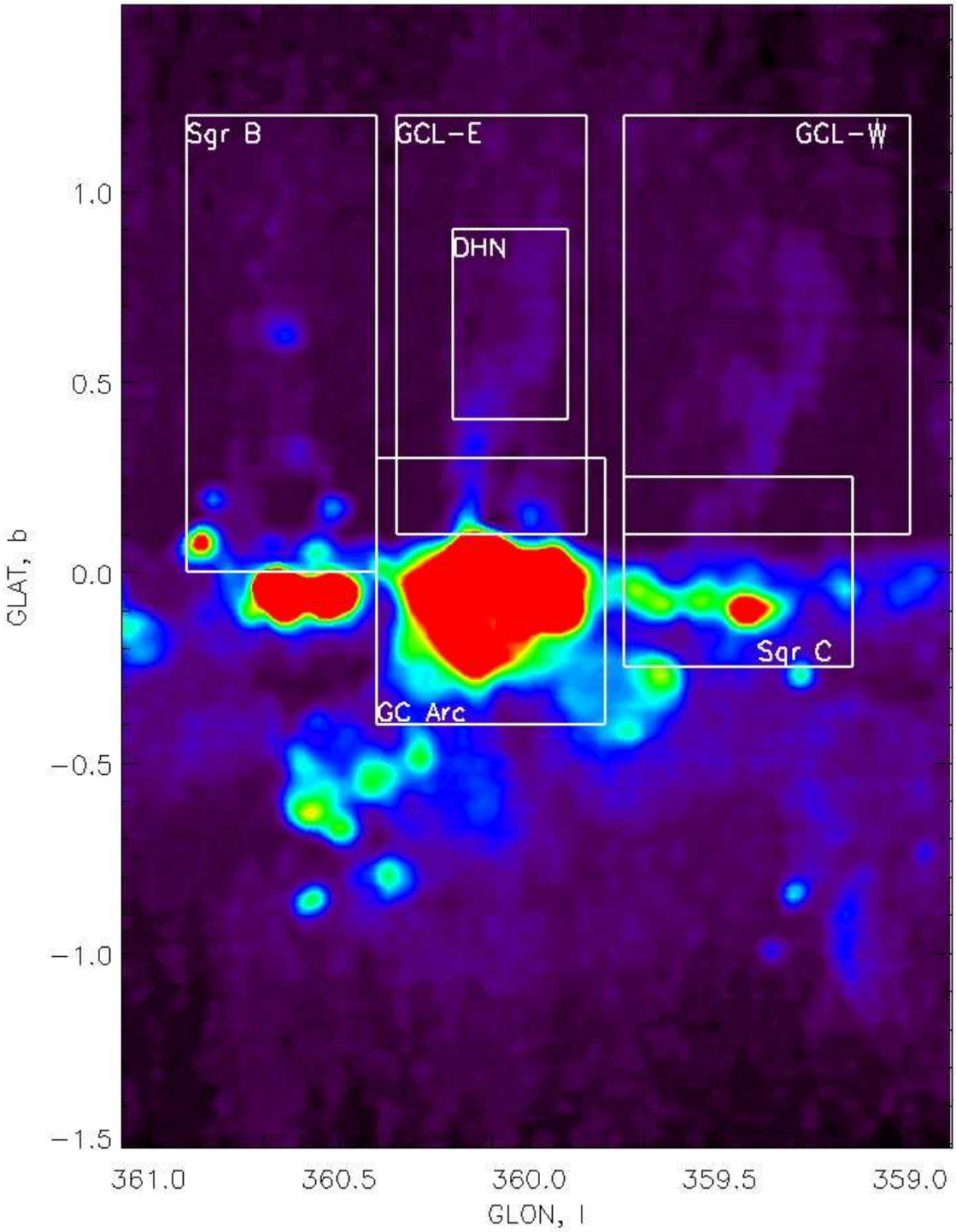

Figure 4.1: The RFT filtered Sofue map with the regions of interest inclosed in boxes, e.g. the GCL-E, the DHN, the GCL-W, Sgr C, the GCA, and the Sgr B-complex. The Galactic Center Region has been suppressed to emphasize the 'spurs' of the GCL.

about $4^\circ \times 5^\circ$ approximately centered on the GC, with a resolution of about 43" x 24", spans a maximum angular extent (due to interferometric nature of the observations) of about 45', and has an rms sensitivity of 5 $mJy \cdot beam^{-1}$. The file for this image (in fits format) was obtained from the website: *http://rsd-www.nrl.navy.mil/7213/lazio/GC/* cited in LaRosa *et al* (2000). The image (Fig. 4.2) was constructed using wide-field imaging techniques to correct for non-coplanar effects.

Yusef-Zadeh *et al* (2004a) have constructed a similar image from new and archived observations with the VLA at 1.4GHz (20cm). The image was 'feathered' from 40 overlapping VLA observations in the VLA's hybrid CnD configuration, and a single-dish observation based on Effelsburg data (Reich 1982) to compensate for the VLA's lack of sensitivity to large scale structures. "The feathering technique consists of making a weighted average of the images to be combined in the spatial frequency (Fourier transform) plane" (Yusef-Zadeh *et al* 2004a). The image covers a range of 'l' between -5 and +2 degrees, and 'b' between $\pm$ 40' around the GC, has a resolution of 30", and background continuum emission between 20 and 40 $mJy \cdot beam^{-1}$. The image (Fig. 4.3) was obtained directly from Dr. Yusef-Zadeh through a personal communication.

4.1.2 The GCL-E in high-resolution radio

Among a myriad of small-scale, filamentary features in the 90cm VLA image, the GCL-E is quite prominent. The image has been filtered with RFT using a 5 pixel (0.'54) radius window to emphasize diffuse structure. This window is approximately the size of the beam of the image, so only features that dominate in the large-scale will be in the 'open' image. The GCL-E is even more prominent in the 'open' image [note that the 'boxy' appearance in Fig. 4.4 is an artifact of the square shape of the filtering window]. The GCL-E appears to brighten at about b=0.35, and then split at b=0.45. As the GCL-E is traced farther north, after the split, it becomes more faint, but it can be seen to bend West and then straighten North again at b=0.6. This is represented more clearly in the 'open' image. The diagonal (NE to SW) strip is an artifact of the non-coplanar mosaicking of the original image performed by LaRosa *et al* (2000).

The 20cm VLA image is similar in many respects to the 90cm image, but the filamentation (see Fig. 4.5) is more prevalent, likely due to higher resolution. But, the diffuse structure of the GCL-E can be seen, and with similar application of the RFT (with a 13 pixel or 1.'1 radius filtering window), the GCL-E can be easily seen. The bend in the GCL-East (b=0.45) is very pronounced in the 'open' 20 cm image.

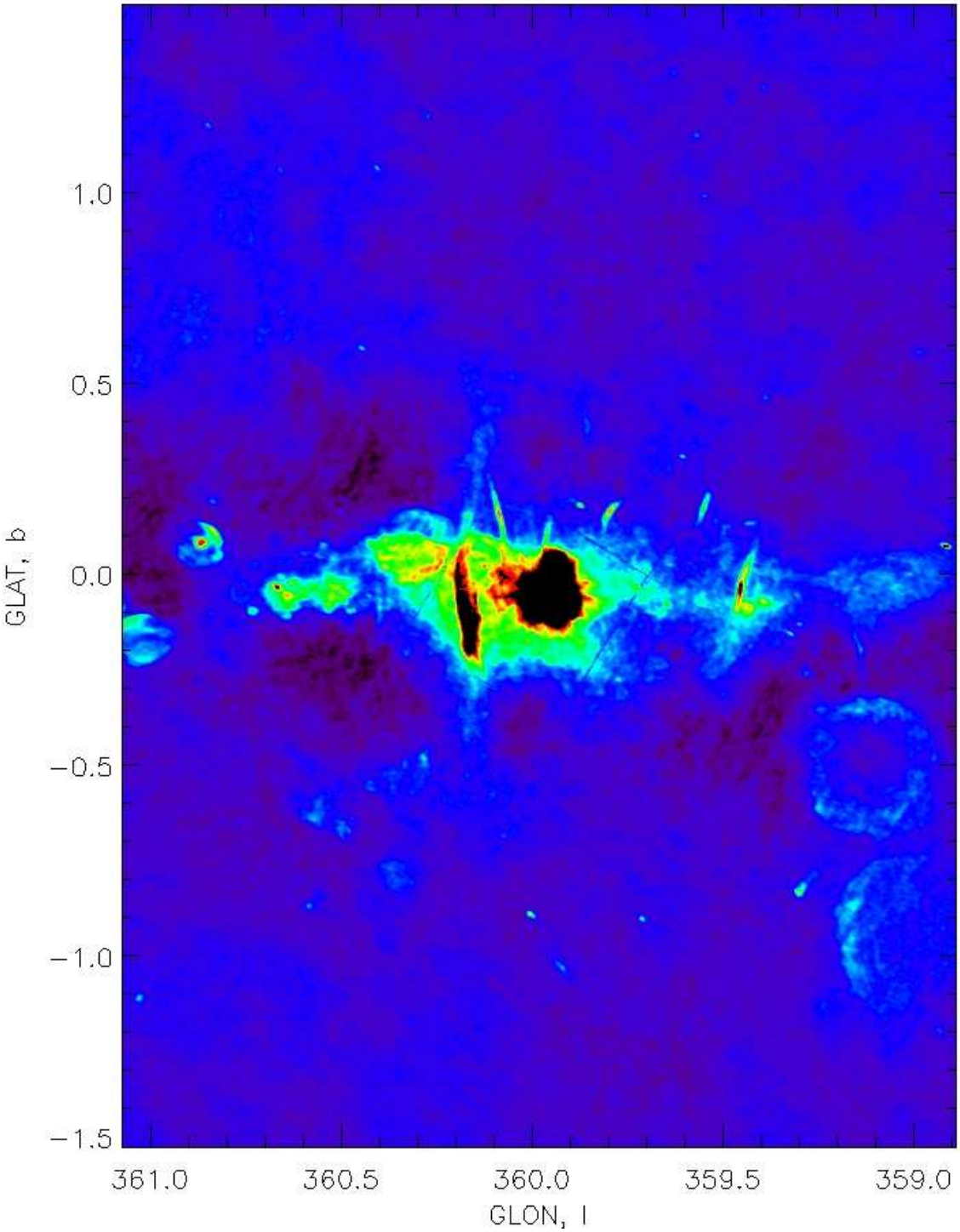

Figure 4.2: 90cm VLA map of GC region, the same region as the Sofue map is used. The GC has been suppressed to emphasize the diffuse structure.

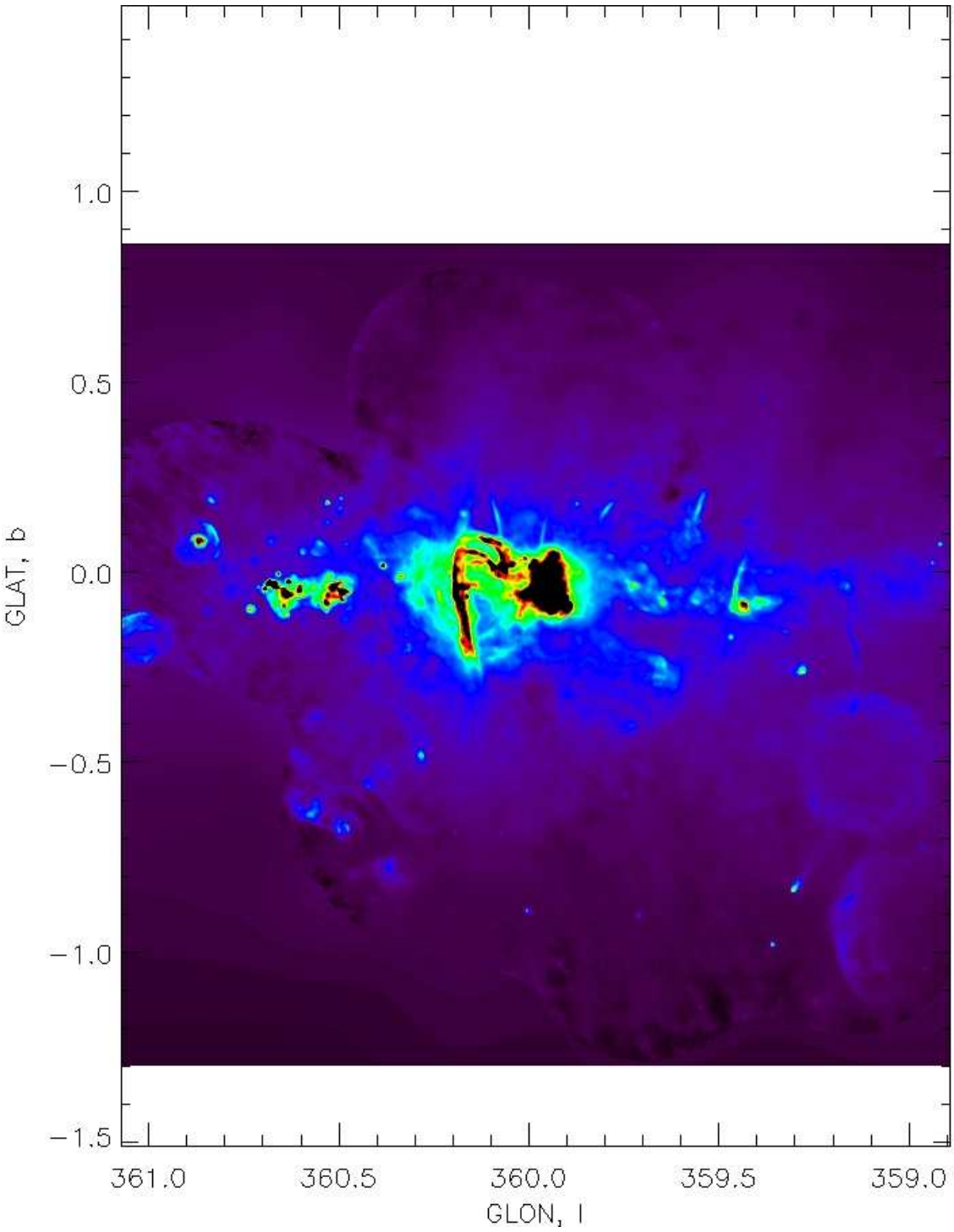

Figure 4.3: 20cm VLA map of GC region, note mosaic overlap with single dish data (e.g. upper left, etc.), the same region as the Sofue map is used. The GC has been suppressed to emphasize the diffuse structure.

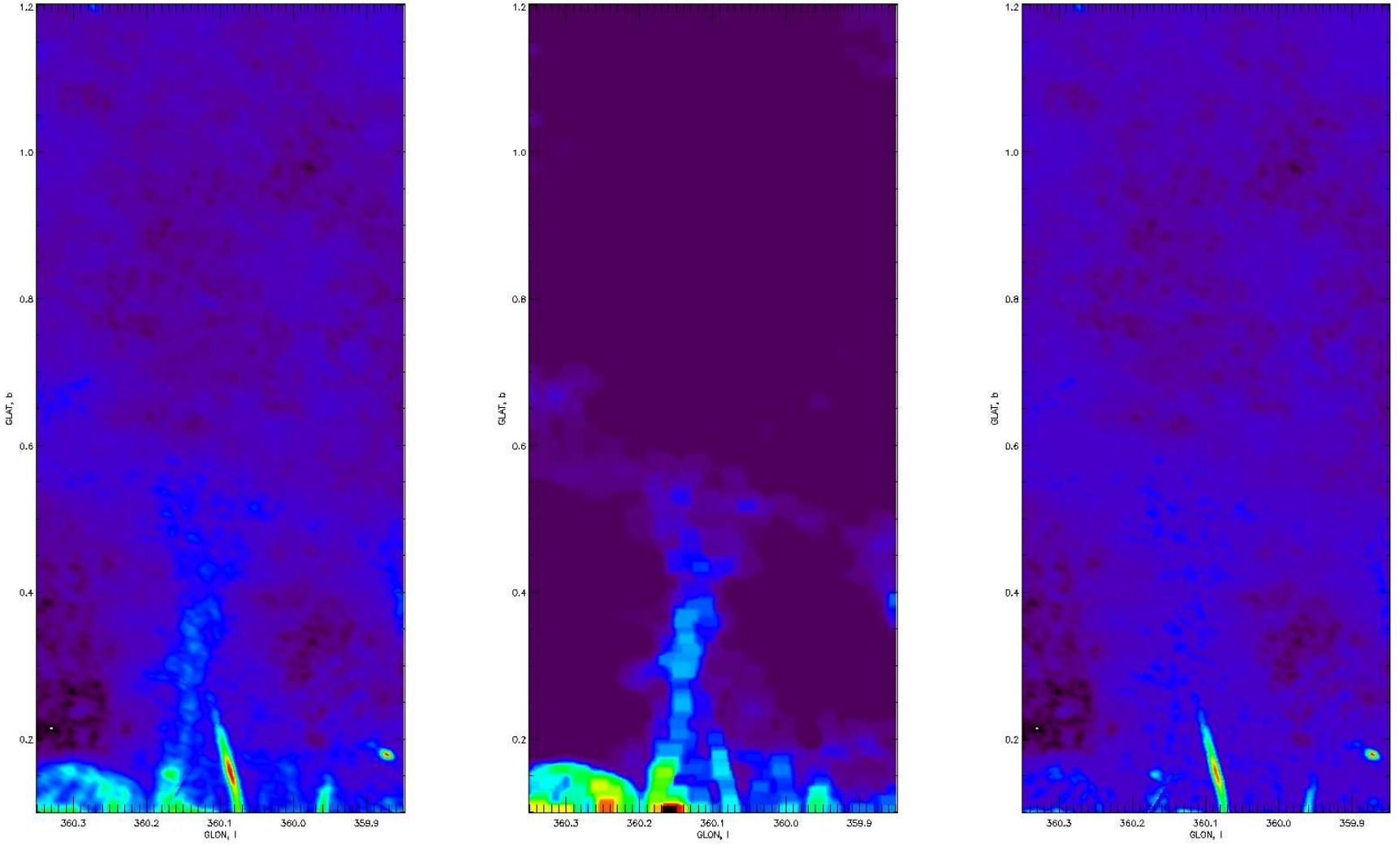

Figure 4.4: The 90cm VLA image of GCL-E region, filtered using the RFT (filtering window is 5 pixels = 0.'54.). (left) original image, (middle) 'open' image, (right) 'filtered' image. Note that the boxy artifacts in the 'open' image are due to the RFT.

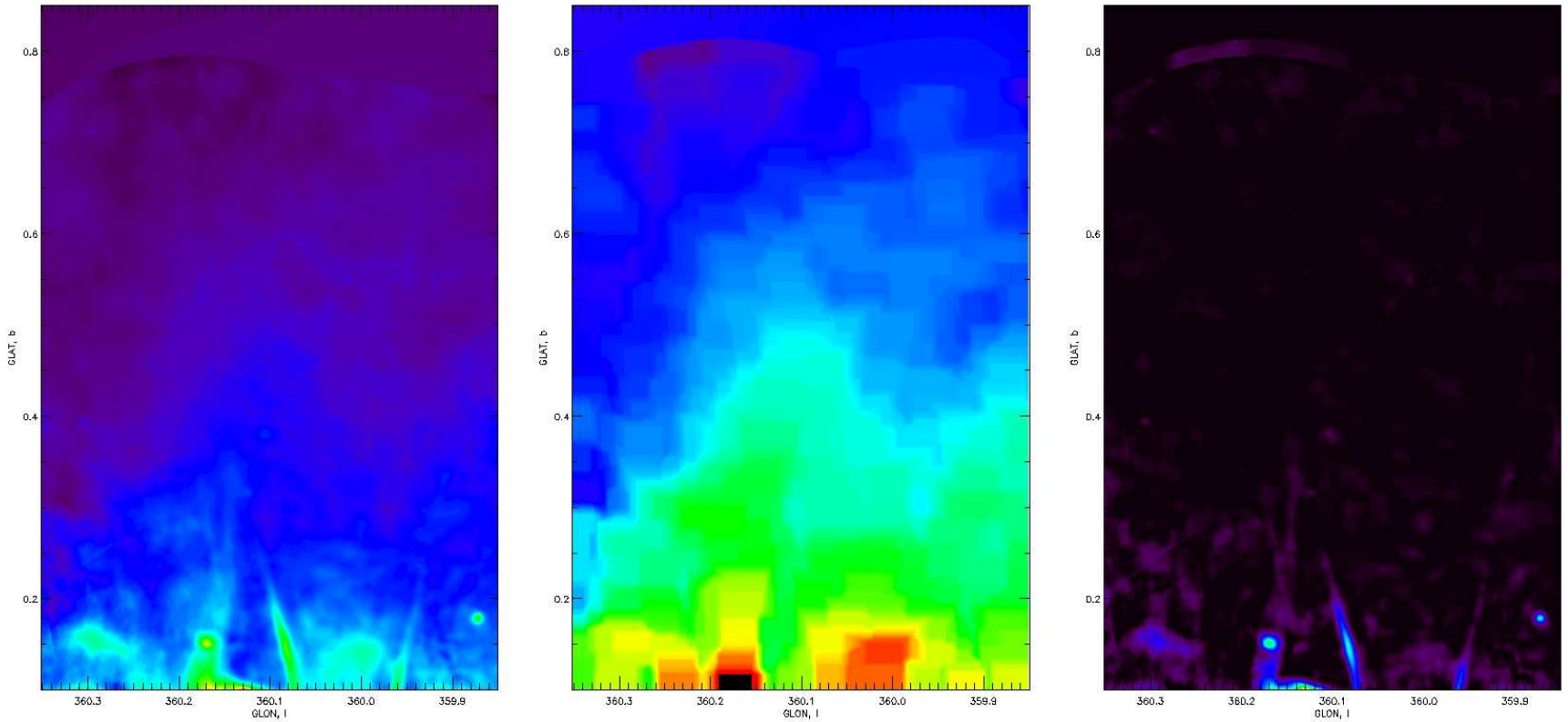

Figure 4.5: Same as Fig. 4.4 but the 20cm VLA data and a filtering window of 13 pixels = 1.'1 has been applied.

4.1.3 The GCL-W in high-resolution radio

The GCL-W spur is almost entirely invisible in the 90cm (333MHz) VLA map (see Fig. 4.6). Again, the map has been RFT filtered, with a window of 5 pixels (0.'54). Indeed, the only location with a trace of the GCL-W seems to appear is an enhancement (emphasized in the 'open' map) at b=0.55, otherwise it is quite unobserved.

Similarly, the 20cm map was RFT filtered (13 pixel or 1.'1 radius window) (Fig. 4.7). Although the GCL-W is also not very prominent in the 20cm VLA map, there is evidence of emission. Though there are some circular mask mosaicking artifacts, the GCL-W appears to widen in the 'open' map at b=0.3. Though the emission starts to approach the low-resolution single-dish edge at b=0.6, the emission mostly ceases at this point. The spur has a strong drop off of emission, on its western edge at about l=359.35.

4.1.4 The Galactic Center Arc

The Galactic Center Arc is a filamentary radio structure first observed in detail with the VLA by Yusef-Zadeh *et al* (1984). It is a "highly ordered set of large-scale features" related to the galactic center at galactic scales. It is characterized by two main structures, the 'vertical' filaments and the 'arched' filaments. The 'vertical' filaments are a bundle of narrow, long, straight, parallel filaments (up to 10' - 15' in length) perpendicular to the Galactic Plane located about 0.2° east of SgrA* (about 30 pc galactic east of the galactic center, in projection). The filaments can be as narrow as 1pc and between 10-100pc in length. The 'arched' filaments are a pair of curved filaments, emanating (or originating) from the galactic center (Sgr A complex), that terminate at their intersection with the 'vertical' filaments. These are quite different structures, though it is strongly thought that they are connected or at least related.

The 'vertical' filaments are non-thermal structures, though they are observed to have a mostly flat (between -0.2 and 0) spectral index. Yusef-Zadeh *et al* (1986) speculate that the 'vertical' filaments are embedded in a diffuse thermal gas that absorbs the 'vertical' filaments' non-thermal emission, flattening the spectrum. So despite its mostly flat spectral index, there are several characteristics that support its non-thermal character. There is 15-25% polarization (at 6cm) for part of the 'vertical' filaments which correspond to large-scale helical structure observed in the filaments. The polarization indicates that the B-field is mostly parallel to the filaments, and this suggests that a substantial fraction of the emission is synchrotron (non-thermal) emission (Yusef-Zadeh *et al* 1986). The 'arched' filaments, on the other hand, have a flat spectrum (again, between

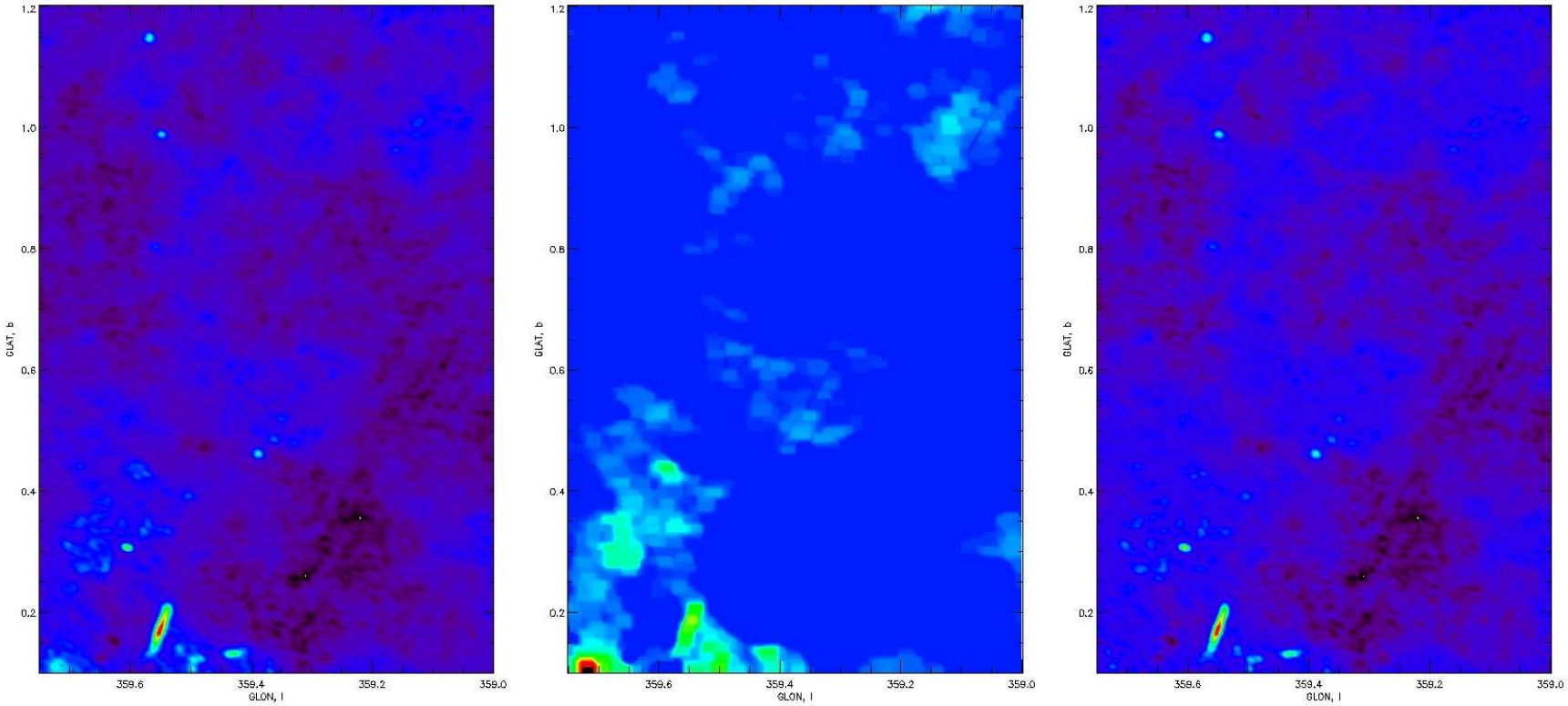

Figure 4.6: Same as Fig. 4.4 but 90cm VLA data of the GCL-W region. The same filtering window as been applied.

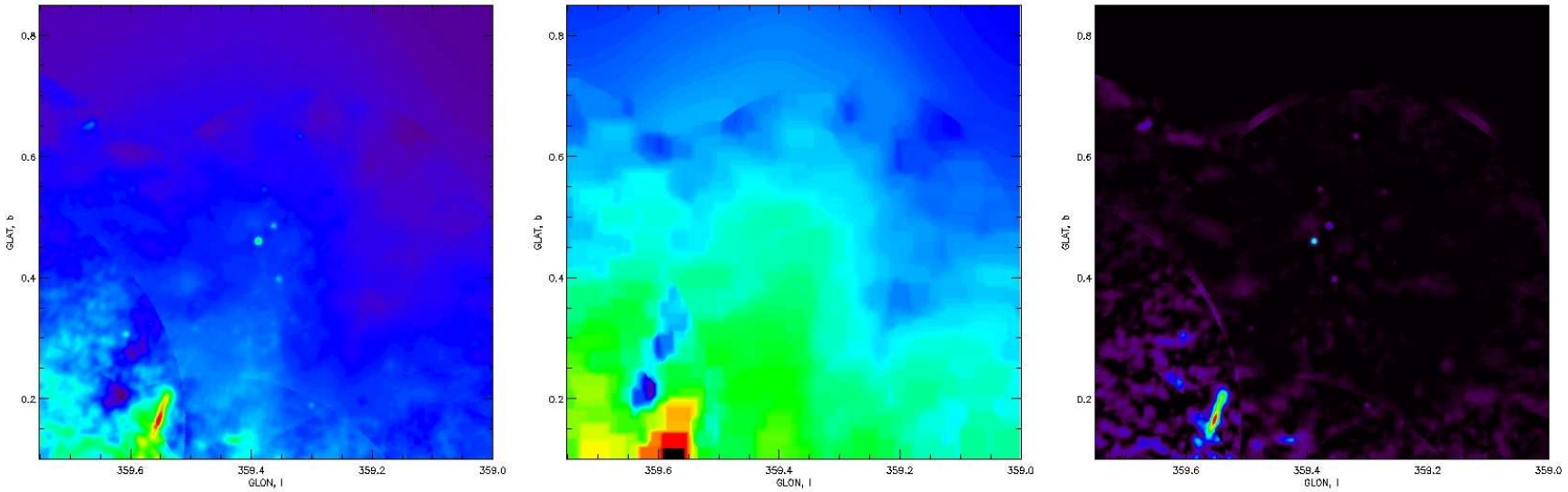

Figure 4.7: Same as Fig. 4.4 but 20cm VLA data of the GCL-W region. The same filtering window as been applied.

-0.2 and 0), no observed polarization, and have a coincident IR component. These factors speak to its thermal character.

The Galactic Center Arc is unlikely to be a foreground object, and there is evidence that it is interacting with the Galactic Center environment. The sickle shaped radio source (G0.18-0.04) is thought to be interacting with the 40 $km \cdot s^{-1}$ molecular cloud located at the galactic center (Yusef-Zadeh *et al*, 1984 and references therein). The 'vertical' filaments are seen to be affected by the 'sickle', in the 20cm VLA image (Fig. 4.8) and though the interaction is circumstantial, it seems clear that the Galactic Center Arc is indeed at the galactic center.

The 'vertical' filaments are generally of constant brightness, except where they cross the galactic plane, where they seem to be interacting with the 'sickle' and the 'pistol'. The 'arched' filaments are not as consistently of the same brightness, and they are generally dimmer than the perpendicular filaments. This is especially obvious in the 90cm VLA image (see Fig. 4.8).

We have applied the RFT to both VLA images of the GCA to enhance their filamentary structure (Fig. 4.9). One of the first impressions from the filtered images is the jet-like feature emanating from the Sgr A complex, most notable in the filtered 20cm image. Additionally, there are a series of faint, radial filaments centered on the 'sickle' structure; these have IR counterparts (see below). Since the RFT removes diffuse background, the 'arched' and 'vertical' filaments of the GCA are greatly enhanced, as is the connective emission above the GCA towards the GCL-E.

4.1.5 The Non-thermal Radio Filaments (NRFs)

The Galactic Center region in high-resolution radio observations is also characterized by the presence of long, narrow, filaments, generally oriented perpendicular to the galactic plane, and having a steep spectral index consistent with non-thermal emission, thus they are dubbed Non-thermal Radio Filaments (NRFs)(Yusef-Zadeh *et al*, 2004a).

The most prominent NRFs (see Fig. 4.9) that seem to have an interaction with the GCL structure are summarized. The two most prominent NRFs associated with the GCA are label N1 and N2 [the naming convention is from (Yusef-Zadeh *et al*, 2004a)]. N1 continues from or starts at the top of the 'vertical' filaments of the GCA, passing through (in projection) the HII cloud G0.17+0.15. The subfilaments of N1 run along the edge of and seems to be distorted by the shell-like HII region G0.17+0.15(Yusef-Zadeh *et al*, 2004a). N2, by contrast, starts at the western edge of the 'arched' filaments of the GCA and continues on to the GCL-E. Both N1 and N2 terminate at the compact source G0.12+0.32. It is not known whether they are interacting,

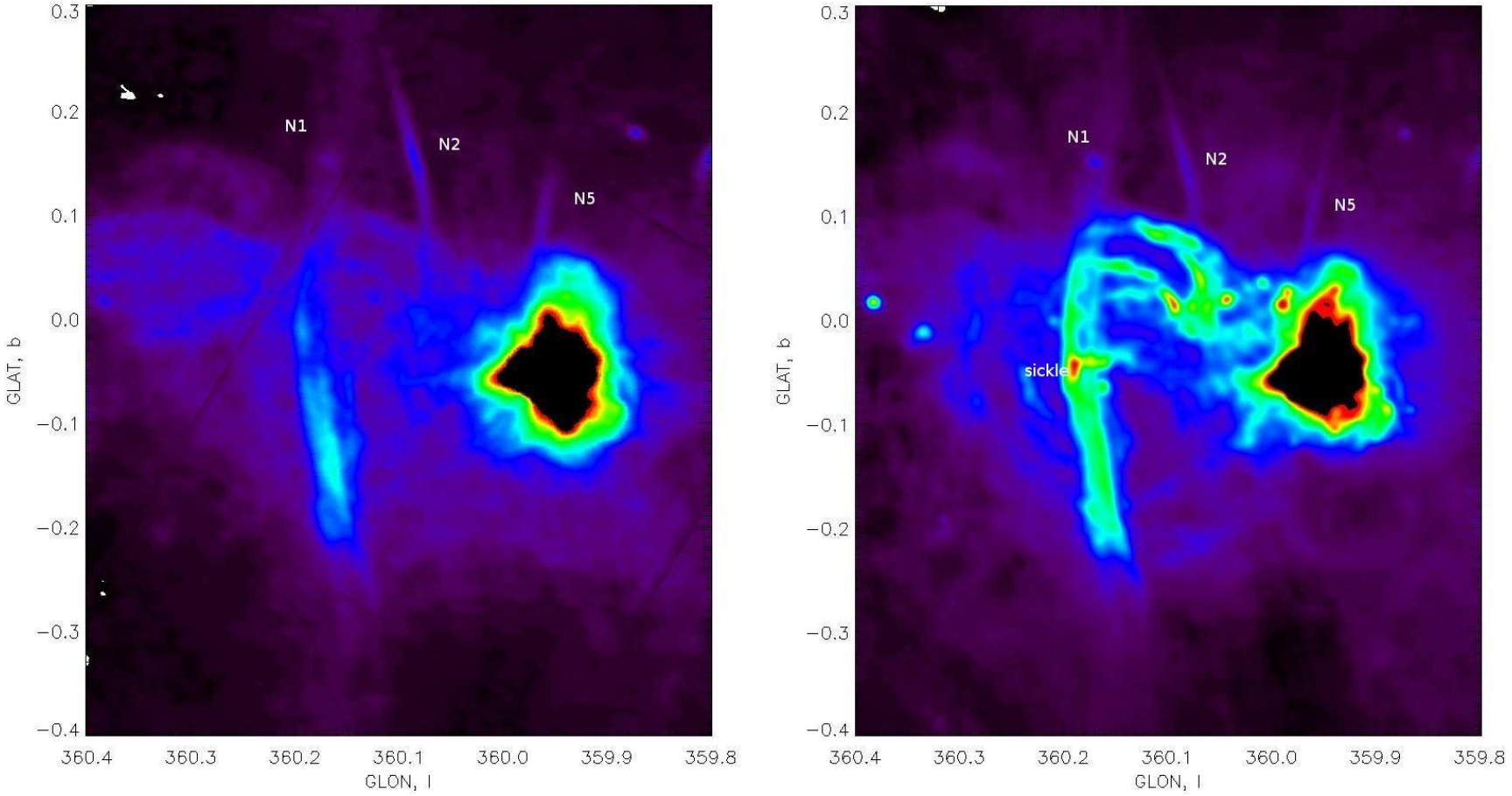

Figure 4.8: The GCA region as observed with the VLA. (left) the 90cm image, (right) the 20cm image. The GC has been suppressed so the 'vertical' and 'arched' filaments, in addition to other Non-thermal Radio Filaments can be seen.

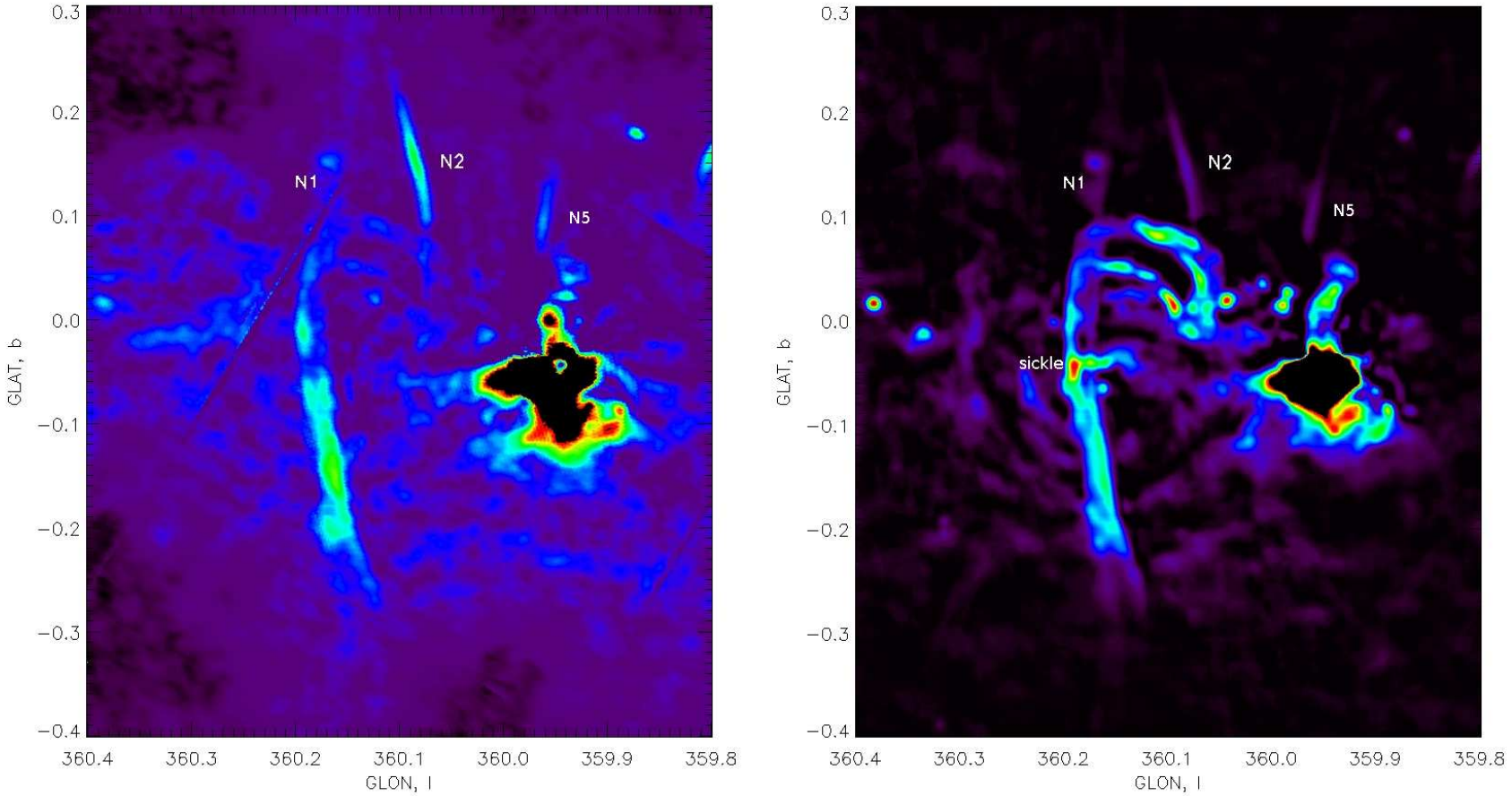

Figure 4.9: The GCA as observed with the VLA with RFT applied, (left) 90cm 'filtered' [N=10 pixels=1.'8], (right) 20cm 'filtered' [N=13 pixels = 1.'1]. The NRFs of interest, N1 and N2, have been labeled. Note also the fainter, radial, filaments in the 20cm image (right)

and whether they are also interacting with the non-thermal emission of the GCL-E as observed in the 20cm VLA map.

The prominent NRFs are brighter in the 90cm VLA map than the 20cm VLA map, thus indicating that they are likely non-thermal (as their name suggests), having steep spectra, they would be more luminous at lower frequencies (longer wavelengths). Conversely, those regions that are thought to be mostly thermal in origin, such as the 'arched' filaments of the GC arc, and not as luminous, again consistent with the thermal origin, having a inverted spectrum, thus being less luminous at lower frequencies (longer wavelengths).

4.1.6 Sgr C

In the 90cm and 20cm VLA images, the GCL-W meets with the Galactic Plane, not in a diffuse union, but at the end of a NRF. The NRF (C1 from Yusef-Zadeh *et al*, 2004a) emanates from the Sgr C region and is observed in both 20cm and 90cm VLA maps. Indeed, though the GCL-W is very faint in both the 90cm and 20cm map, the C1 filament diffuses up, into the faint emission. This region has also been filtered with the RFT (see Fig. 4.10) , but apart from removing the diffuse galactic plane emission, does not substantially enhance the NRFs or other structure. The C1 filament is thought to be non-thermal, and interacting with the Sgr C HII region (Yusef-Zadeh *et al* 2004a). Note that the compact source emission of Sgr C is almost invisible at 90cm, indicating thermal origin.

The other filament of interest is the C3 filament, to the north and a little east of the C1 filament. It is also non-thermal (Yusef-Zadeh *et al* 2004a) and leads into the GCL-W, as observed in the 20cm VLA map, where (on the side away from the galactic plane), it abruptly ends, whereas the galactic plane end of the NRF trails off into the plane. Thus this may mean there is a part of the GCL-W that is non-thermal.

4.2 High-resolution mid-IR images

4.2.1 Spitzer IRAC and MIPS survey images

Stolovy *et al* (2006) mapped the central 2×1.5 degrees of the Galaxy with the InfraRed Array Camera (IRAC) instrument aboard the Spitzer Space Telescope in all four channels (3.6, 4.5, 5.8 and 8.0 μm). The spatial resolution of the survey is approximately 2". The images were constructed from about 2895 pointings, and were acquired from the Spitzer archives in 7 'slices'

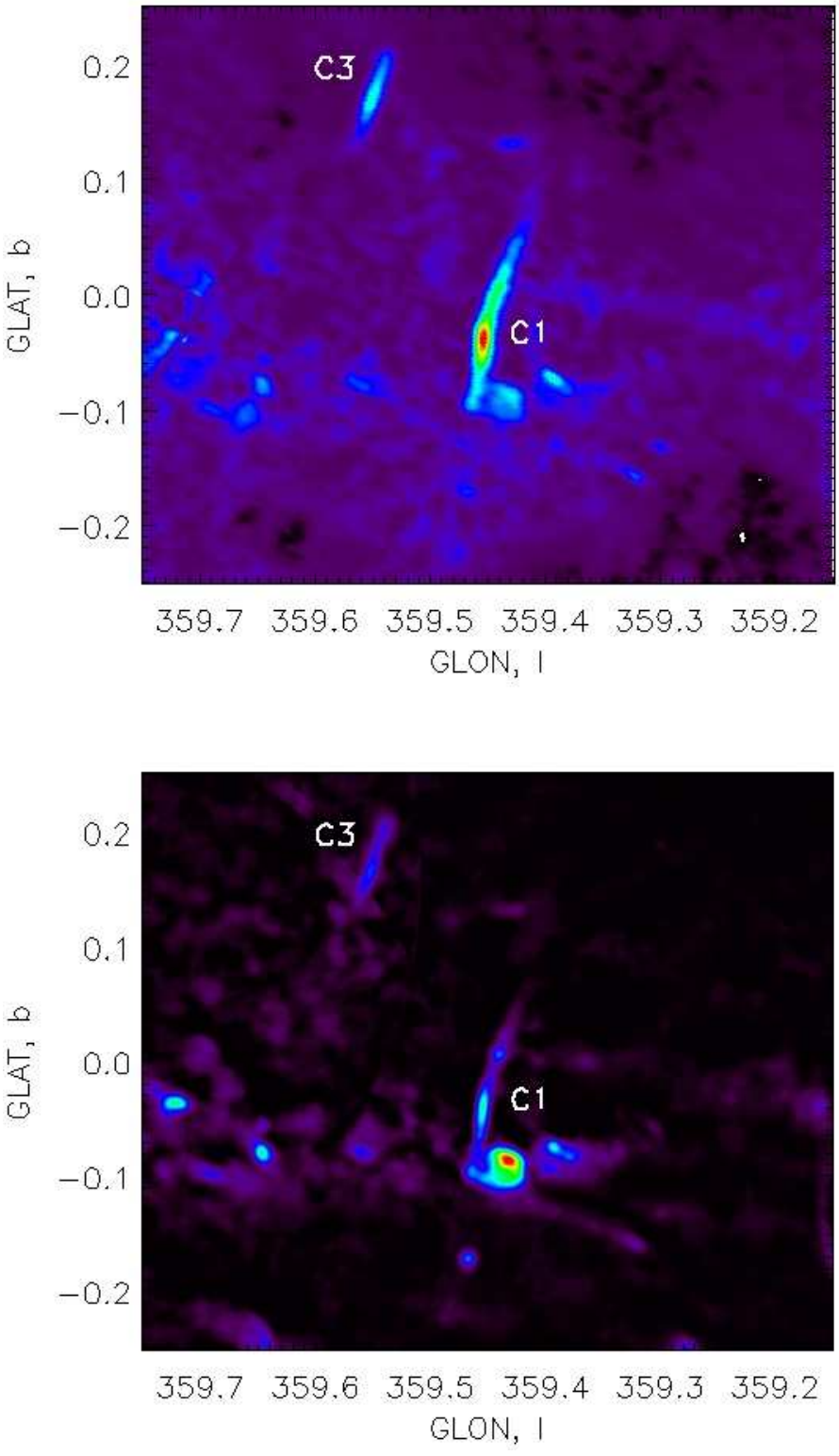

Figure 4.10: RFT filtered images of the Sgr C complex as observed with (top) 90 cm VLA [N=10 pixel = 1.'8] and (bottom) 20 cm VLA [N=13 pixels = 1.'1]. The NRFs of interest have been labeled, C1 and C3. Note in the 90cm image (top) the Sgr C HII cloud is barely visable.

of the region which were combined with our developed IDL software.

The ch1 and ch2 (3.6 and 4.5μm images respectively) are dominated by the galactic plane and point sources, and the filamentary structures we are interested in are not present. However, the overall structures of the GCL and the GCA are observed in the ch3 and ch4 (5.8 and 8.0 μm respectively) and are thus the focus of our analysis (see Figs. 4.11 and 4.12). To extract point sources (mostly) we use the RFT and obtain the 'open' (i.e. diffuse) image with a 3 pixel (3."6) radius window. This is on order the resolution (beamsize) of the images, and should emphasize diffuse, 'feathery', structure while reducing the imposition of point-like sources. The general diffuse structure in the IRAC images is dominated by emission from polycyclic aromatic hydrocarbons (PAHs) (Stolovy *et al* 2006). These are dust grains which are excited by the bath of UV photons at the Galactic Center and are indicative of star forming regions.

An image of the GC region was also obtained using the Multiband Imaging Photometer (MIPS) instrument on the Spitzer Space Telescope imaged at 24 μm by Morris *et al* (2006). The image (Fig. 4.13) has a spatial resolution of 6' and also images the inner few degrees of the Galactic Center Region.

4.2.2 The GCL-E region in high-resolution mid-IR

The GCL-E, as a northern extension of the Galactic Plane, is not clearly seen in either the 5.8μm or 8.0μm images (see Fig. 4.14). There is limited emission extending up from the top of the GCA. In the 8μm image, there is an arc of emission extending from the strong IR feature at (l,b) = (359.9,0.1) that loosely connects to the emission above the GCA. The emission from the GCL-E that does extend above the plane dissipates prior to ending about where the helical structure called the Double Helix Nebula begins.

The Double Helix Nebula (DHN) is a mid-infrared feature that exhibits an intertwined helical structure, seeming to coincide with the outer edge of the GCL-E, located about 90 pc from the Galactic Center (in projection), and oriented approximated perpendicular with the galactic plane. Images, from the Spitzer/IRAC observations, of the DHN and characterization of its morphology were published by Stolovy *et al* 2006. Both spurs of the GCL are observed in the Stolovy survey. While the Western spur of the GCL has similar 'feathery' morphology as the Eastern spur (and the DHN in particular), only in the DHN is helical structure observed in the IR.

The DHN is observed particularly well in the 24 μm image (see Fig. 4.15), and in Morris *et al* (2006) is described as being a double helix in shape, and whose origin was thought to be

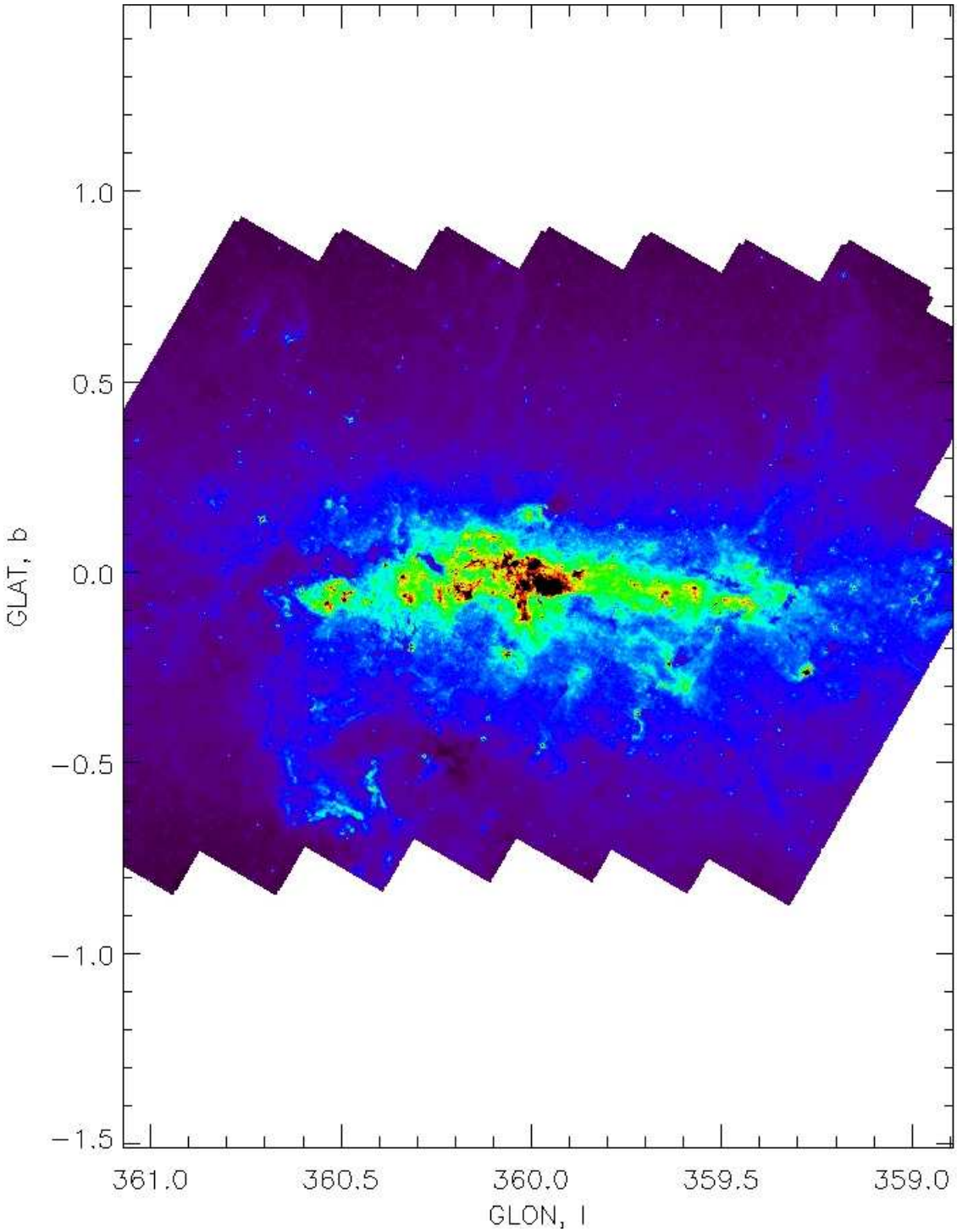

Figure 4.11: Spitzer IRAC ch3 ($5.8\mu m$) image of the galactic center. The image has been filtered with the RFT with a window 3 pixels ($\sim 3.6''$) to mostly remove point sources ('open' image).

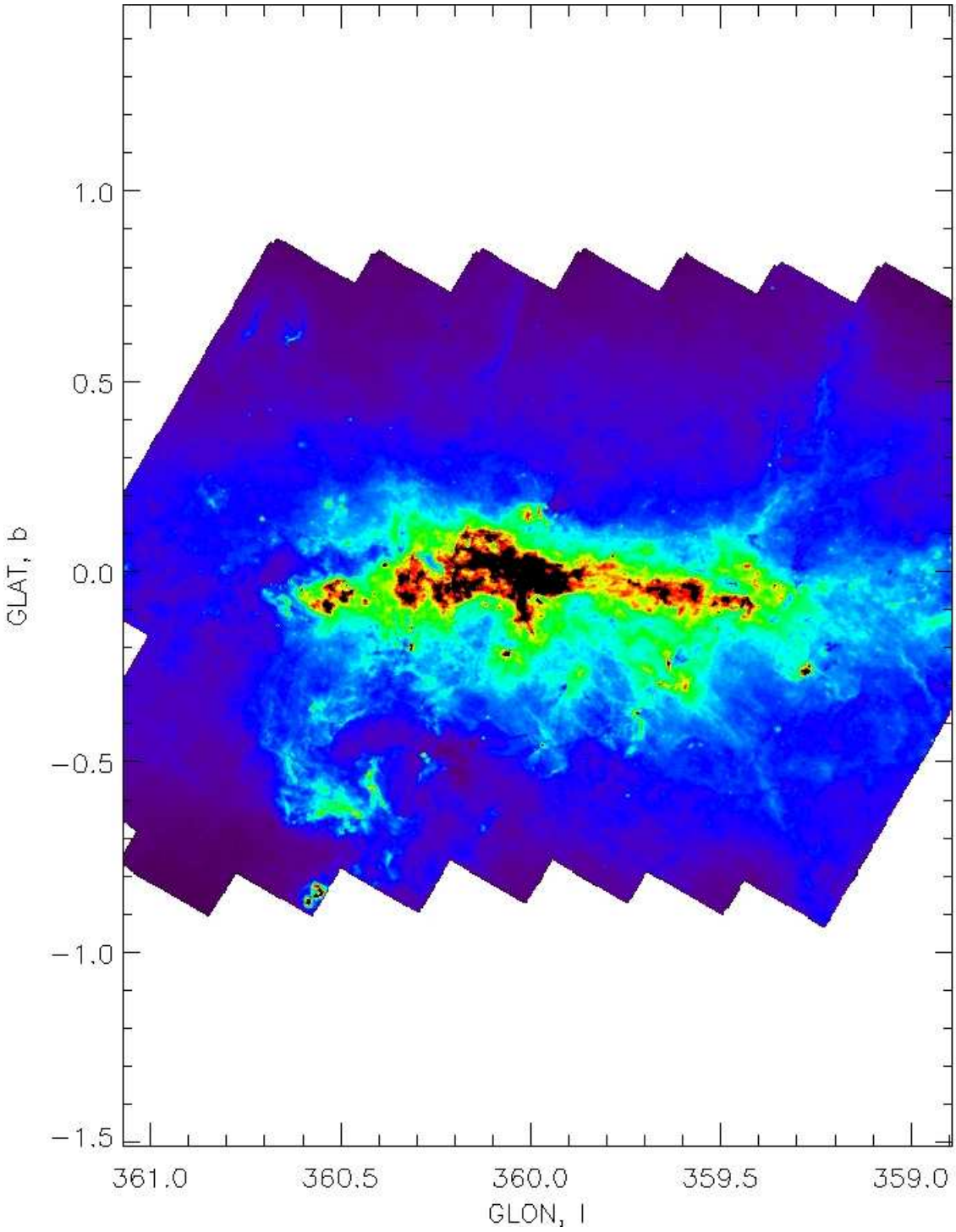

Figure 4.12: Same as Fig. 4.11 but the Spitzer IRAC ch4 (8.0μm) image.

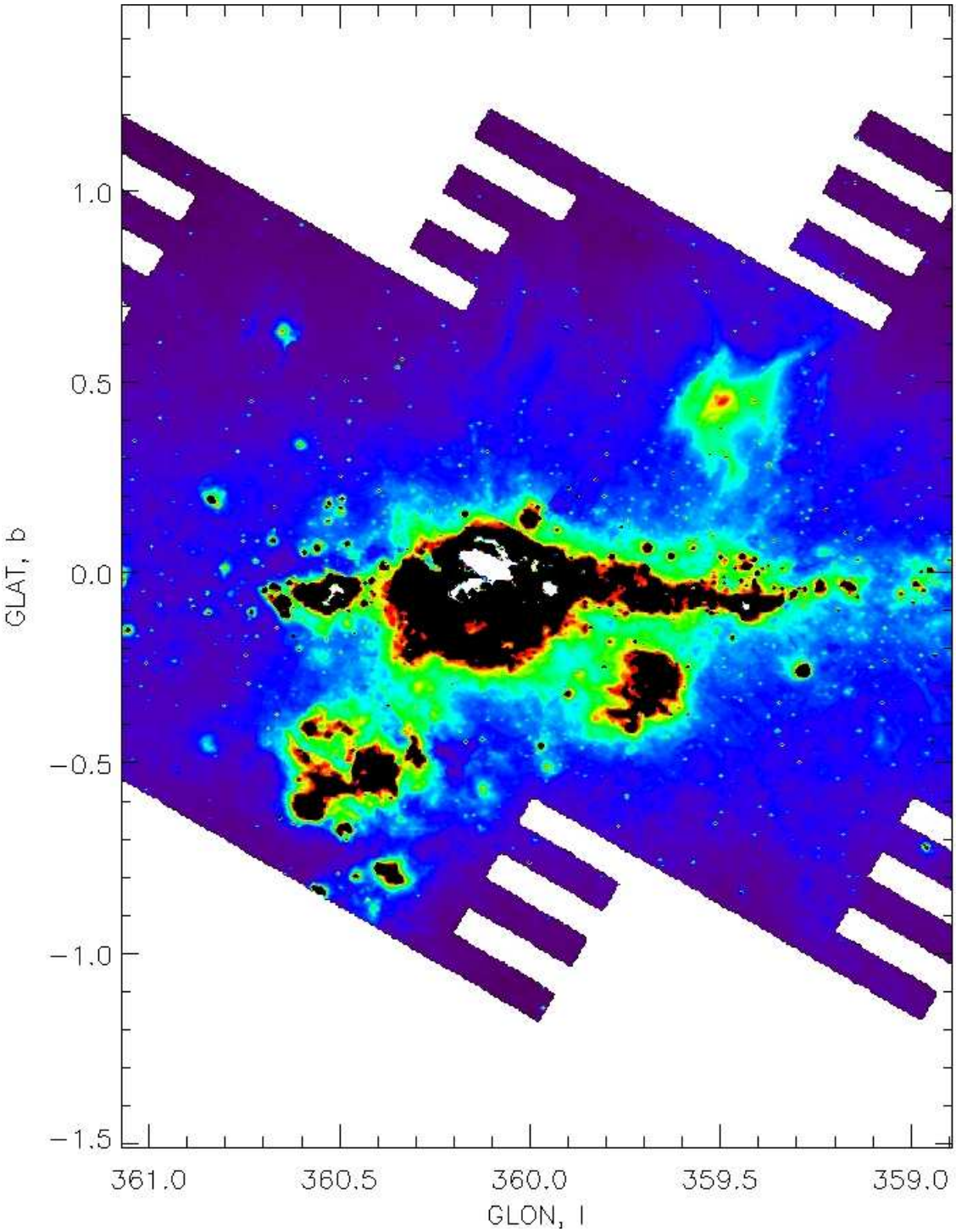

Figure 4.13: Spitzer MIPS ($24\mu m$) image of the galactic center region. Note that the central region was omitted from the survey due to risk of overexposure (in white) and the stronger emission has been suppressed in this image to emphasize the diffuse structure. Unlike the ch3 and ch4 IRAC images, this image has not been filtered to remove point sources.

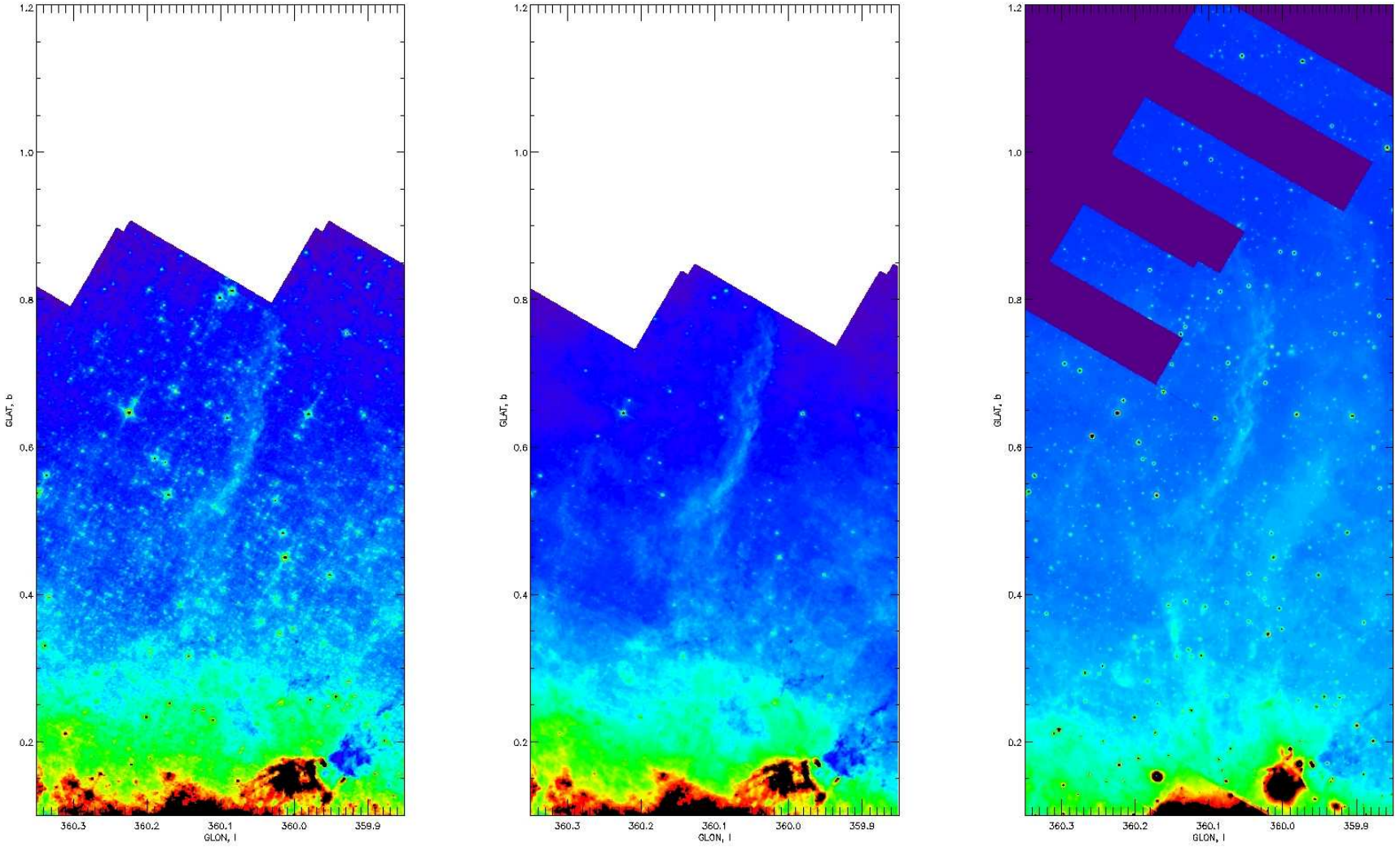

Figure 4.14: The three Spitzer images of the GCL-E complex. (left) Spitzer/IRAC ch3 5.8μm 'open' image. (center) Spitzer/IRAC ch4 8.0μm 'open' image. (right) Spitzer/MIPS 24μm 'open' image. Each image was filtered with the RFT to remove point-like sources with a filter window radius of 3 pixels = 3."6. except the 24μm image which had a radius of 1 pixel = 2."4.

a "magnetohydrodynamic torsional Alfven wave propagating more or less vertically out of the galactic plane, along magnetic field lines, from the near vicinity of the Galactic Center." From the galactic center, there is a strong magnetic field that is being ejected out from the center, and the emission mechanism of the DHN is interpreted as thermal dust emission. They suggest the thermal dust, charged (perhaps merely from inter-dust collisions), follows the magnetic field that is being ejected. Morris *et al* (2006) rule out thermal bremsstrahlung by hot electrons and non-thermal synchrotron emission from relativistic electrons both on spectral grounds. There are two strands, however, to the DHN. This kind of symmetry would originate from a bar or two displaced blobs (essentially a bar-bell).

4.2.3 The GCL-W region in high-resolution mid-IR

In all of the IR images, the GCL-W and surrounding structure is much more intense than the GCL-E region. In the 5.8 and 8.0 μm images (see Fig. 4.16), the GCL-W is clearly seen projecting galactic north from the galactic plane, becoming increasingly filamentary. At b=0.25 there is a filament that breaks away and continues west from the GCL-W. The main structure of the GCL-W is broken into two main filaments beginning at b=0.25 and b=0.4. All filamentation appears to be streaming north and west.

The 24 μm GCL-W region is dominated by the non-thermal molecular cloud AFGL 5376 (see Fig. 4.16). This is a structure that has a circular central hotspot, but becomes more diffuse at the periphery, and several streamers emanate from its central structure. It is also interesting that no trace of the IR source AFGL 5376 is seen in the 8μm Spitzer images, although the southern extended streamer may join up with a diffuse 'tongue' of emission from the GCL-W itself at about (l,b)=(359.46,0.29). The western perimeter of AFGL 5376 boarders the edge of the IR tendrils of GCL-W.

In the Sgr C region (Fig. 4.17), there is no obvious, coherent structure forming the joint between the filamentary GCL-W structures and the Galactic Plane. Since the images have been filtered to remove point sources, the diffuse emission from the Galactic Plane dominates. However, there is a dark cloud running perpendicular to the Galactic Plane to the west of the GCL-W (about l=359.3), though this is likely foreground extinction. There is also a foreground extinction cloud at the base of the GCL-W at about (l,b)=(359.4,0.1).

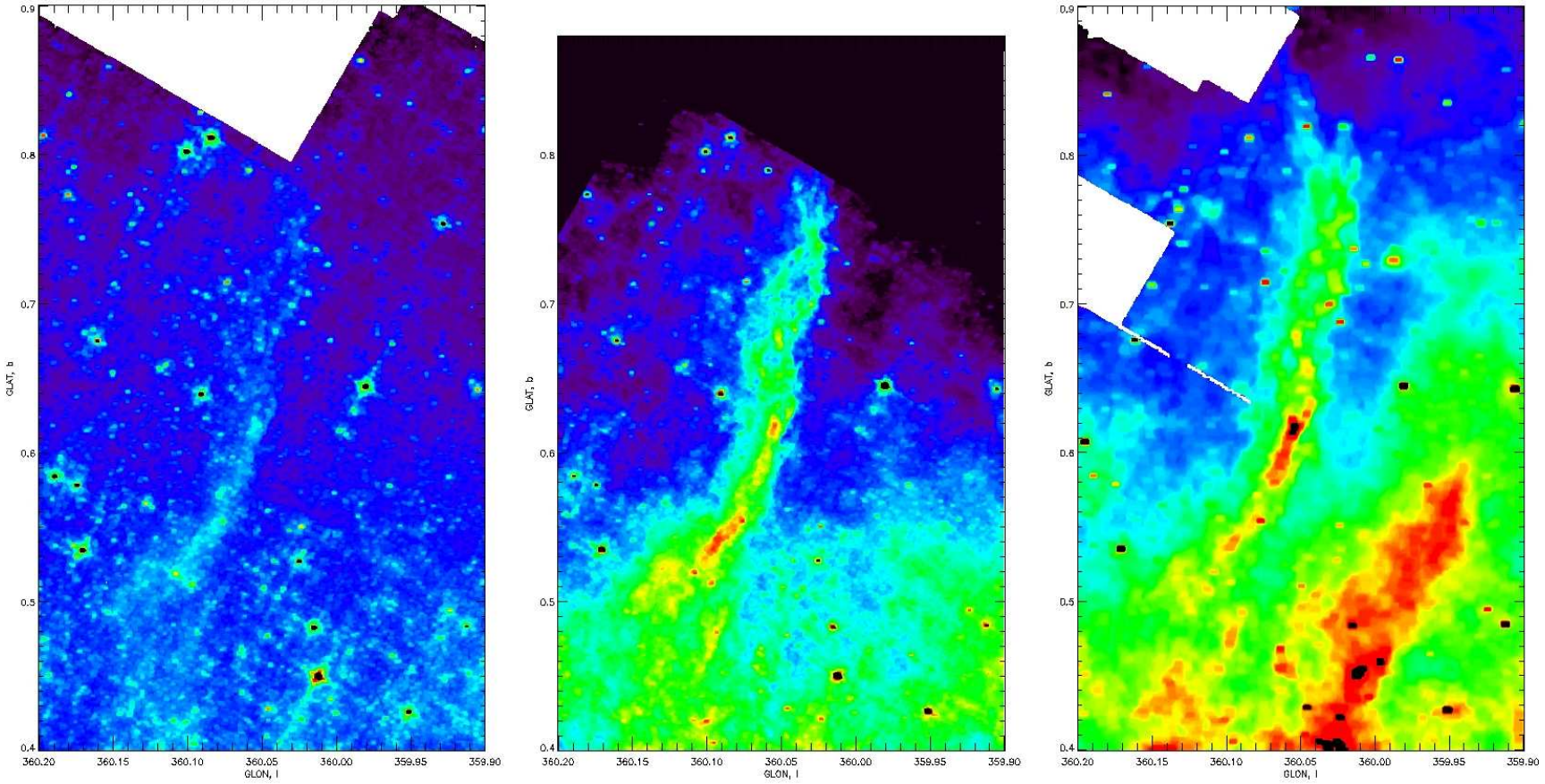

Figure 4.15: Same as Fig. 4.14 but of the Double Helix Nebula (DHN). Note also the prominent IR region west of the DHN in the 24μm map (right).

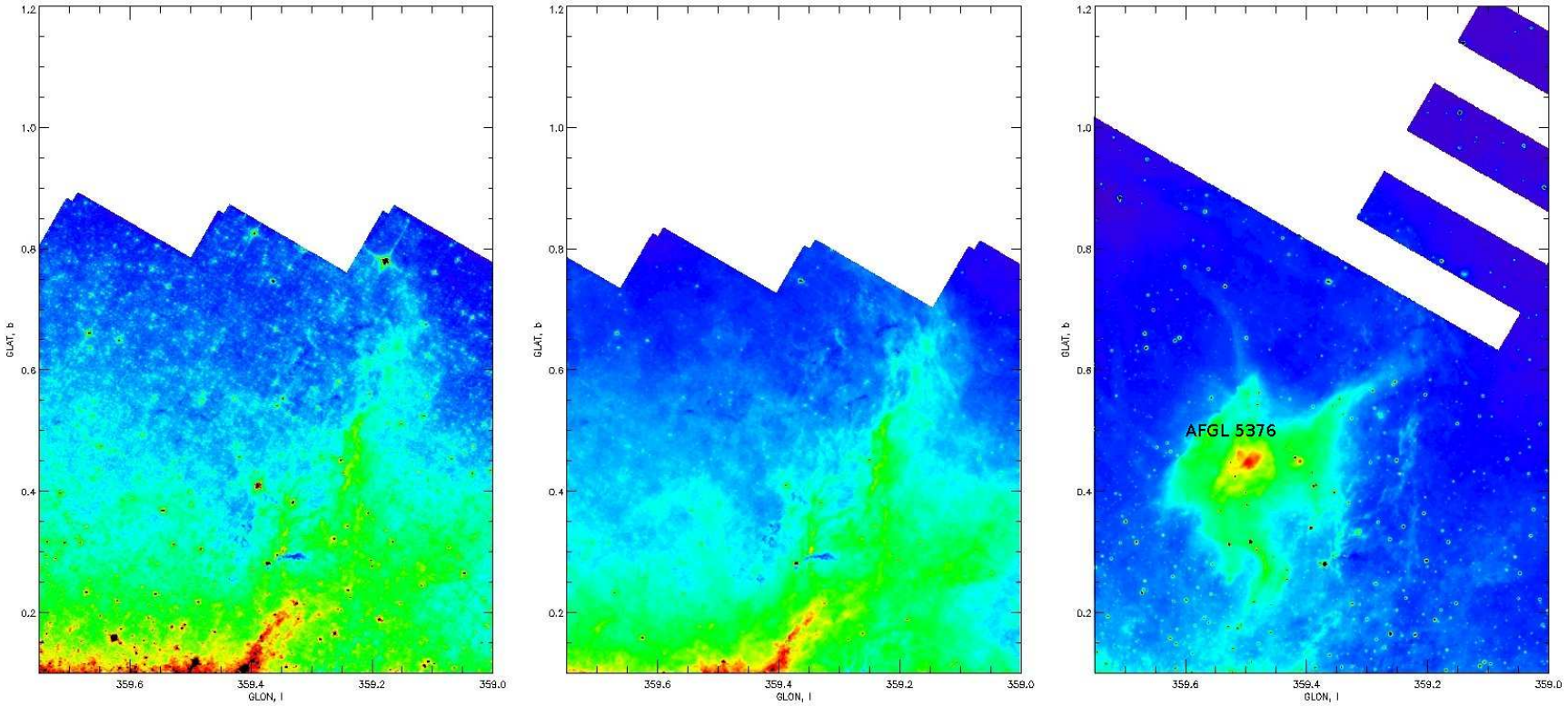

Figure 4.16: Same as Fig. 4.14 but of the GCL-W region. Note the lack of corresponding emission from AFGL5375 [which dominates the 24μm map (right)] in the 5.8μm (left) and 8.0μm(center) images.

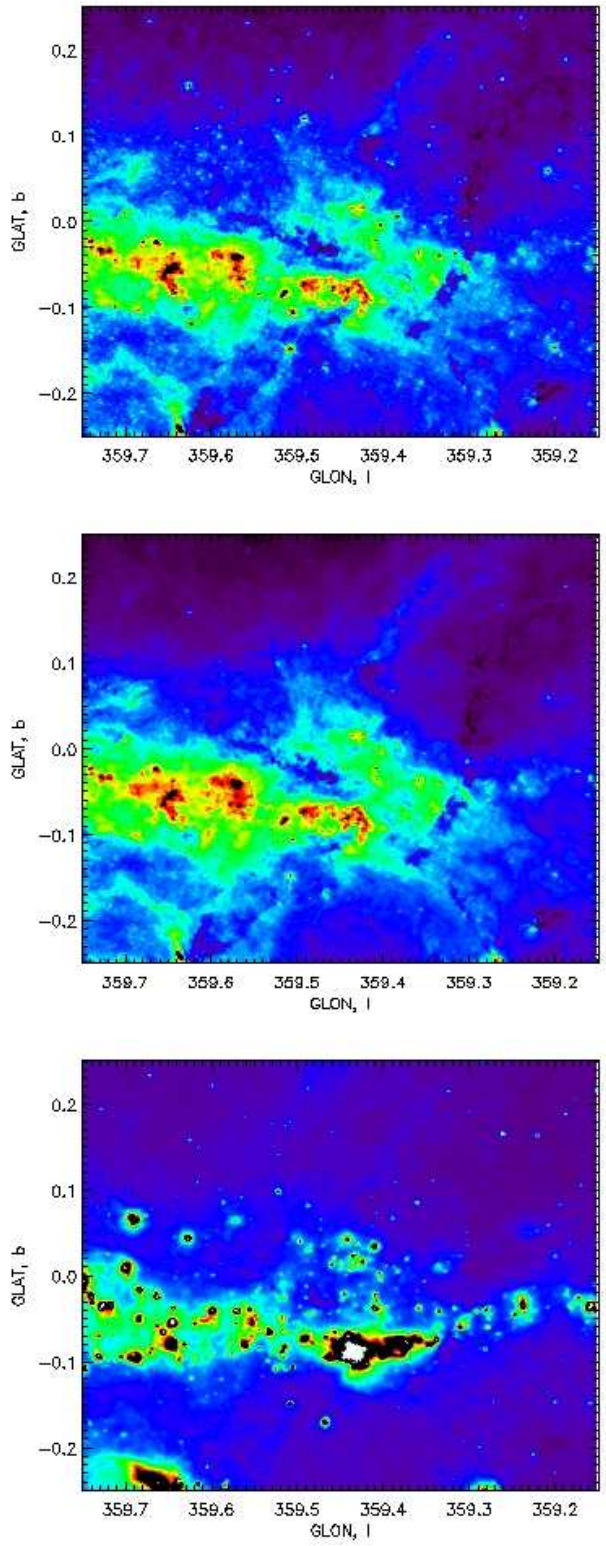

Figure 4.17: Same as Fig. 4.14 but of the Sgr C region [5.8μm (top), 8.0μm (middle), 24μm (bottom)].

4.2.4 The GCA

The Galactic Center Arc (GCA) as observed with the Spitzer/IRAC (namely chs 3 and 4, 5.8 μm and 8.0 μm respectively) are remarkably similar (see Fig. 4.18). The 'arched' filaments of the GCA are particularly distinct. Of the two main components of the 'arched' filaments, the top filament is less luminous than the bottom one. They do not appear to originate at the GC directly, but do emanate from the confused Sgr A complex. There is also a vertical structure just to the east of the GC at about b=360.02 that may join with the top-most arched filament, crossing over the region in an arc. The bottom arched filament splits into two components at (l,b) = (361.16,0.03), this is at about where it joins the dim component of the 'vertical' filaments. Consistent with the non-thermal assessment of the 'vertical' filaments, they do not appear in the IRAC observations.

The brighter regions of the Galactic Center (namely Sgr A and parts of the GCA) were masked out in the Spitzer/MIPS 24 μm map so as not to overexpose the image. There are a few, specific differences in the 24 μm MIPS map from the IRAC maps, not including the masked region. The southern part of the 'vertical' filaments can clearly be seen. Indeed, they form a structure that appears to be a near-closed loop of emission with the 'arched' filaments, a connection between these two structures not seen at 5.8μm and 8.0μm. There is also an arching structure that arcs east and south down from the GC complex connecting with the now curving southern part of the 'vertical' filaments. However, the curving southern filament overshoots this structure, expands and terminates on a hotspot of emission. This termination 'hotspot' does appear in the IRAC ch3/ch4 maps as a diffuse cloud.

There are structures further east from the 'vertical' filaments observed in all three IR maps. They lack filamentary structure, appearing as diffuse clouds with hotspots, but their nebulous structure, in bulk, is parallel to the vertical filament region. This region is seen to increase in intensity from 5 μm, through 8 μm, to 24 μm.

The parallel, straight emission feature nearly directly above SgrA at (l,b)=(360.0,0.13) is thought to be a limb brightened cylindrical channel (Morris *et al* 2006), evidence for the torsional Alfven wave responsible for the DHN structure (see above). However, there is considerable foreground absorption coincident with this structure (observed as a dark cloud immediately to the West), and there is not a similar, symmetrically situated structure below the galactic plane, since it would be expected that such a wave would propagate north and south equally. This 'channel' appears as a round, diffuse but hotspot like emission structure in the 24 μm MIPS image.

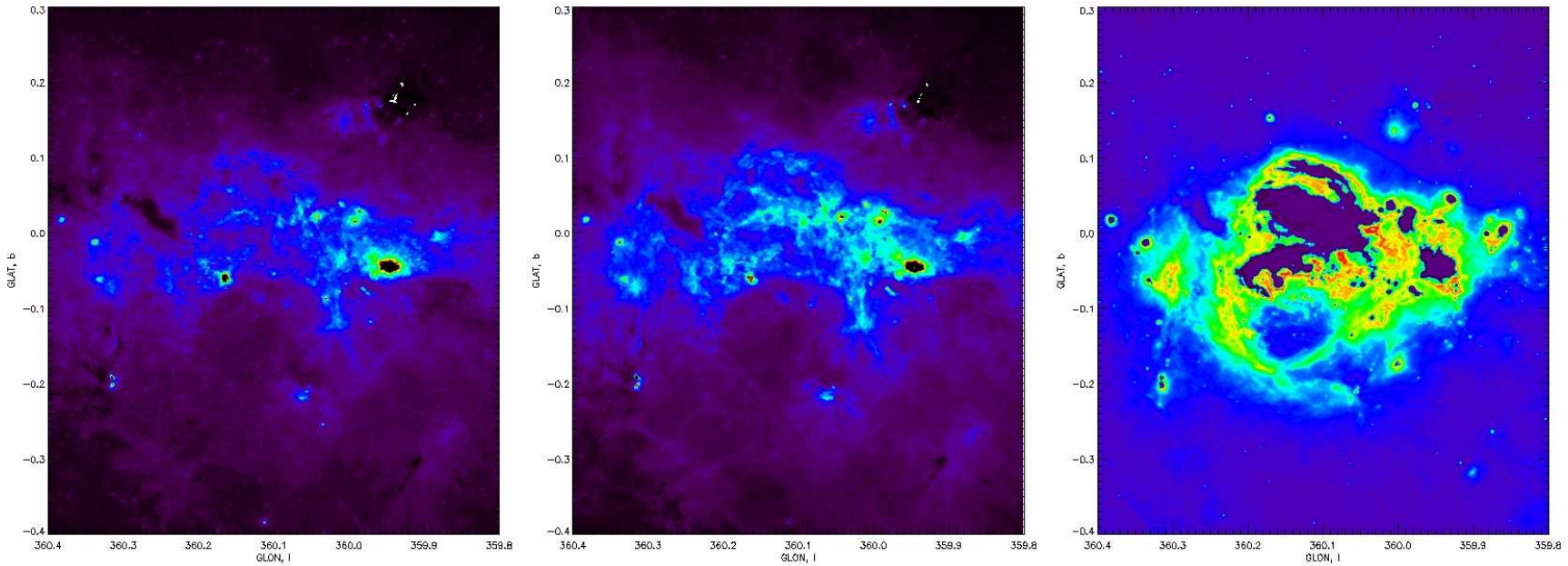

Figure 4.18: Same as Fig. 4.14 but of the Galactic Center Arc (GCA) region, [5.8μm (left), 8.0μm (center), 24μm (right)].

4.2.5 NRFs

Almost by definition, the NRFs should have no IR counterparts, being all non-thermal emitters, their IR emissivity would be nil. This is indeed the case, as there are no structures in the IR images we acquired that have obvious, filamentary counterparts to the NRFs.

4.3 Chandra X-ray survey image

The Galactic Plane at the Galactic Center was surveyed with the Chandra X-ray Observatory by Wang *et al* (2002). The survey extends to about ±0.4 above and below the galactic plane, and about ±1 degree East and West of the galactic center. The data were mosaicked from 30 pointings, and were taken with the front-illuminated Advanced CCD Imaging Spectrometer (ACIS-I). The spatial resolution ranges from 0."5 on-axis, through 5" on the edge of the ACIS-I and as much as 10" on the diagonal edge of each pointing. The Chandra images consist of three different channels with energies of 1-3keV, 3-5keV, and 5-8keV.

The Chandra images were filtered using the RFT (see Fig. 4.19) to emphasize diffuse structure, since the focus of our analysis of the Chandra images is location of diffuse high temperature plasma. Apart from the detailed, high-resolution imaging of the Galactic Center, and the Sgr A complex itself, there are vertical, diffuse extensions East and West of the GC. These vertical extensions are centered at approximately l=360.3 and l=359.7. Note that the locations of the East and West spurs of the GCL are approximately located at l=360.2 and l=359.4. The X-ray and gamma-ray source, 1E1740.7-2942, also known as the Great Annihilator because of its positron-electron annihilation gamma-ray emission, see in Fig. 4.19 at l=359.1, is likely a galactic source (Bosch-Ramon *et al*, 2006), near the galactic center, but not *at* the galactic center.

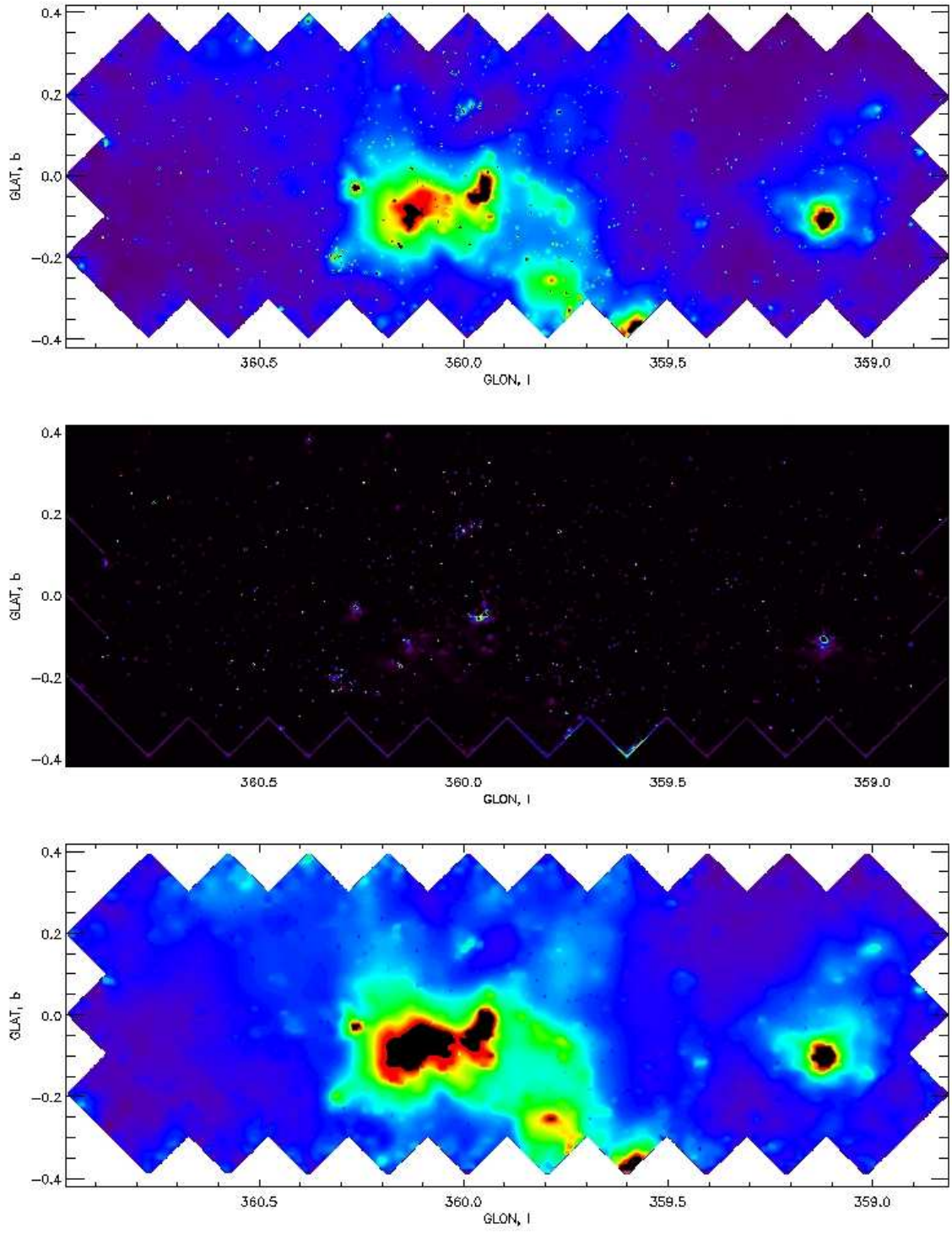

Figure 4.19: Chandra ch1 (1-3 keV band) image, with the RFT to mostly remove point source and to emphasize diffuse structure (filtering window was 3 pixels = 17"). (top) the original image, (middle) 'filtered' image, (bottom) 'open' image.

Chapter 5

Multiband correlations

5.1 GBT vs. VLA

5.1.1 The GCL-E and DHN

The bloby, knotted morphology of the GCL-E can be seen in the 'filtered' version of the VLA images. Along the N1 NRF, the HII cloud G0.17+0.15 is seen as a distinct hotspot in both the VLA and GBT maps (Figs. 5.1, 5.2 & 5.3). As the NRFs N1 and N3 meet at the GCL-E, they form another such blob. This hotspot corresponds to a GBT hotspot about at b=0.35.

The diffuse structure of the GCL-E is best seen in the 'open' VLA images from the applied RFT filter. In both 'open' VLA maps (Fig. 5.3), the 'paw' feature is clearly visible, with the split in the spur occurring in the same location in both VLA maps as our GBT map at about (l,b)=(0.11,0.43). However, despite separating at the 'paw', neither VLA map has further emission on the far side of the 'paw'. The VLA maps also correspond to our filtered Sofue map (Figs. 5.4 and 5.5), deflecting at the same location in the GCL-E.

5.1.2 The GCL-W

The GCL-W itself is nearly invisible in the 90cm VLA map, but is visible in the 20cm map. There is little distinct correlation between the 20cm VLA map and our 14GHz GBT map (Fig. 5.6). That there is a diminished emission at lower frequencies (90cm/20cm) indicates the thermal nature of the GCL-W as a whole.

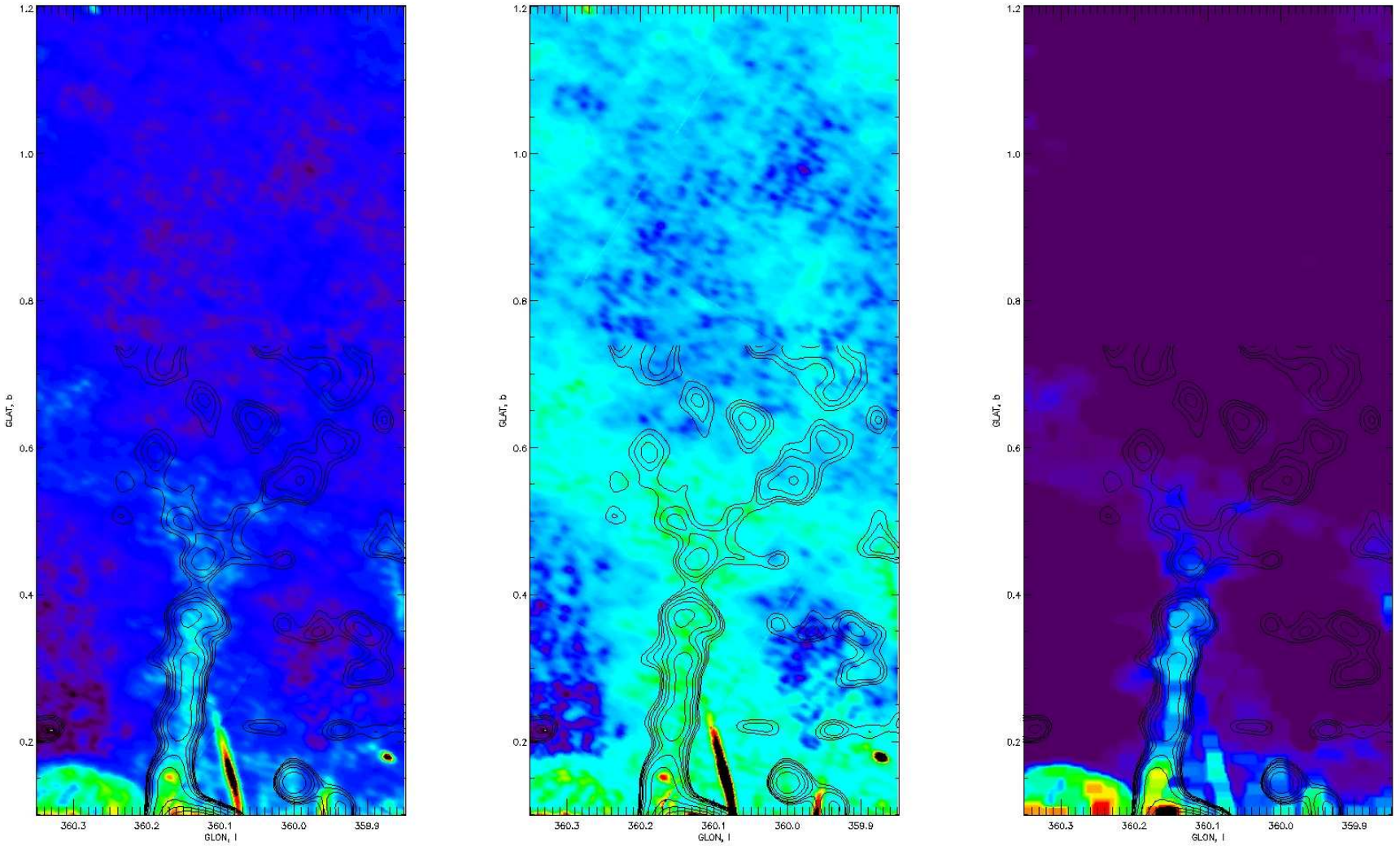

Figure 5.1: The 90cm VLA image of GCL-E region, filtered using the RFT (filtering window is 5 pixels = 0.'54.). (left) original image, (middle) 'open' image, (right) 'filtered' image. Note that the boxy artifacts in the 'open' image are due to the RFT. Our GBT data is plotted (contours) on top of the VLA data. The contour levels are [1, 1.05, 1.1, 1.2, 1.3, 1.5, 2, 3, 4, 5, 6, 7, 8, 9, 10, 15, 20, 25, 30, 35, 40, 50, 100] $\times$ 1% the maximum value of the GBT data.

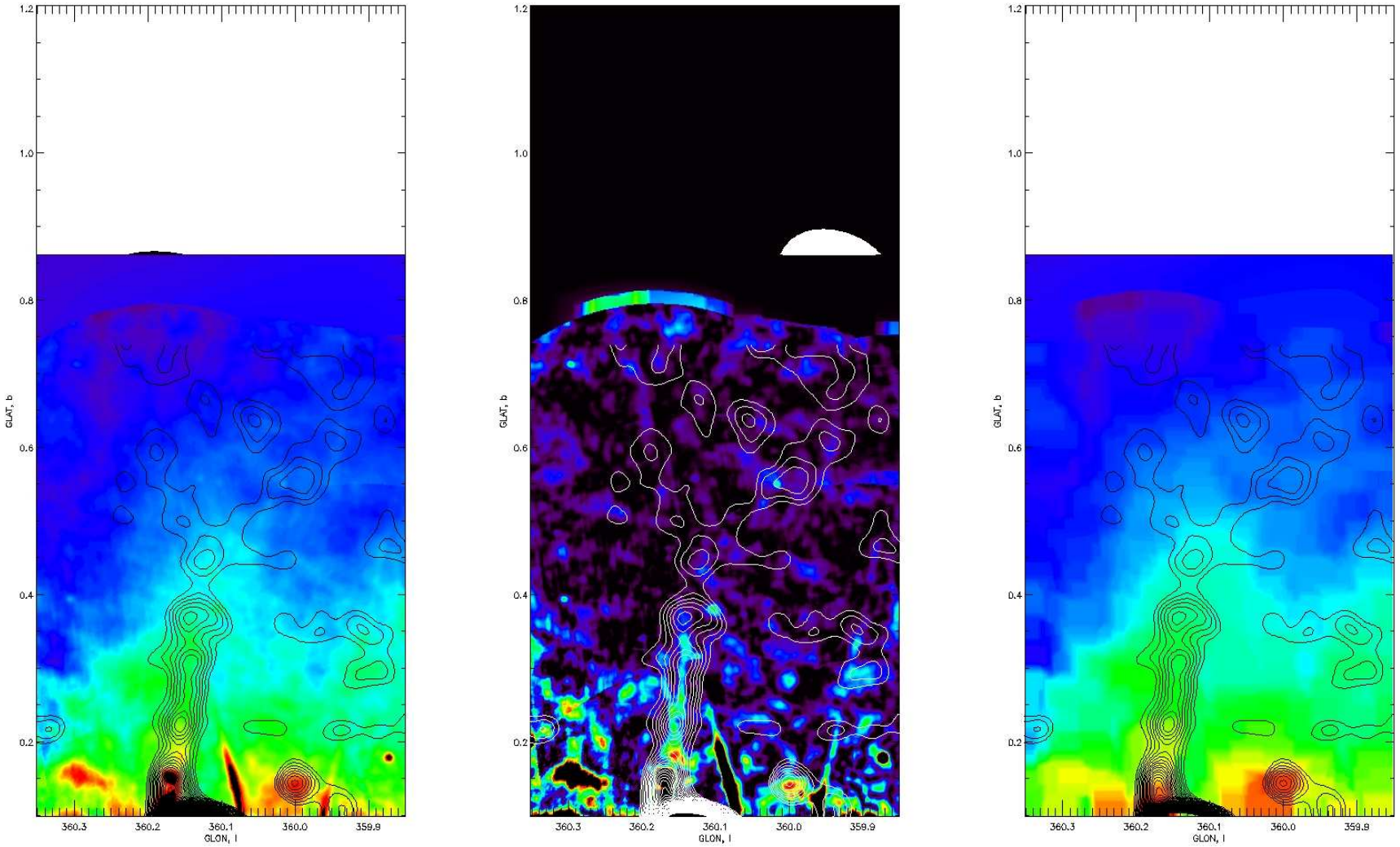

Figure 5.2: Same as Fig. 5.1 but the 20cm VLA image of the GCL-E region. Contours for our GBT image are the same as Fig. 5.1.

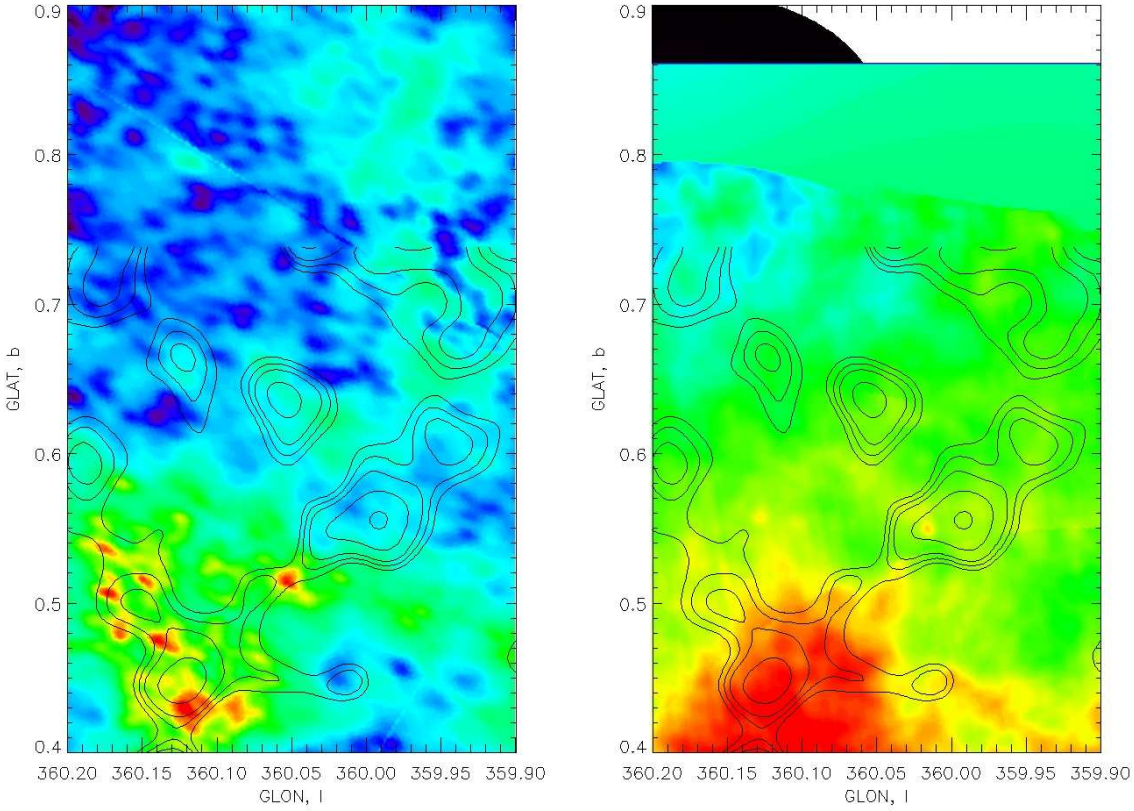

Figure 5.3: The Double Helix Nebula region, with the 'paw' feature in our GBT map overlaid on the 'open' 90cm (left) and 20cm (right) VLA images. Contours for our GBT image are the same as Fig. 5.1.

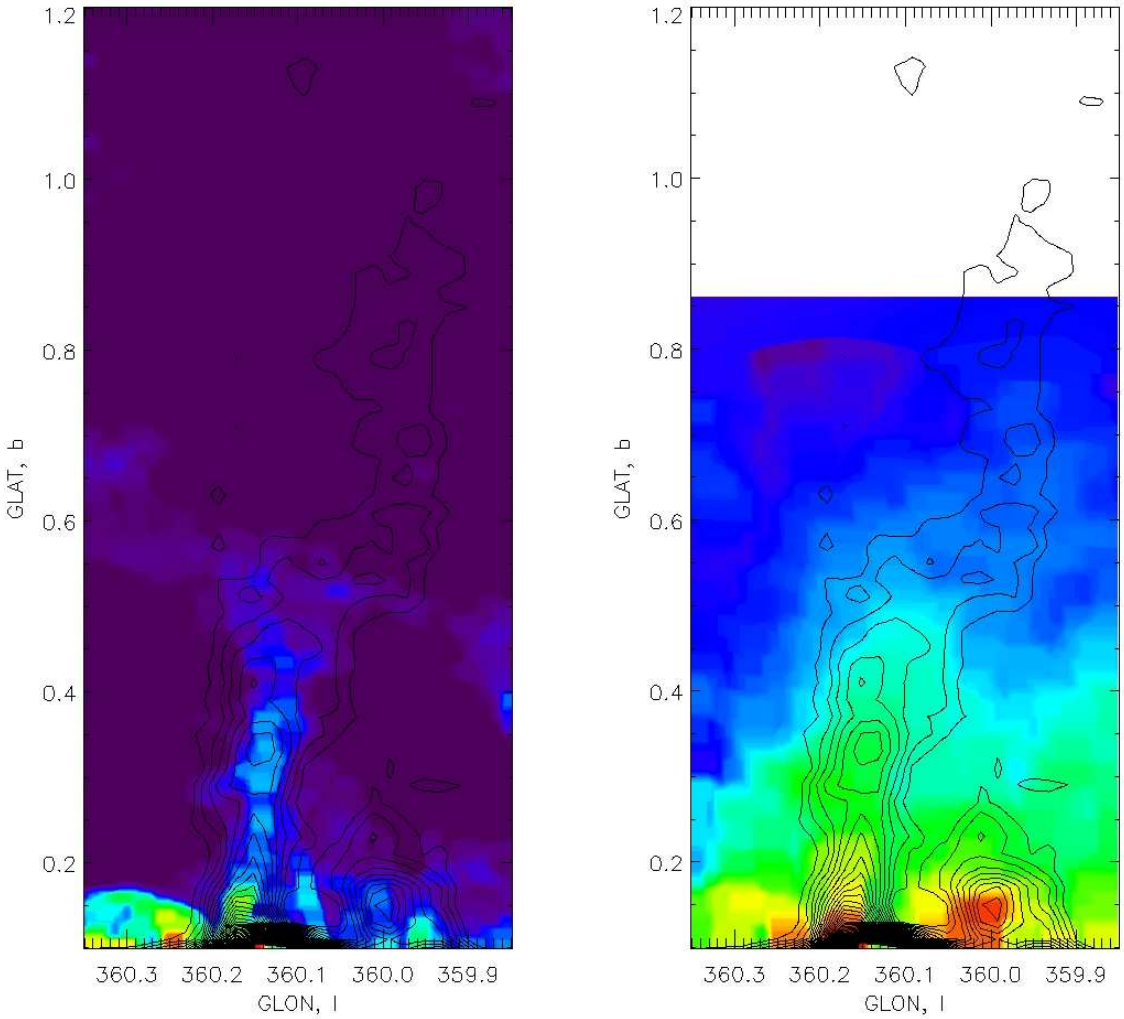

Figure 5.4: The VLA images of the GCL-E region, 90cm (left) and 20cm (right), with the Sofue map contours overlaid. The Sofue contours are 16.2mJy $arcmin^{-2}$ to 287mJy $arcmin^{-2}$ in steps of 6.9mJy $arcmin^{-2}$.

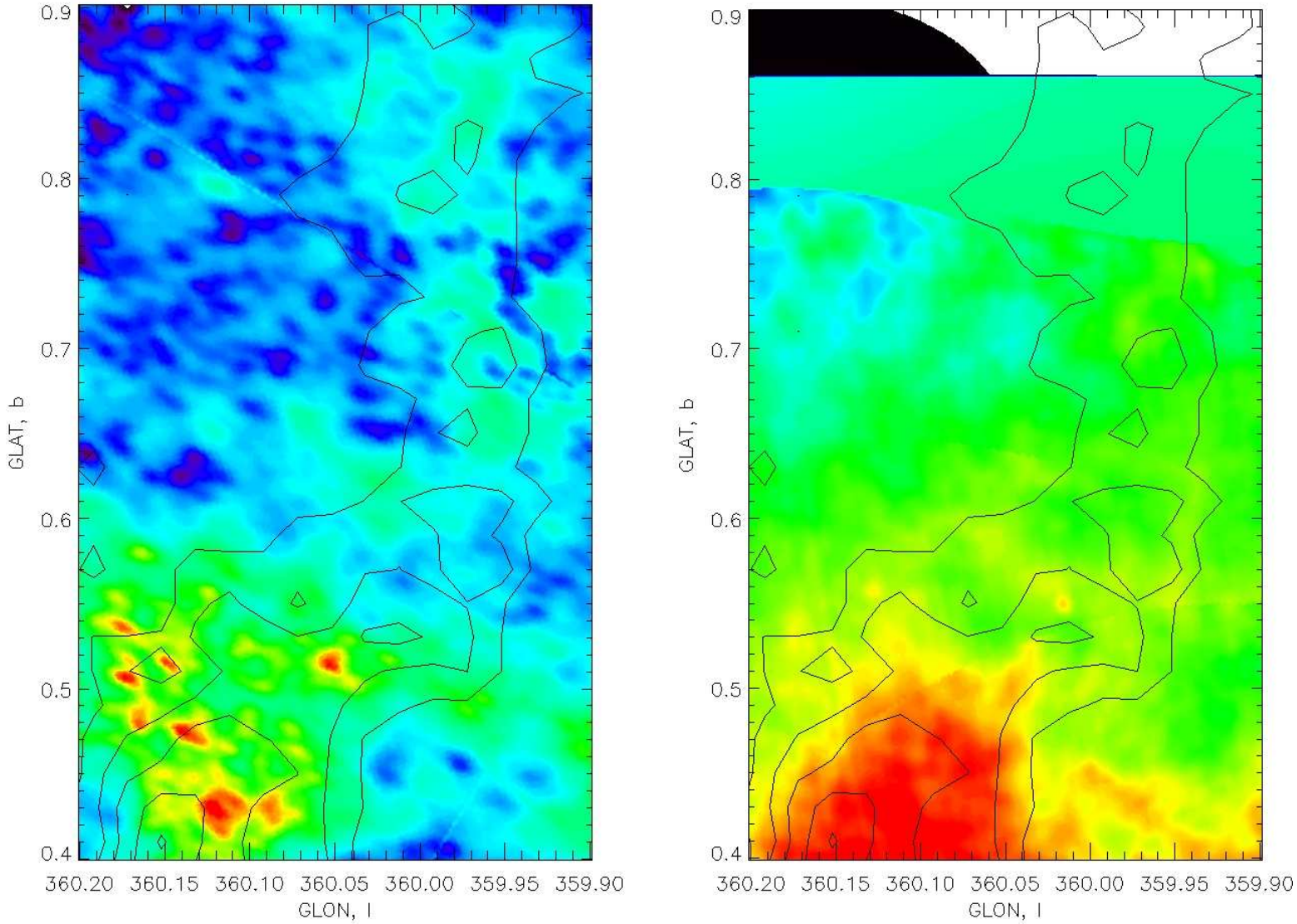

Figure 5.5: The zoomed in VLA images of the Double Helix Nebula region, 90cm (left) and 20cm (right), with the Sofue map contours overlaid. The Sofue contours are the same as Fig. 5.4.

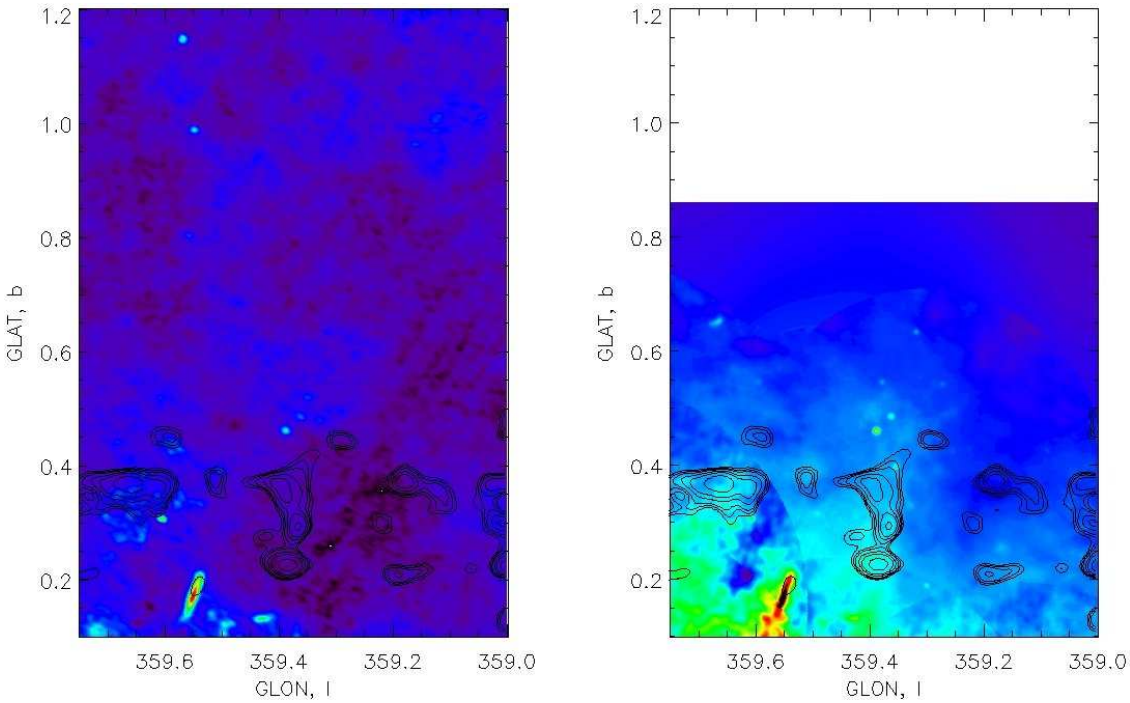

Figure 5.6: Same as Fig. 5.3 but the VLA images of the GCL-W region [90cm (right), 20cm (left)]. Contours for our GBT image are the same as Fig. 5.1.

5.1.3 The Galactic Center Arc (GCA)

Seiradakis *et al* (1985) and Tsuboi *et al* (1986) observe an S-shaped, polarized structure above and below the GCA. Above the GCA the polarized cloud curves away from the GC, and below it also curves away from the GC. The GCA proper curves inward (towards the GC): the center of curvature is beyond (farther west) of the GC. This change in curvature is seen in the southern extension of the GCA, in the 20cm VLA map, where the emission coming out of the southern end of the 'vertical' filaments of the GCA turns away from GC. This is not seen in the 90cm VLA map, indeed the 90cm looks more like a plume or lobe blown in the ISM (for the southern extension). It is likely that this polarized feature is connected with the GCA, but the estimation of curvature is premature given that it is only associated with the polarized material, but the continuum emission does not support the Southern curvature. In the north polarized feature, which is essentially the Eastern spur of the GCL, the bend in curvature in the Seiradakis' map is likely the manifestation of the kink in the GCL-E observed in all radio maps where the GCL-E is interacting with the DHN (see below). Unlike our GBT map, in the VLA maps, the connection between the GCA and the GCL-E is not a constant ridge of emission. There is a distinction between the N1 NRF and the 'vertical' filaments of the GCA as the N1 filament passes through (and/or around) the HII

region G0.17+0.15.

In our GBT map, the dual nature of the 'arched' filaments is clearly coincident with both VLA maps 'arched' filaments' emission (see Fig. 5.7). Along the length of the 'vertical' filaments, the 'sickle' radio source is clearly distinguished in our GBT map. The several additional radio sources to the east of the 'vertical' filaments also have distinct counterparts in our GBT map. There is no VLA counterpart to the northern extension of the SgrA complex located at (l,b)=(360.0,0.15). This is referred to below as the 'channel' thermal IR structure observed in the Spitzer maps.

5.1.4 The Non-thermal Radio Filaments (NRFs)

In general there are no obvious associations between the NRFs as observed in the high-resolution VLA maps and our GBT 14GHz data, with a few notable exceptions (see below). The non-detection of the NRFs at higher frequency (14GHz) is likely due to a combination of effects: 1) some may not be detected due to resolution constraints; however, 2) other non-detections correspond to a steep (non-thermal) spectrum, or a cutoff frequency below 14GHz. Note, we are using the convention of measuring spectral index as $S \sim \nu^{-\alpha}$, thus $\alpha > 0$ is non-thermal and $\alpha < 0$ is thermal, in general.

To test the resolution issue (1) the 20cm VLA map was convolved with a 2' beam (comparable to our final GBT map) so any effects or loss of signal due to resolution are isolated (see Fig. 5.8). In the convolved VLA image, the emission from the N2 filament is still detected, although it loses the morphology identifying it as a NRF. If the convolved VLA map were at the original resolution observed, the N2 filament would not be characterized as a NRF. However, the fact that there is no detectable emission in the GBT image (even at the 1σ level quoted in sec. 3.2) signifies it as a non-detection at 14GHz. Given the *a priori* knowledge that this *is* a NRF makes the non-detection at 14GHz likely a spectral consideration (2). The dimmer and smaller NRFs (e.g. N5) all but disappear in the convolved 20cm VLA map.

In contrast to the non-detection of the N2 filament, the C3 NRF, which is detected in the convolved 20cm VLA map, yet registers weakly at a 2σ level in our GBT map (see Fig. 5.10). Therefore, it may be possible that the stronger, perhaps less steep spectrum NRFs might show up at 14GHz in a deeper map. In the filtered Sofue map, the C3 NRF also has a counterpart to the 20cm VLA map (see Fig. 5.9). This is seen as an enhancement to the east of the base of GCL-W, though it is unlikely to be directly interacting with the GCL-W. In fact, the detection of the C3 filament (7σ above the background of the filtered Sofue map) leads to confusion about

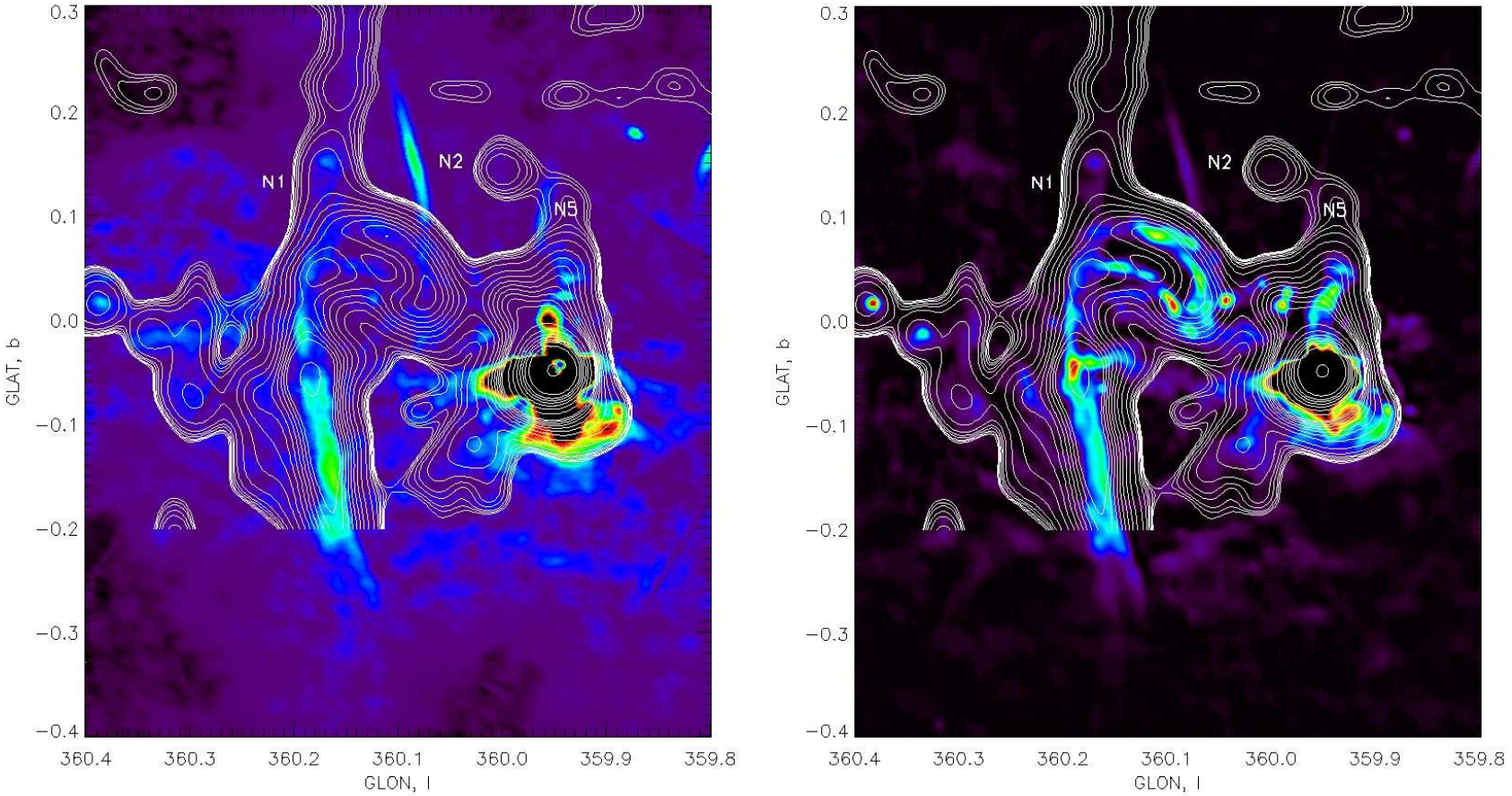

Figure 5.7: The RFT filtered 90cm VLA image (left) and 20cm VLA image (right) of the Galactic Center Arc region, with our GBT 14GHz data overlaid in contours. GBT contours are the same as in Fig. 5.1. The NRFs N1 and N2 are labeled. Note the absence of the 'channel' thermal counterpart in the VLA images as opposed to the GBT contours.

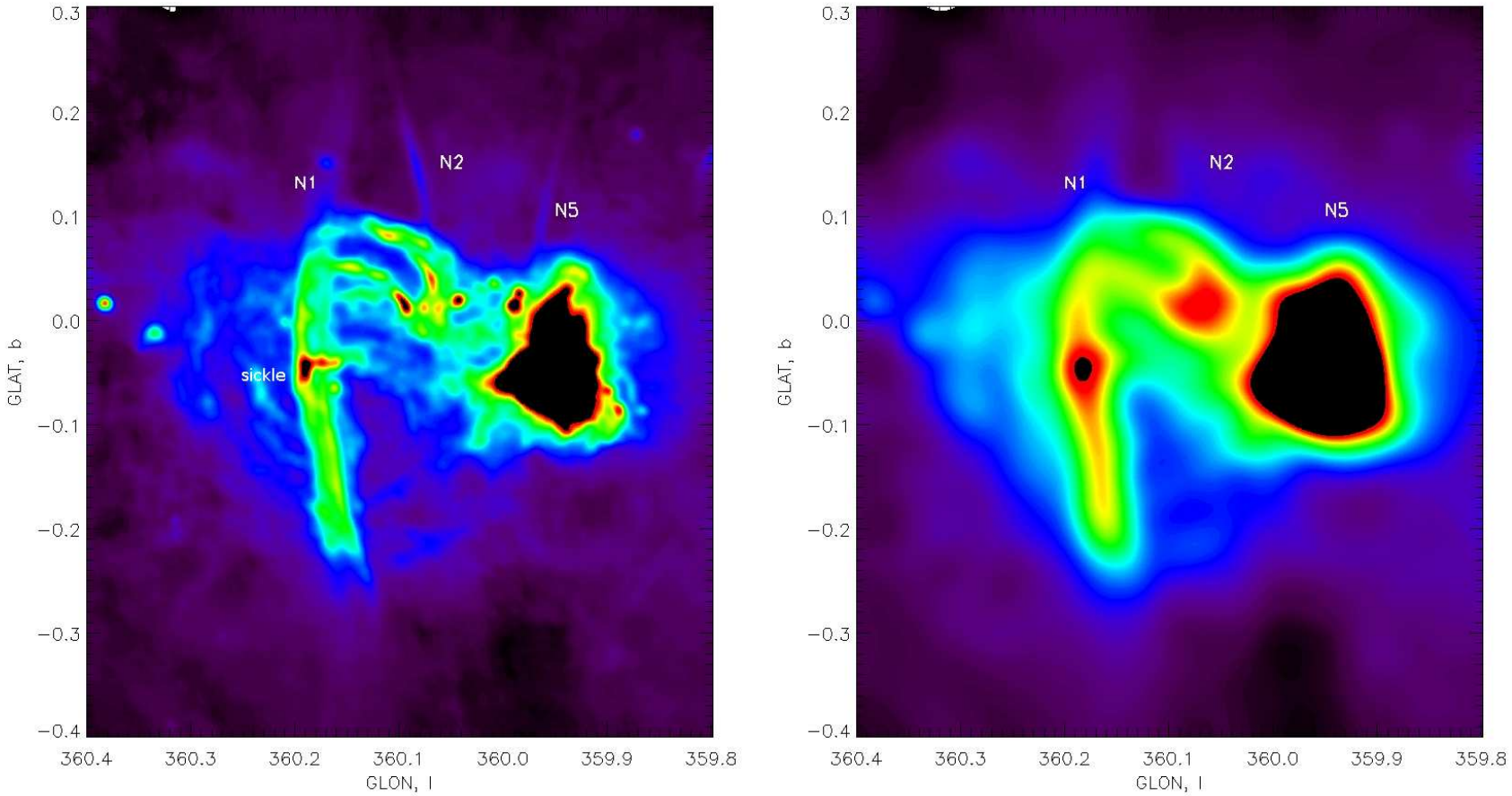

Figure 5.8: The comparison between the original 20cm VLA image (left) and the 20cm VLA image convolved to a beamsize of 2' (right), comparable to the beamsize of our GBT image. Note that the only significant filamentary structures that remain observable in the convoled image are the N1 and N2 NRFs. Note, for instance, the complete absence of the N5 filament in the convolved map.

the structure at the base of the GCL-W, making it appear wider, and more bent, than it likely is.

Similarly, the C1 filament touching SgrC is a possible marginal detection in both our GBT (again, weakly, at 2σ) and filtered Sofue maps (14σ). The C1 filament proceeds directly into the Western spur of the GCL (Fig. 5.10). Like our 14GHz GBT map, the western spur appears detached from the galactic plane in our filtered Sofue map. However, this apparent detachment only appears when the Sofue map is filtered with RFT (see Fig. 5.9).

For a non-thermal, steep spectrum source, the intensity is inversely proportional to a power of the frequency, so as the frequency increases the emission decreases. Also, with synchrotron emission, the spectrum may dramatically cutoff at higher frequencies. So, if there is emission at 20cm (1.4GHz), at a higher frequency (14GHz) there should be less emission from a continuous power law. If there is a cutoff at high frequency (between 1.4 and 14GHz) a source could easily go undetected by the GBT at 14GHz. The stated sensitivity of the GBT using the Ku-Band receiver, with a 3GHz bandwidth, observing a single (continuum) channel is about $0.2 mJy/arcmin^2$. But, given the atmospheric interference (as evidenced by the stripes in our map, Fig. 3.1) , a conservative estimate of $10 mJy/arcmin^2$ will be used to limit the unobserved NRFs.

If the filaments have the same spectral index from 5GHz to 14GHz as they do from 1.4GHz to 5GHz, then extrapolated flux density at 14GHz can be calculated. If this is greater than the lower limit of observable emission in the 14GHz map, *and* the filaments is undetected at 14GHz, then a spectral cutoff may be inferred. By using the noise figures we can also calculate an upper limit to the steepened spectral index at this point.

The total flux density of the N2 filament is 1346 mJy at 1.4GHz (Yusef-Zadeh *et al*, 2004), and covers an area of about $10 arcmin^2$ (measured using our IDL routine, AREA), thus has an average flux density of $135 mJy \cdot arcmin^{-2}$. This gives a limiting spectral index of +1.1, which, while steep, is reasonable. The peak flux density for the N2 NRF in the 90cm (333MHz) map (measured directly from the map) is $363 mJy \cdot arcmin^{-2}$, thus the $\alpha_{1.4GHz}^{333MHz}$ is 0.69, thus the cutoff spectrum must be between 1.4GHz and 14GHz, since the spectral index $\alpha_{14Ghz}^{1.4GHz}$ is so much steeper than the $\alpha_{1.4GHz}^{333MHz}$ spectral index.

The total flux density of the C1 NRF is 1204mJy at 1.4GHz (Yusef-Zadeh *et al*, 2004) covering an area (not including the connected C5 filament) of about $10 arcmin^2$. This gives the limiting spectral index ($\alpha_{14GHz}^{1.4GHz}$) for C1 of 1.1, however, since the source *is* detected at 14GHz, the spectral index must be shallower. The spectral index ($\alpha_{1.4GHz}^{333MHz}$) for C1 is 1.1. To obtain the $\alpha_{1.4GHz}^{333MHz}$ spectral index, the peak flux density of the filament at 333MHz was compared to the mean flux

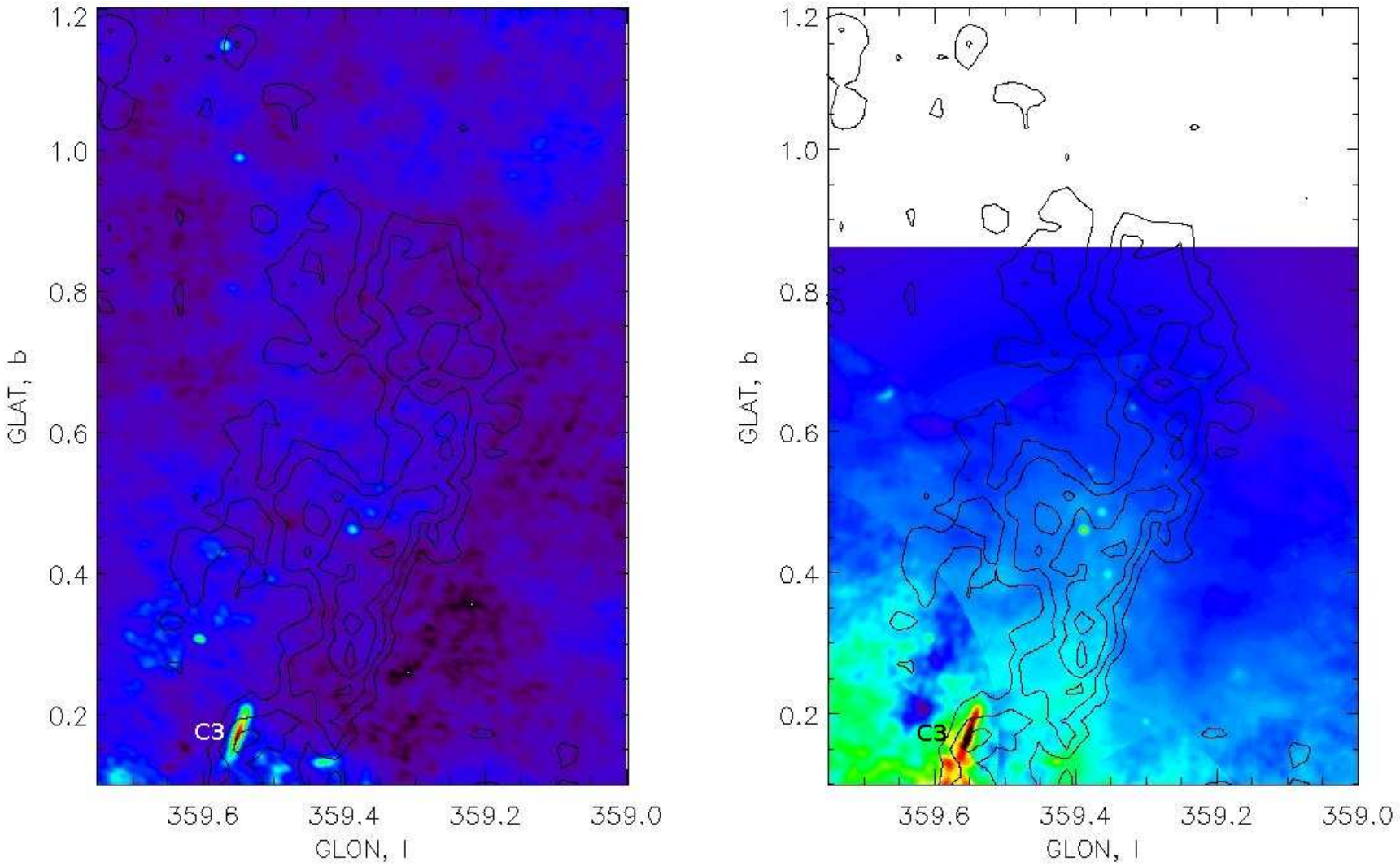

Figure 5.9: The VLA images of the GCL-W are presented, 90cm (left) and 20cm (right), with the RFT filtered Sofue data overlaid in contours. Radio contours are the same as Fig. 5.4. Note the bright NRF C3 at the base the GCL-W and its affect on the apparent width of the GCL-W as observed in the filtered Sofue data.

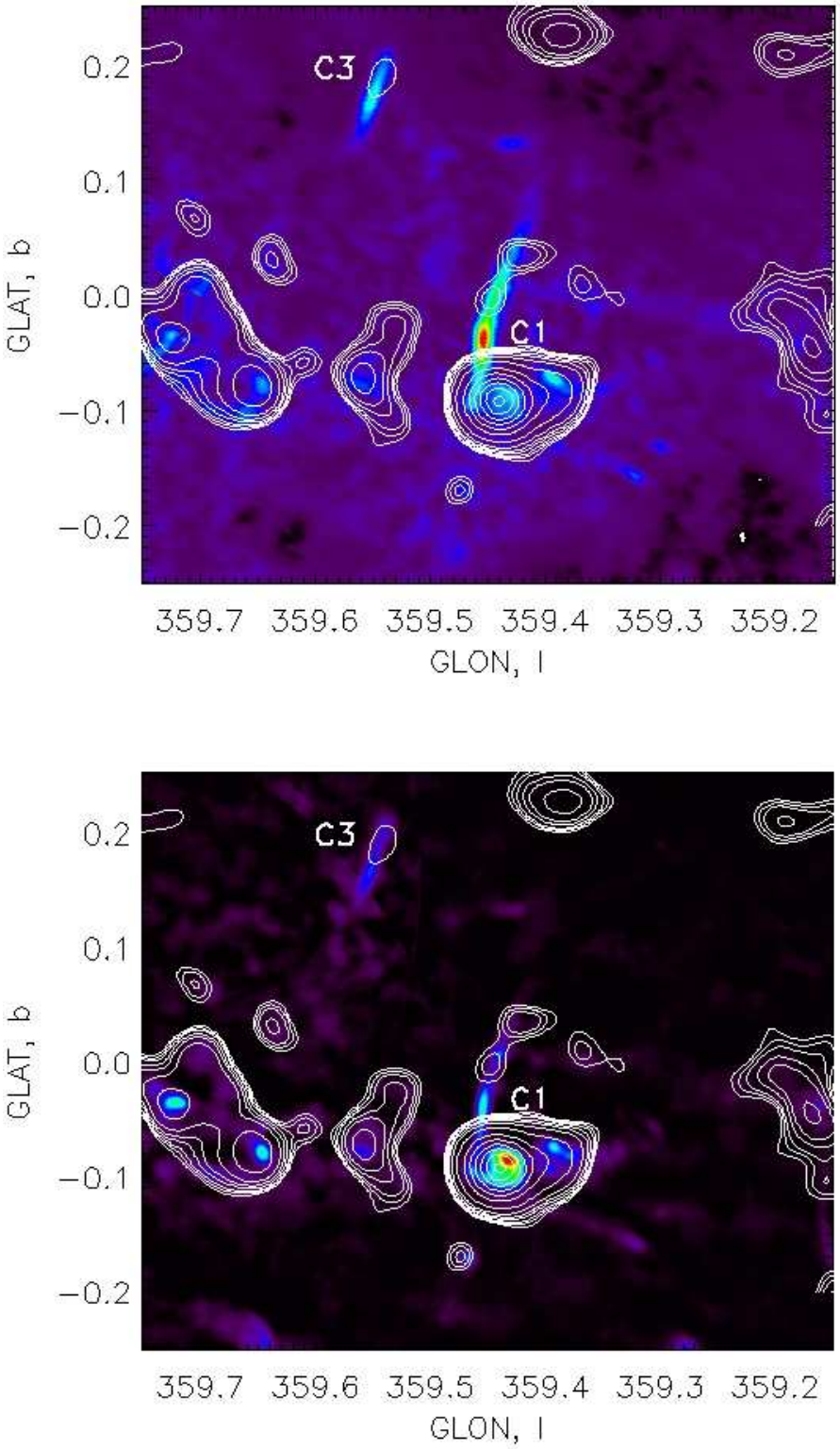

Figure 5.10: The filtered VLA images of the Sgr C region are presented, 90cm (top) and 20cm (bottom), with the 14GHz GBT data overlaid in contours. Contours for our GBT data are the same as Fig. 5.1. The NRFs C1 and C3 are labeled and their 14GHz GBT counterparts can be seen.

density at 1.4GHz, since the 1.4GHz (20cm) map did to have calibrated flux density (the values quoted for 1.4GHz are from (Yusef-Zadeh *et al*, 2004). However, given that the C1 filament is quite a bit brighter at the central peak than the periphery overall, and that it is more diffuse (and wider) than most filaments, comparing the peak flux density at 333MHz to the mean flux density at 1.4GHz to determine the spectral index of the filament will give a steeper spectral index than a more conventional method. Also, given that the filament is seen at 14GHz, its spectral index will be shallower than the limiting case, and this would indicate a generally constant spectral index from 333MHz (90cm) through 1.4GHz (20cm) to 14GHz (2cm).

For those NRFs that are detected at 10.5GHz and 14GHz, generally they only appear as elongated, barely detected point sources. They are likely only the brighter central parts of the NRF, the complete NRF being only observable at lower frequencies (e.g. the 90 and 20cm VLA maps). While it is likely that the ends/edges of the NRFs are smeared out to non-detection in our GBT and filtered Sofue maps due to their resolutions, the ends/edges of the NRFs also likely have a steeper spectral index. The peaks in the filaments are thought to be the site of energetic particle injection: HII regions interacting with the galactic magnetic field (Shore & LaRosa, 1999). The ends/edges of the NRFs likely have an aged high-energy electron population leading to a steeper spectral index than the peak, thus they would be more difficult to detect at higher frequencies. However, this is contingent on the rapid aging of the high-energy electron population. Since this may be a transient phenomenon there may be too little time to significantly age across the length of the filament. LaRosa *et al* (2000) find the spectral index more-or-less constant along these filaments. Since the spectral index is likely constant along the length of these filaments, the emission from the edges/ends as they become less dense and diffuse into the ISM are merely too dim to be seen with the GBT.

A jet model is proposed for the origin of the NRFs (Yusef-Zadeh *et al* 2004b) that is a scaled down version of the jets found in FRI galaxies and protostellar discs. There is a list of similar features, including the shape, linearity, and width profiles of these filaments that resemble the jets of FRI sources. The fact that there is not a bright hot spot at the terminator of the 'jet' is unlike the FRI sources. The accretion discs in proto stellar or star forming regions could make a similar jet feature that is observed as the NRFs.

Boldyrev & Yusef-Zadeh (2006) propose another theory whereby turbulence in the galactic center is responsible for amplifying the modest ($10\mu G$) ambient magnetic field into regions of stronger magnetic fields (0.1-1mG), but not requiring the much higher 1-10mG fields that previous

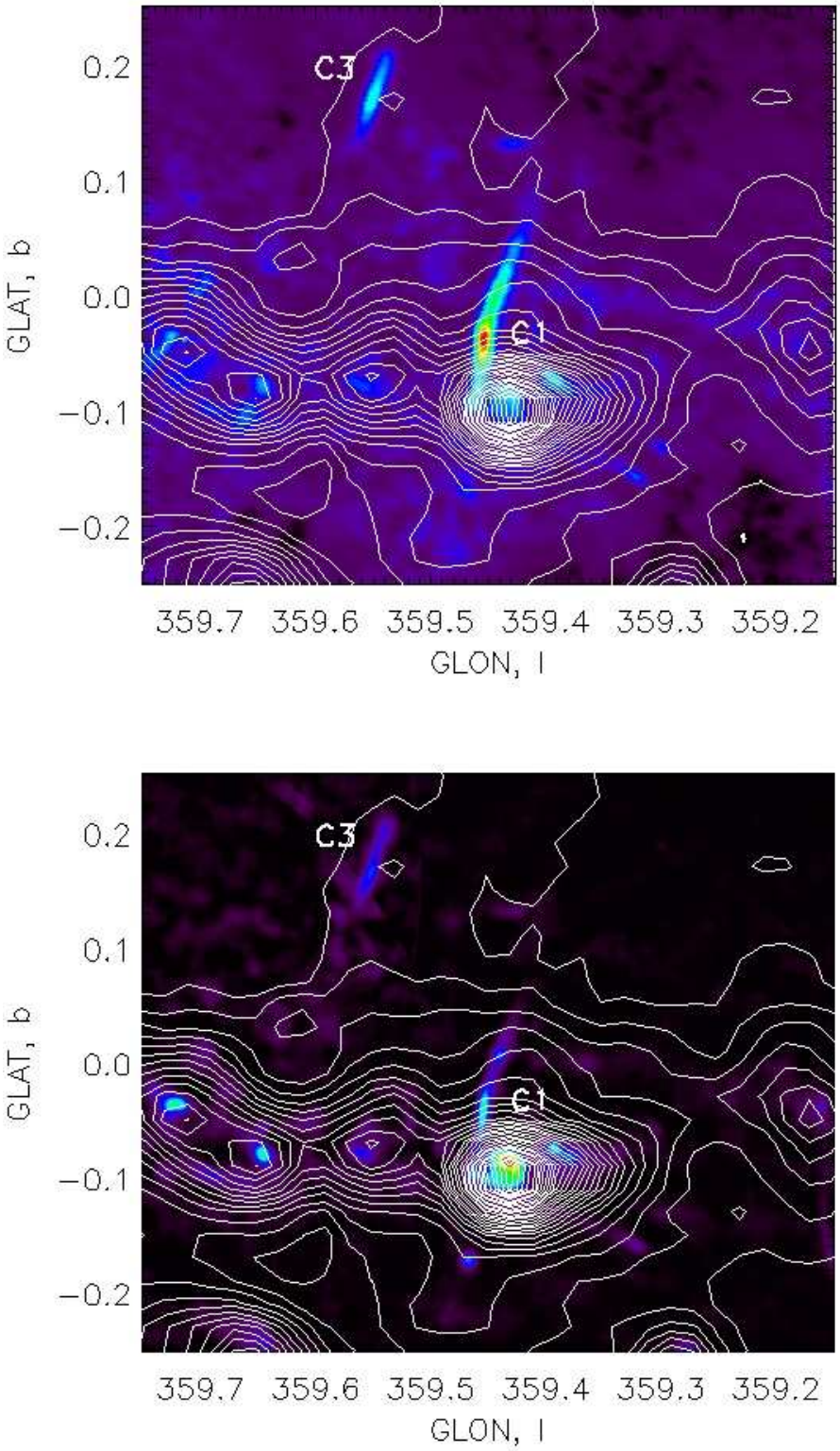

Figure 5.11: The filtered VLA images of the Sgr C region are presented, 90cm (top) and 20cm (bottom), with the filtered 10.5GHz Sofue data overlaid in contours. Contours for the filtered Sofue data are the same as Fig. 5.4. The NRFs C1 and C3 are labeled. Note the affect that C3 has on the width of the base of the GCL-W.

analysis asserts. The regions of stronger magnetic field have filamentary structure, thus being observed as the NRFs. However, there doesn't seem to be any explanation for why many to most of the filaments are observed nearly perpendicular to the galactic plane.

Neither model for the filaments is consistent with the fact that most of the filaments are perpendicular to the galactic plane. If explained via the stellar jet model, then all of the orientations would be random. However, the decreasing ambient density of the galaxy with increasing galactic latitude could be responsible for the orientation of the jets from protostellar discs, etc. In the case of the turbulence, the gradient of matter density may also make for a preferred orientation.

However, a model by Shore & LaRosa (1999) is bolstered by their predominately perpendicular orientation. The NRFs are formed from the magnetic wake from an HII region embedded in a hot, supersonic wind. As the HII cloud orbits, it streams through the nuclear wind and ambient magnetic field. The magnetic field infused plasma deforms around the HII cloud, concentrating the magnetic field and allowing particles to be accelerated to a relativistic, non-thermal population emitting synchrotron radiation. The magnetic wake would generally point away from the source of the nuclear wind, thus generally perpendicular to the Galactic Plane. In this picture the NRFs may be 'relics' of the type of interaction we have observed in the DHN (see Sec. 6.2.1).

To estimate the strength of the magnetic field in and around the NRFs from dynamical arguments (Yusef-Zadeh *et al*, 1987) (as opposed to spectral or emission arguments) the magnetic field is assumed to be in equipartition with the energy density. Also assuming that the magnetic pressure is balanced by the ram pressure of a gas cloud (presumably the $40km \cdot s^{-1}$ molecular cloud surrounding the galactic center) then there are two methods for obtaining similar magnetic fields. From dynamical arguments: the ram pressure is equal to the magnetic field pressure.

$$P_{ram} = 1/2 \cdot \rho \cdot v^2 \tag{5.1}$$

The density is $10^4 cm^{-3}$ and the velocity is about $15km \cdot s^{-1}$ (which is the half-width velocity of the $40km \cdot s^{-1}$ cloud), this leads to a ram pressure of $2 \times 10^{-9} Pa = 2 \times 10^{-8} dyn \cdot cm^{-2}$. The magnetic pressure is

$$P_{mag} = B^2/4\pi \tag{5.2}$$

Equating these gives a magnetic field of $7 \times 10^{-4} G$ which is about 1mG.

Using equipartition, which assumes that the magnetic energy and the high-energy particle energy responsible for the synchrotron emission are balanced, and also that the spectral index is

flat between 10^7 and $10^{11} Hz$ (10MHz-100GHz) yields an inferred magnetic field strength of about $2^{-4} G$, and a relativistic electron density of $3.2 \times 10^{-3} cm^{-3}$. Total radio flux of the radio arc is measured to be $\sim 100 Jy$ at 1.4GHz (Yusef-Zadeh *et al*, 1987). If NRFs are transient phenomena, they do not require a global magnetic field on order 1mG, but simply an enhancement of $\sim$ 1 mG. This relaxes the criteria for a global magnetic field in the galactic center (Shore & LaRosa, 1999).

5.2 GBT vs. Mid-IR

5.2.1 The GCL-E

The DHN begins to form at the position in our GBT map that bends in a bow shock pattern. The non-helical head of the DHN corresponds to a relative void in the radio emission (see Fig. 5.12). Then, on the far side of the 'radio-paw' feature, there is a radio hot spot. In the DHN this is coincident with the first visible helicity in the DHN, indicating the presence of a coherent, organized magnetic field. The DHN continues north, remaining east of the northern radio extension of the GCL-E as observed in both our GBT map and the filtered Sofue map (Fig. 5.13).

As observed only in the $24 \mu m$ Spitzer image, to the West of the DHN (Fig. 5.12) is a large non-thermal vertical projection that is just 'inside' (to the west) of the GCL-E. This is especially interesting since it is where the GCL-E spur (in our GBT map) bends at the 'paw' structure. The GCL-E in our filtered Sofue map appears to pass between this new non-thermal IR feature and the DHN. This feature does not appear in the $8 \mu m$ image thus indicating that it is a non-thermal feature, and has a $S \sim \nu^{-\alpha}$, positive spectral index. Measured against the $8 \mu m$ image, with little processing beyond that which is extracted from the "Post Basic Calibrated Data" (Post-BCD) archive, the spectral index is ~ 0.5, which implies non-thermal emission. The DHN itself appears to have an almost flat (0.05) spectral index, confirming that it is likely a thermal feature. In confirmation of the registration of the images, there is a point source observed in both the 8 and 24 μm maps, that also appears in our GBT map. This is at $(l, b) \sim (0.01, 0.45)$.

5.2.2 The GCL-W

It is evident from our higher resolution radio data (at 14GHz) and the very-high resolution Spitzer 24 μm images that the radio and IR emission *do not* correlate (see Fig. 5.14). However, as suggested by Uchida *et al* (1990, 1994), the edges of the two features do overlap. Indeed, in the filtered Sofue map (Fig. 5.15), the eastward outcropping at (l,b)=(359.43,0.47) extends into AFGL

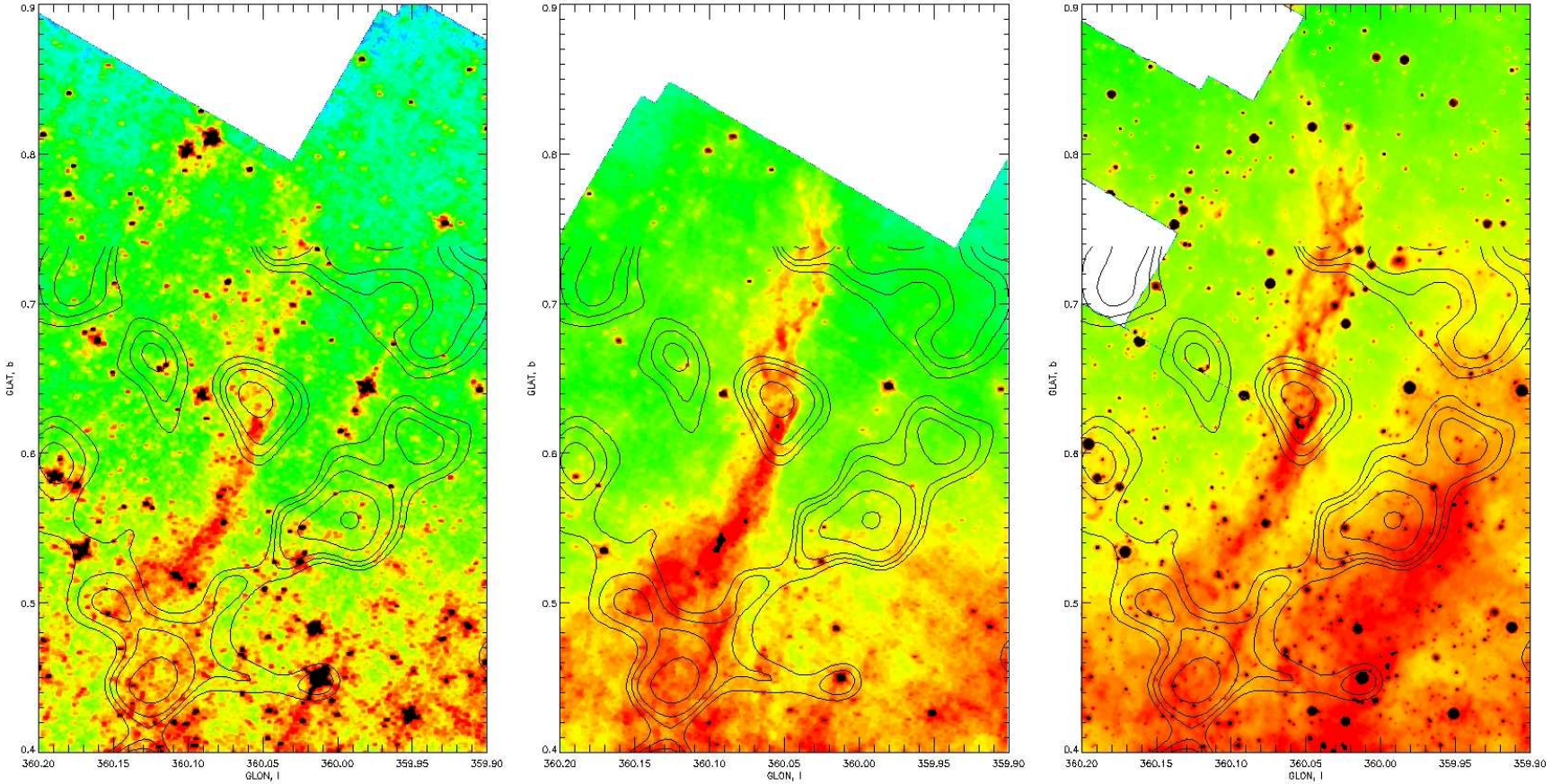

Figure 5.12: The three Spitzer images of the Double Helix Nebula are shown with our 14GHz GBT data overlaid in contours. (left) Spitzer/IRAC ch3 5.8μm 'open' image. (center) Spitzer/IRAC ch4 8.0μm 'open' image. (right) Spitzer/MIPS 24μm 'open' image. Contours for our GBT data are the same as Fig. 5.1.

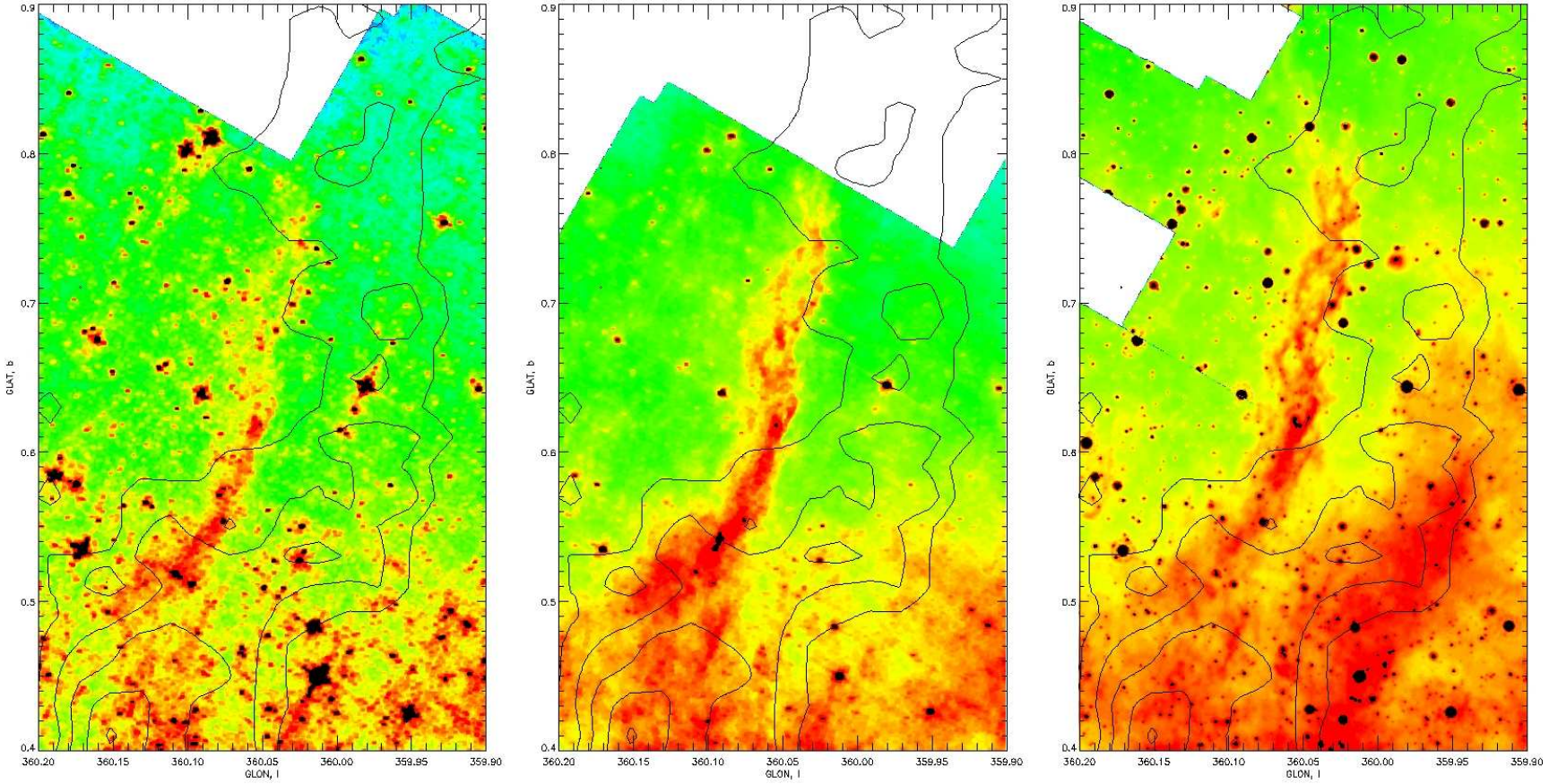

Figure 5.13: Same as Fig. 5.12 but with the filtered Sofue map overlaid in contours. Contours for the filtered Sofue data are the same as Fig. 5.4.

5376. In our 14GHz map, where the GCL-W flattens and ends is where AFGL 5376 extends itself westward, overlapping with the GCL-W. Uchida *et al* (1990, 1994) provide convincing velocity data to suggest that AFGL 5376 and GCL-W are associated given their common high positive (counter-rotating) associated velocities (as measured in CO-line emission). AFGL 5376 is associated with a CO12 line emission moving at $125km \cdot s^{-1}$ and the GCL-W is 'likely' associated with lower velocity $90km \cdot s^{-1}$ emission. The widening of the filtered Sofue map at b=0.4 is coincident with the IR feature AFGL 5376.

In both our GBT map and the filtered Sofue map, the edge of the radio ridge of GCL-W coincides with the location of the filamentary spurs in the 8 and 24 μm Spitzer images. Filaments (1) and (2), as an example, are seen to coincide with the edge of the filtered Sofue map. Indeed, the spur alters direction westerly at b=0.45 and abuts the IR filament. In our GBT map as well, the radio emission jogs west to come in contact with the second filament. Though Uchida *et al* (1990, 1994)) deduce that the IR emission and the radio emission were coincident, they are not; this ambiguity is cleared up with the new IR images and the higher resolution 14GHz radio image. They are not directly coincident, but are touching at the edges of detectable emission.

Uchida *et al* (1990, 1994) suggests that AFGL 5376 and the GCL-W are 'coincident,' and that they are interacting, as suggested by "the alignment of the outermost non-circular contours of AFGL5376 with the GCL." The correlation is based on the original Sofue 10.5GHz and the 25 μm IRAS maps of the region. However, given our higher resolution 14GHz GBT maps (higher than Sofue's) and the higher resolution Spitzer 24μm maps (higher than the IRAS map), these two features are not perfectly coincident.

5.2.3 The Galactic Center Arc (GCA)

The basic radio structure of the GCA consists of the 'arched' filaments and the 'vertical' filaments. The 'arched' filaments have a mid-IR component in all three of the Spitzer images we have obtained. The 'vertical' filaments have little-to-no IR component. However the IR components for the 'arched' filaments are interesting.

The IR counterpart to the 'arched' filaments of the GCA do not overlap with our GBT radio map (see Fig. 5.16). The 'arched' filaments in our GBT map decomposes into two components, just as the IR counterpart. That there are two 'arched' filaments in the radio and in the IR seems to confirm an association; however, the IR component is compressed against the northern edge of *both* radio 'arched' filaments (this can be seen especially well in Fig. 5.17 where the 20cm (1.4GHz)

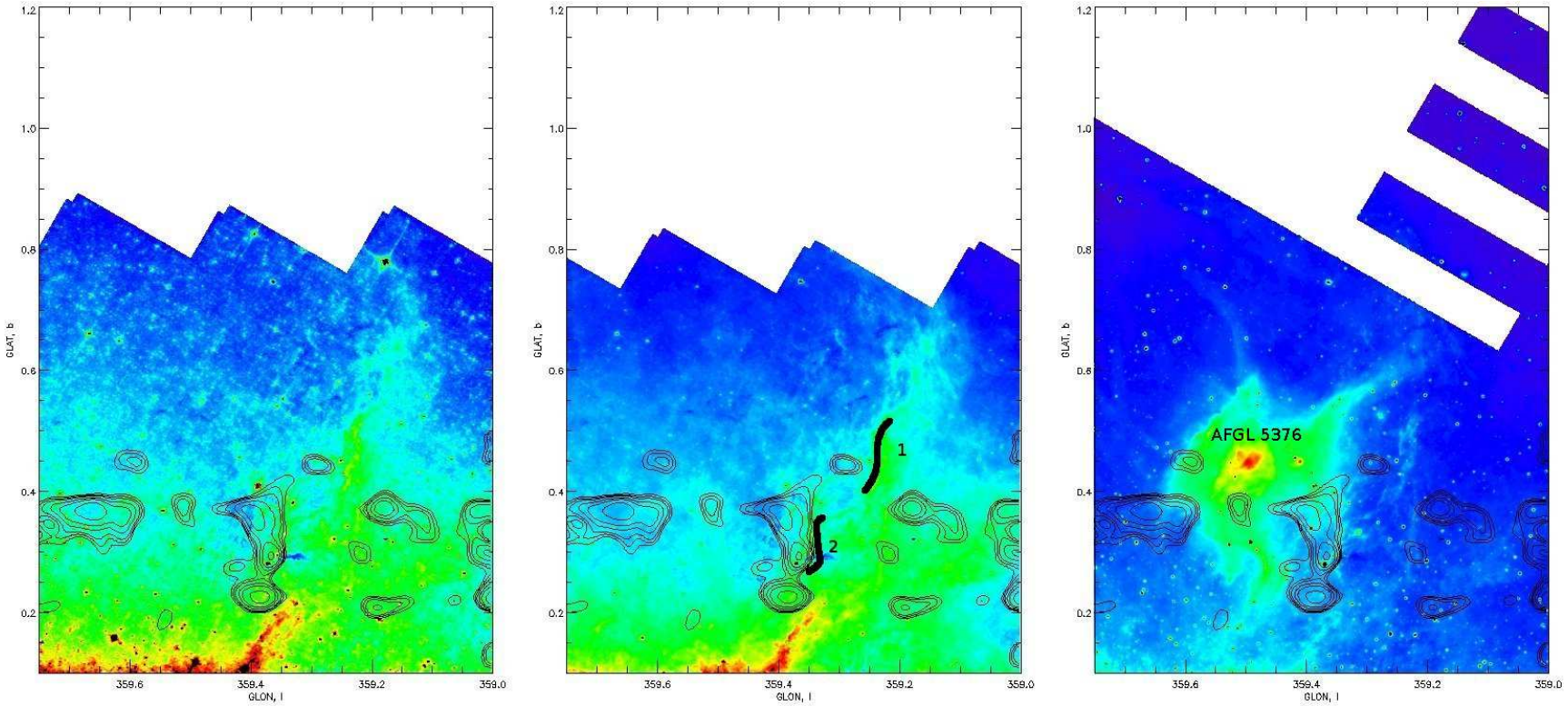

Figure 5.14: Same as Fig. 5.12 but of the GCL-W region. Filaments (1) and (2) are labeled in the (center) image. Contours for our GBT data are the same as Fig. 5.1.

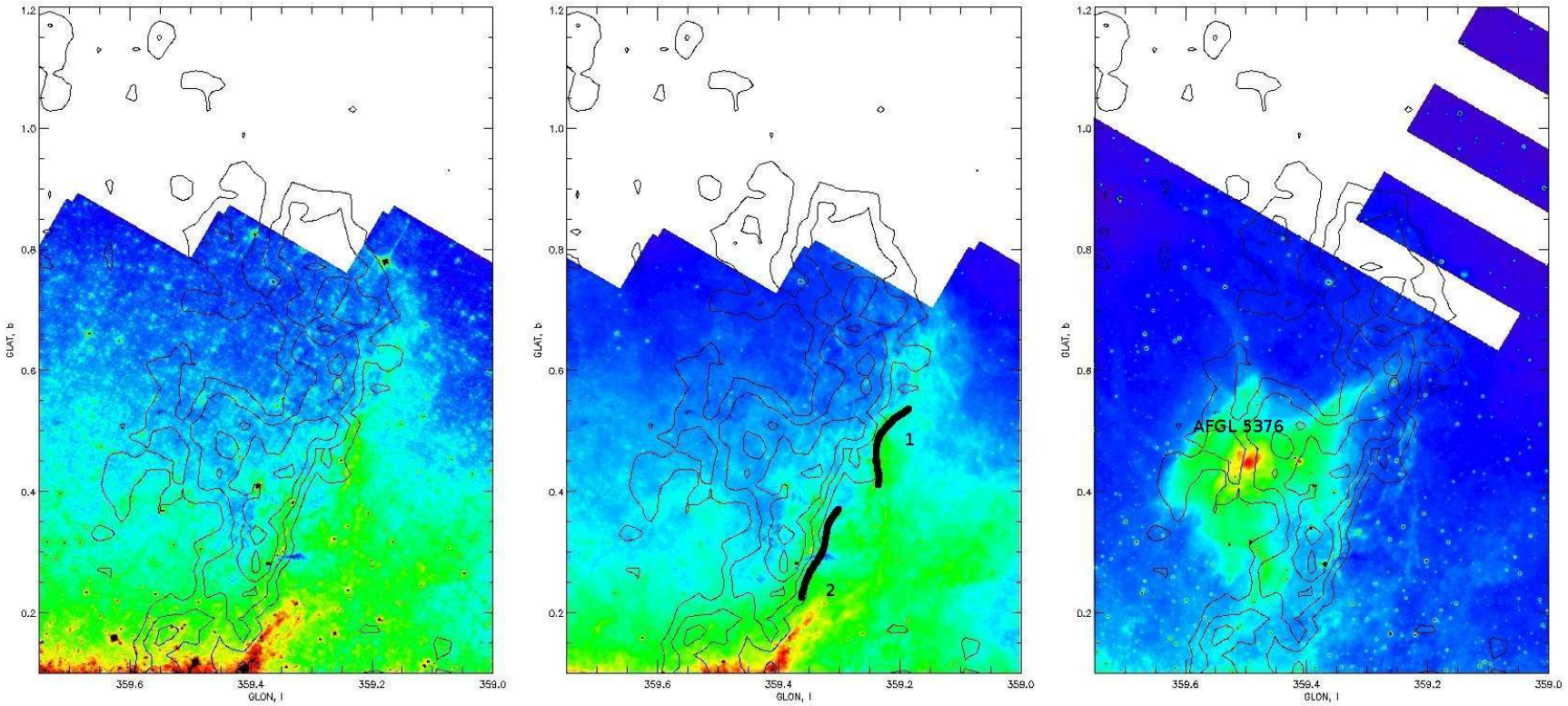

Figure 5.15: Same as Fig. 5.14 but with the 10.5GHz filtered Sofue data overlaid in contours. Contours for the filtered Sofue data are the same as Fig. 5.4.

VLA image is overlaid with the 8.0μm Spitzer image). This would be consistent with dust that is entrained in a shock propagating outward from within the GCA superstructure, though east of the Galactic Center itself.

5.2.4 The Filaments of the GCA observed at 20cm and 24um

Sofue (2003) filtered the 20cm VLA data (used here) to find a correlation between shell-like filamentary structures in the radio data and similar shell-like features in MSX 16-26 μm IR data. We have used the RFT to remove the 'vertical' filaments from the 20cm VLA image of the GCA to enhance radial filamentary structure (see Fig. 5.18). The filter was applied row-by-row, removing diffuse structure parallel to the 'vertical' filaments, using a filter size of 13 pixels or 1.1 arcmin. These radial structures are centered (in curvature) approximately at the 'sickle' radio feature (where the 'vertical' filaments cross the galactic plane).

Like Sofue (2003), these radial filaments correspond to the radial structures observed in the IR (here the Spitzer/MIPS 24 μm map). These evidently thermal filaments are evidence for previous epochs of outflow from the 'sickle' region. They are seen to deform in the direction of the galactic center, which is consistent with the higher density expected in that direction, as is the flattening and expanding east of the GCA, where expanding shells would be freer to expand out into less dense media. The filaments east of the 'vertical' filaments would correspond to the shells of previous outflows which are also seen in our GBT map.

5.2.5 Thermal 'channel' structure

The parallel 'channel' described above (Morris *et al* 2006) correlates with a northern projection out of the Sgr A complex (see Fig. 5.16). The northward projection bends sharply and terminates on the 'channel' structure as a sharp hotspot in our GBT map. The contours of the hotspot appear to blend with the northern projection out of Sgr A, so they are likely unrelated, and the overlap is due to resolution constraints. It is interesting that this 'channel' observed in the IR does not appear in the VLA images. This is consistent with the assumed thermal nature of these parallel structures.

5.2.6 A String of Thermal Point Source and the N2 NRF

There is a string of point IR sources in all three IR maps coincident with the N2 NRF (Fig. 5.19). This may be just coincidentally, but it is a string of four (4) point sources, exactly in line, and

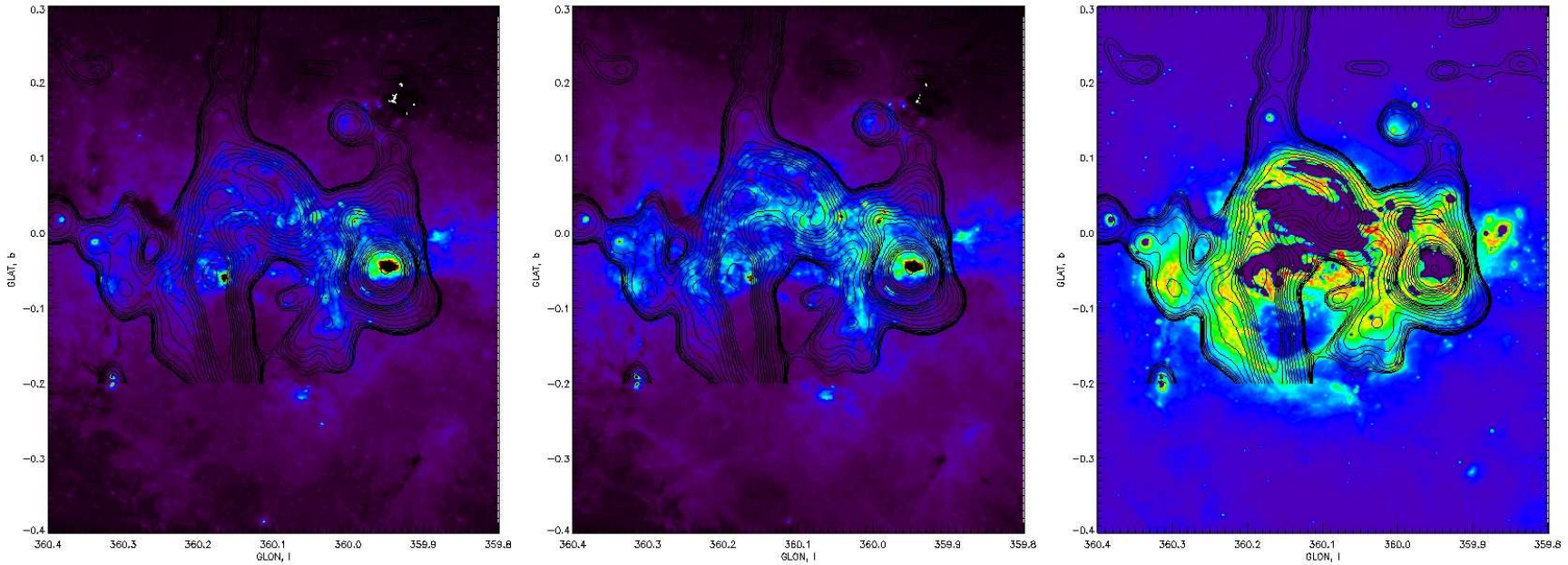

Figure 5.16: The three Spitzer images of the Galactic Center Arc (GCA) are shown with our 14GHz GBT data overlaid in contours. (left) Spitzer/IRAC ch3 5.8μm 'open' image. (center) Spitzer/IRAC ch4 8.0μm 'open' image. (right) Spitzer/MIPS 24μm 'open' image. Contours for our GBT data are the same as Fig. 5.1.

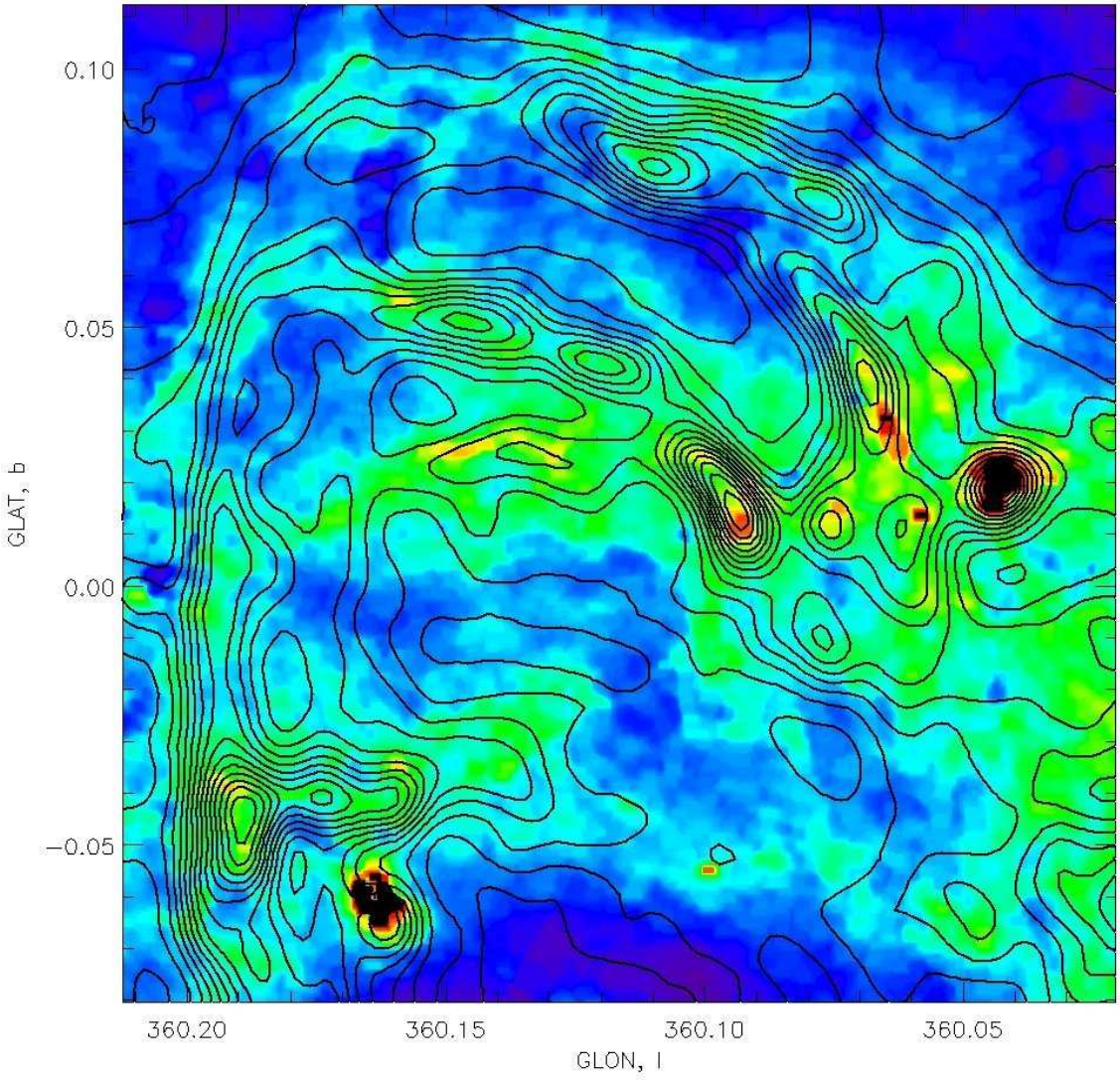

Figure 5.17: An enlargement of the association between the 'arched' filaments of the GCA as observed in the 20cm VLA image and similar filamentation in the 8.0μm Spitzer/IRAC image. The Spitzer map is in false-color, with the VLA contours overlaid.

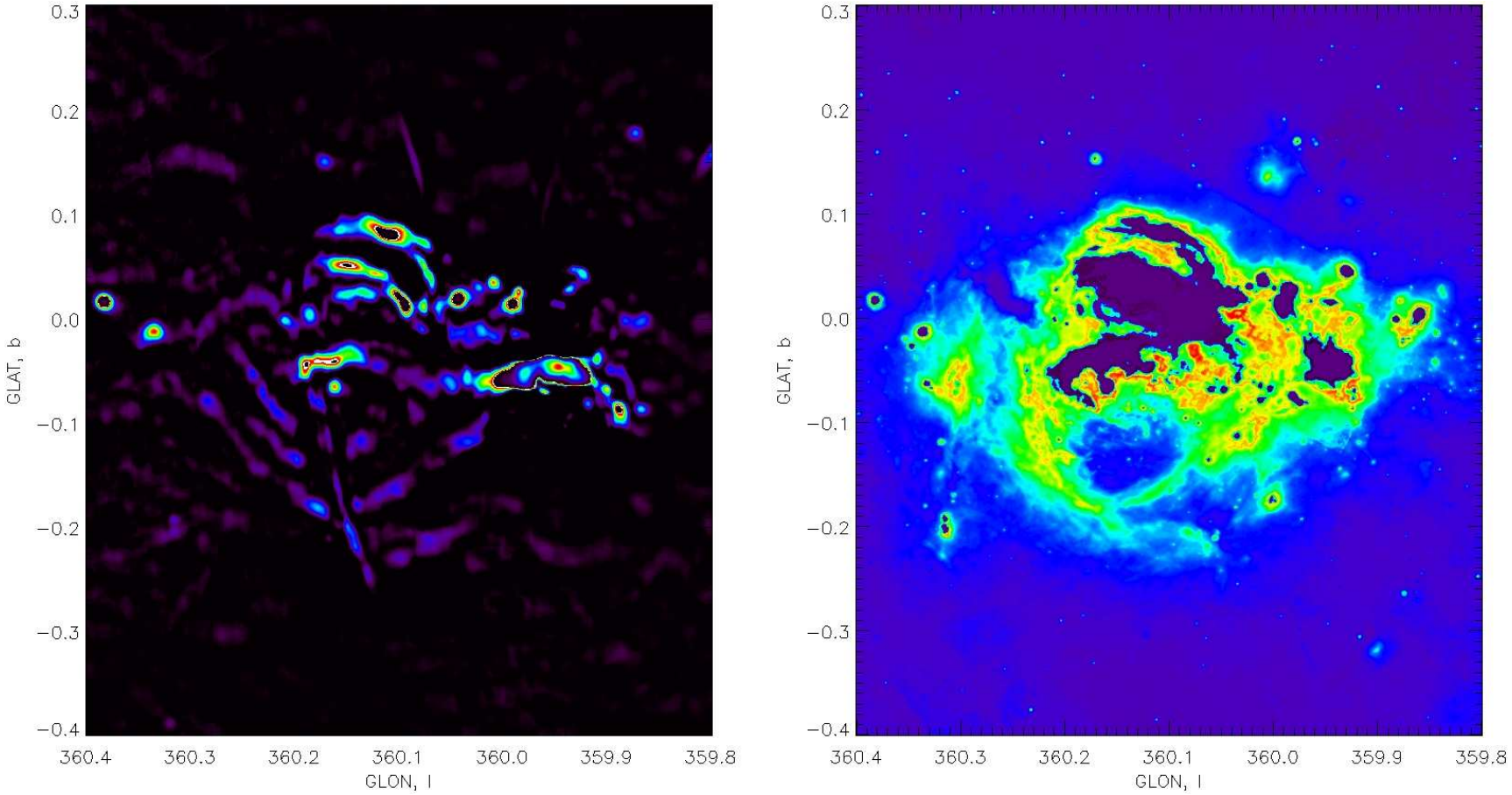

Figure 5.18: The re-filtered 20cm VLA map (left) that has been RFT along the length of the 'vertical' filaments is presented. The GCA region as observed with Spitzer/MIPS 24μm (right) is shown for comparison.

very closely coinciding with the N2 filament. The N2 filament has a position angle of 14° (E of N) and the line of 4 IR point source have a position angle of 18° (E of N). The line of the filament and the line of IR point sources are displaced by only 23" which is less than the resolution of the VLA map. These may be the seed sources for the accelerated non-thermal particle distribution in the NRF itself as described in the above *magnetic wake from an HII region* model (see sec. 5.1.4).

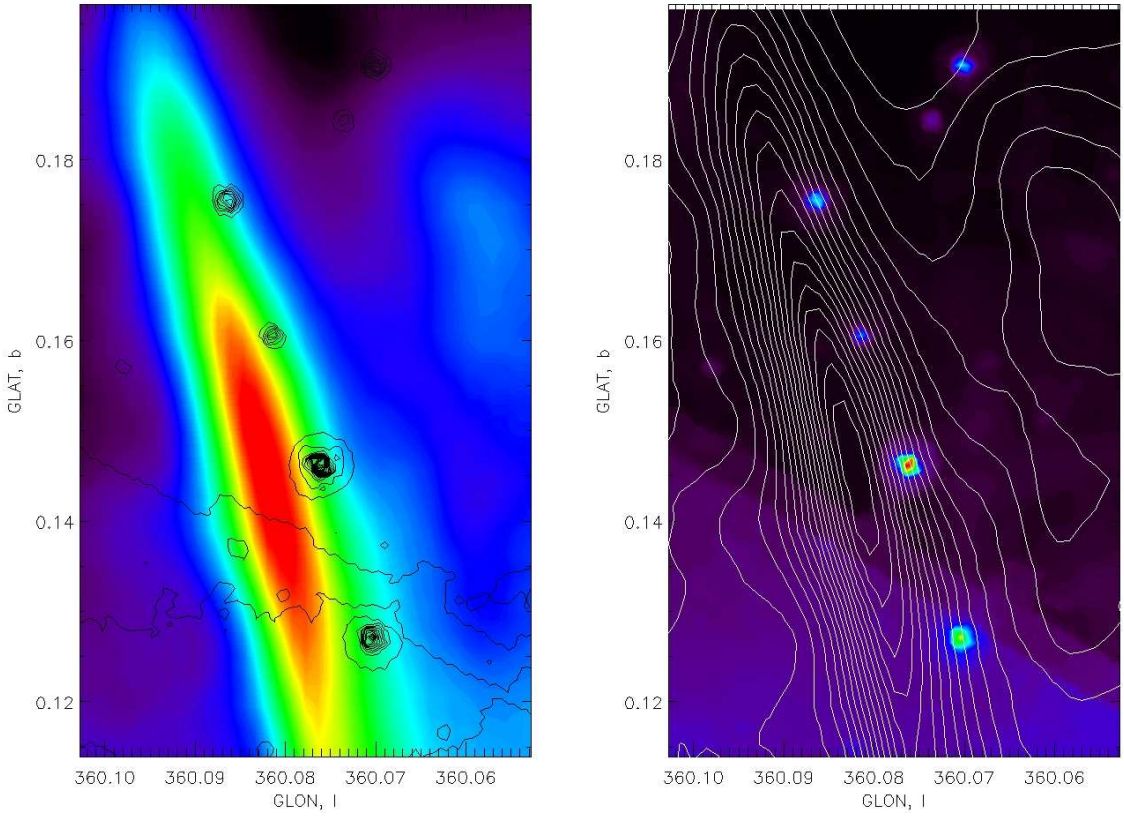

Figure 5.19: A close-up of the N2 NRF from the 20cm VLA compared to the same region from the Spitzer/MIPS 24μm image. (left) The VLA map in color and the IR map in contours. (right) The IR map in color and the VLA map in contours. The coincident string of IR point sources is the focus of this plot.

5.3 GBT vs. X-ray

Comparing the X-ray emission with the radio emission, it is interesting to see what the tracer for very high temperature gas shows. Though the Wang survey does not go beyond 0.4° above the galactic plane, there is a suggestive symmetry to the X-ray emission. There are two northward projections of X-ray emission symmetric about the Sgr A complex (see Fig. 5.20). The east projection is farther east than the GCL-E, and the west projection is also farther east than the

GCL-W. There is no direct correlation in diffuse emission to this X-ray feature in any of the radio maps, nor the mid-IR maps. Of course, the Wang survey does not extend far enough north to determine more of this interesting structure.

Within the GCA, however, this is an interesting anti-correlation between the radio emission and the X-ray emission (Fig. 5.21). Between the Sgr A complex and the 'vertical' filaments of the GCA there is a bright, diffuse ensemble of X-ray emission. This emission is also bordered to the north by the 'arched' filaments. It is likely this is a region of very high-temperature plasma.

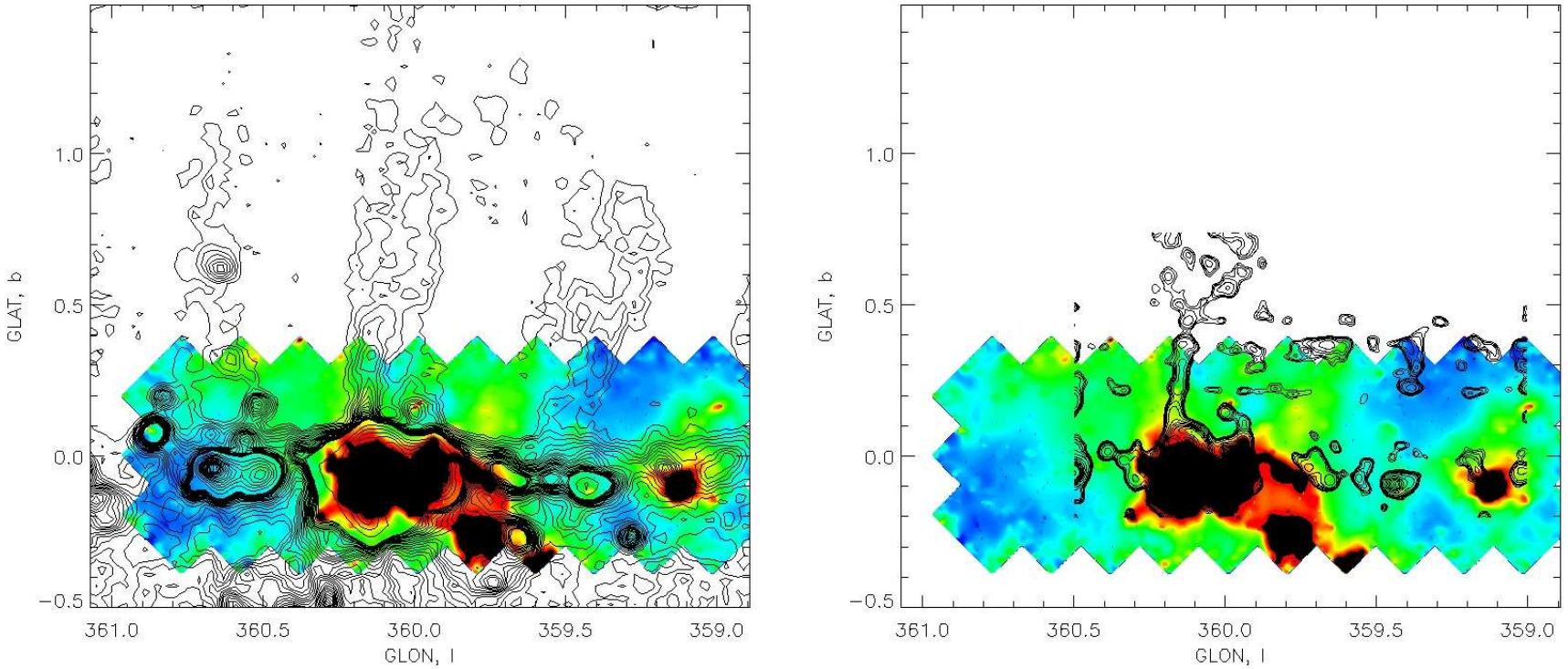

Figure 5.20: Complete Chandra ch1 (1-3 keV band) image, with the RFT to mostly remove point source and to emphasize diffuse structure (filtering window was 3 pixels = 17") is plotted with the filtered Sofue map contours overlaid (left) and our 14GHz GBT map contours overlaid (right). Filtered Sofue contours are the same as Fig. 5.4 and the GBT contours are the same as Fig. 5.1.

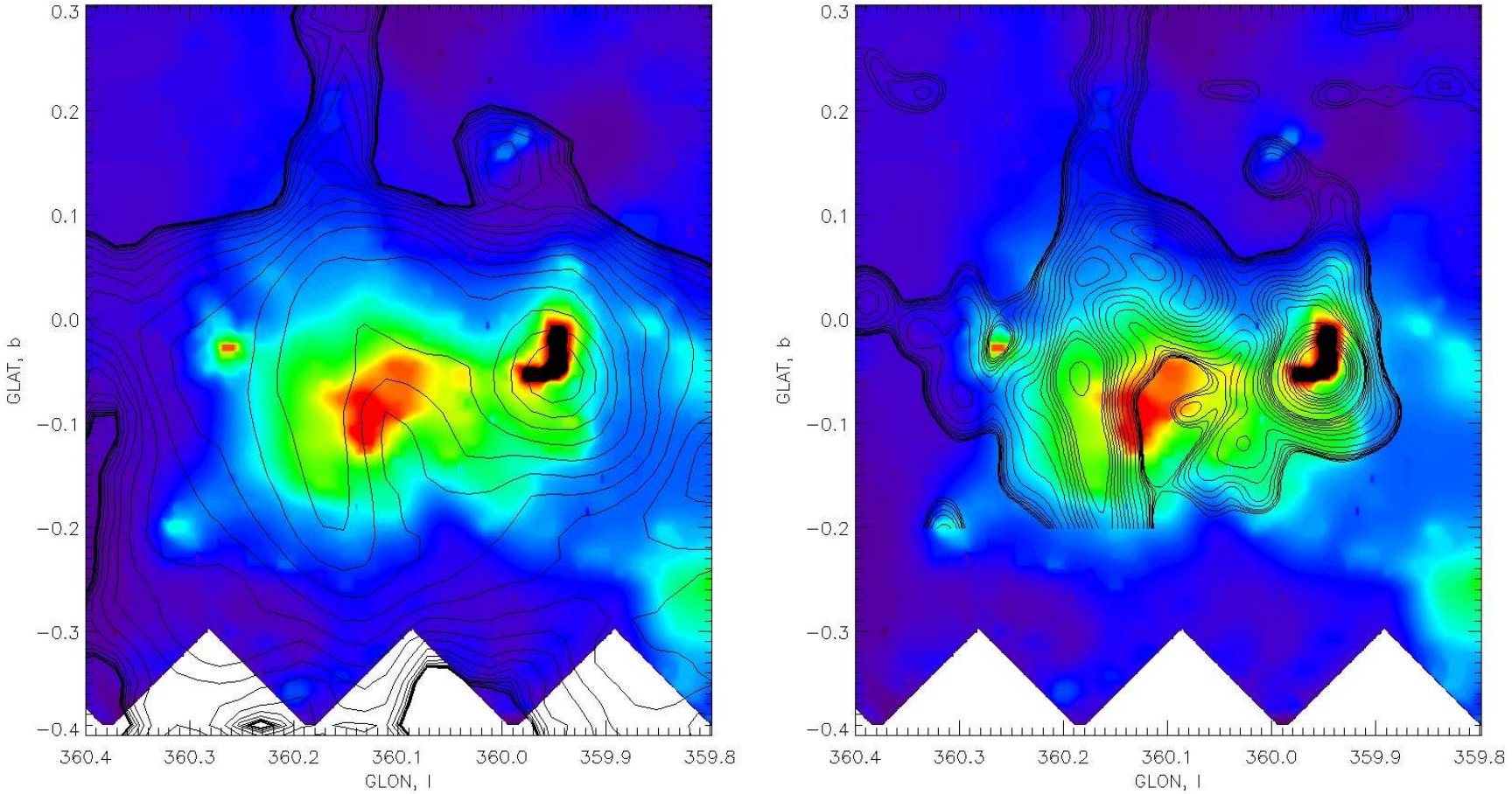

Figure 5.21: Chandra ch1 (1-3 keV band) image of the Galactic Center Arc (GCA) region, with the RFT to mostly remove point source and to emphasize diffuse structure (filtering window was 3 pixels = 17") is plotted with the filtered Sofue map contours overlaid (left) and our 14GHz GBT map contours overlaid (right). Filtered Sofue contours are the same as Fig. 5.4 and the GBT contours are the same as Fig. 5.1.

Chapter 6

Analysis and Theory

6.1 Consideration of the GCL origin model

6.1.1 Asymmetric Kompaneets Blastwave Toy-Model

Schiano (1985) describes and simulates a unifying model for the origin of superbubbles as formed by supersonic nuclear winds using a modified Kompaneets blast-wave solution. Shiano (1985) models a modified Kompaneets solution using as the source a wind instead of a point explosion in an exponentially decreasing atmosphere. This is a good simulation of the conditions at the galactic center, where the density presumably decreases exponentially with increasing galactic latitude. In general the form of the Kompaneets solution is sensitive to the ambient pre-shock density.

The GCL is not symmetric about the galactic center. The West wall is about three times farther from the center than the East wall. Additionally, the total flux from the East wall is about twice the magnitude as the total flux from the West wall: the approximate half-width of the West wall is twice the half-width of the East wall. These asymmetries can be used to test the behavior a Kompaneets-like blast wave, passing through pre-shock densities that are different would result in this asymmetry.

To first investigate the kind of matter distribution that could be responsible for the observed emission, we model a cylindrical elliptical shell with emissivity proportional to density (since the emissivity scales as the magnetic field, presumably frozen into the plasma, its strength is proportional to the plasma density). The cylindrical, elliptical shell is then modeled to be centered (at one of the ellipse's foci) on the Galactic Center (see Fig. 6.1), and the integrated brightness profile is calculated. Integrated brightness profiles of the 14GHz GBT data are also made; each

scan in Galactic Longitude are summed (for data with both 'walls' of the GCL available below b=0.5) (Fig. 6.2). With the only physical assumption pertaining to its emissivity, the elliptical shell brightness profiles qualitatively match the desired asymmetries observed in the GCL. The emission observed with the GBT of the GCL is consistent with emission from a cylindrical, elliptical shell.

To simulate the blast wave that would result in this kind of density contrast we have constructed a toy model of an asymmetric initial density distribution. The model is evaluated for a Kompaneets blast wave which shows, at least in principle, that a density contrast of 3 between the East and West sides of the Galactic Center region could be responsible for the asymmetry observed in the walls of a wind-blown shell. The equation for the Kompaneets blast wave is:

$$r = 2 \cdot a \cdot acos\ \frac{e^{\frac{z}{2a}}}{2} \cdot \left(1 - \frac{y^2}{4 \cdot a^2} + e^{\frac{-z}{a}}\right) \qquad \text{(Kompaneets, 1960)} \tag{6.1}$$

where a is the scale height of the vertical exponential density distribution, z is the vertical height, r is the transverse distance from the blast center, and y is related to the time coordinate by the following relation:

$$y \sim \frac{t}{\sqrt{\rho_0}} \tag{6.2}$$

where ρ_0 is the density of the material at the origin of the blast wave.

In the toy model, the 14GHz GBT image is displayed, and equal time steps of the Kompaneets blast wave are overdrawn on the image (Fig. 6.3). The East (left) side of the toy model use a ρ_0 of 1, and the West (right) side uses a ρ_0 of $\frac{1}{3}$. We simulate the GCL as an asymmetric blast wave in an exponential vertical density distribution, with one side 1/3 as dense as the other side. The blast fronts line up well with the spurs of the GCL. Note, however, that this model is meant to test *only* the east/west matter density asymmetry, *not* matter density *above* the galactic plane. That the curvature of, esp., the East spur does not match the curvature of the model shock front is not an issue; we are just investigating the propagation of the shock-front through the lateral asymmetric density distribution.

This density distribution, that the East side is 3 times as dense as the west side of the Galactic Center region is inconsistent with observations of the Expanding Molecular Ring (EMR) (Uchida et al, 1990, 1994)). The EMR is inclined to the plane of the galaxy by about 10 degrees, and is NOT centered on the GC. The EMR is off center towards the East of the GC, so the denser region of the EMR would be closer to the West side of the GCL. Thus, based on the observations of the EMR, it is unlikely that the West side of the GCL would be three time LESS dense than

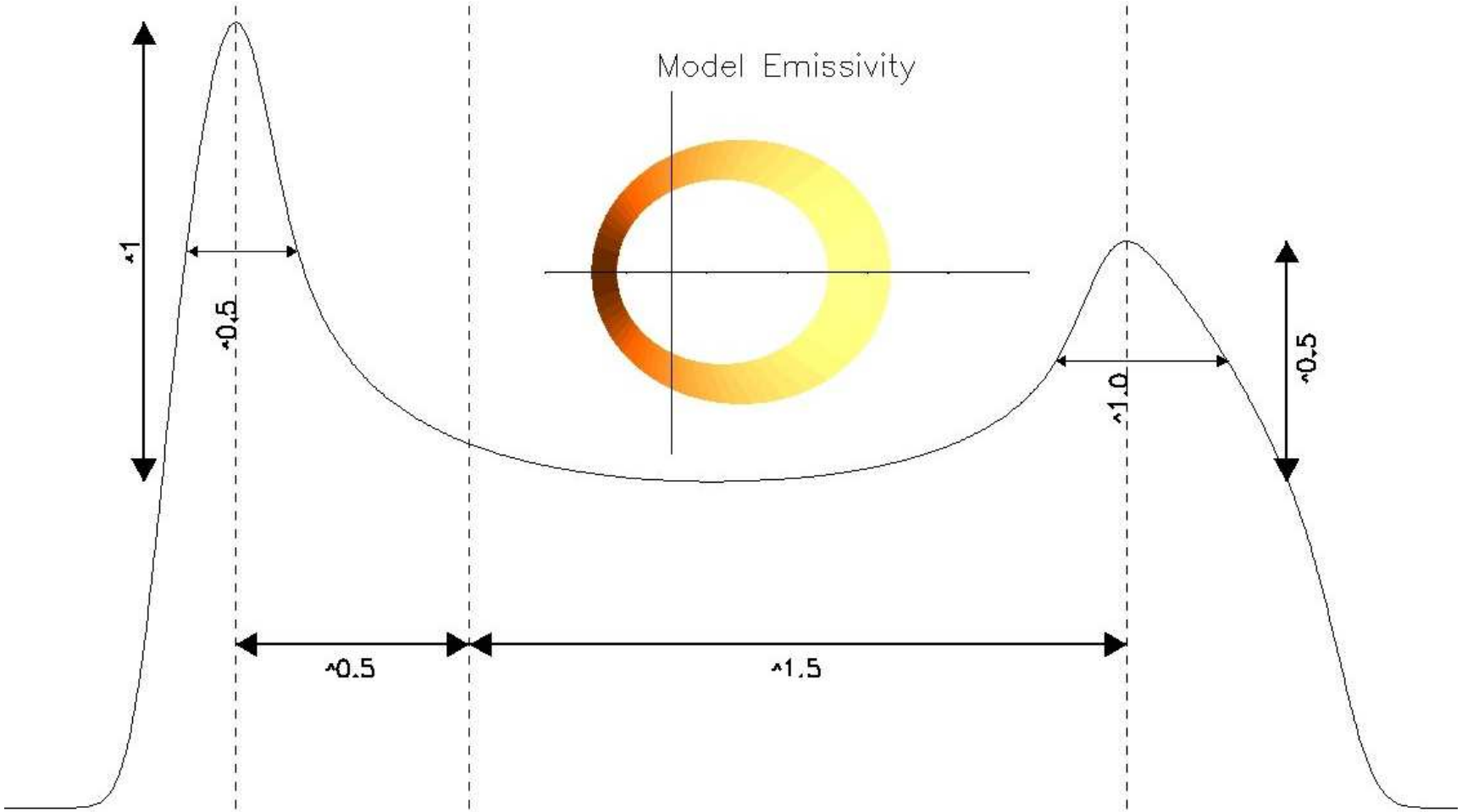

Figure 6.1: Model Emissivity of the elliptical cylindrical shell (pictured inset). The color is proportional to the emissivity (the thinner parts of the shell are actually more dense), and the model is integrated along the line-of-sight.

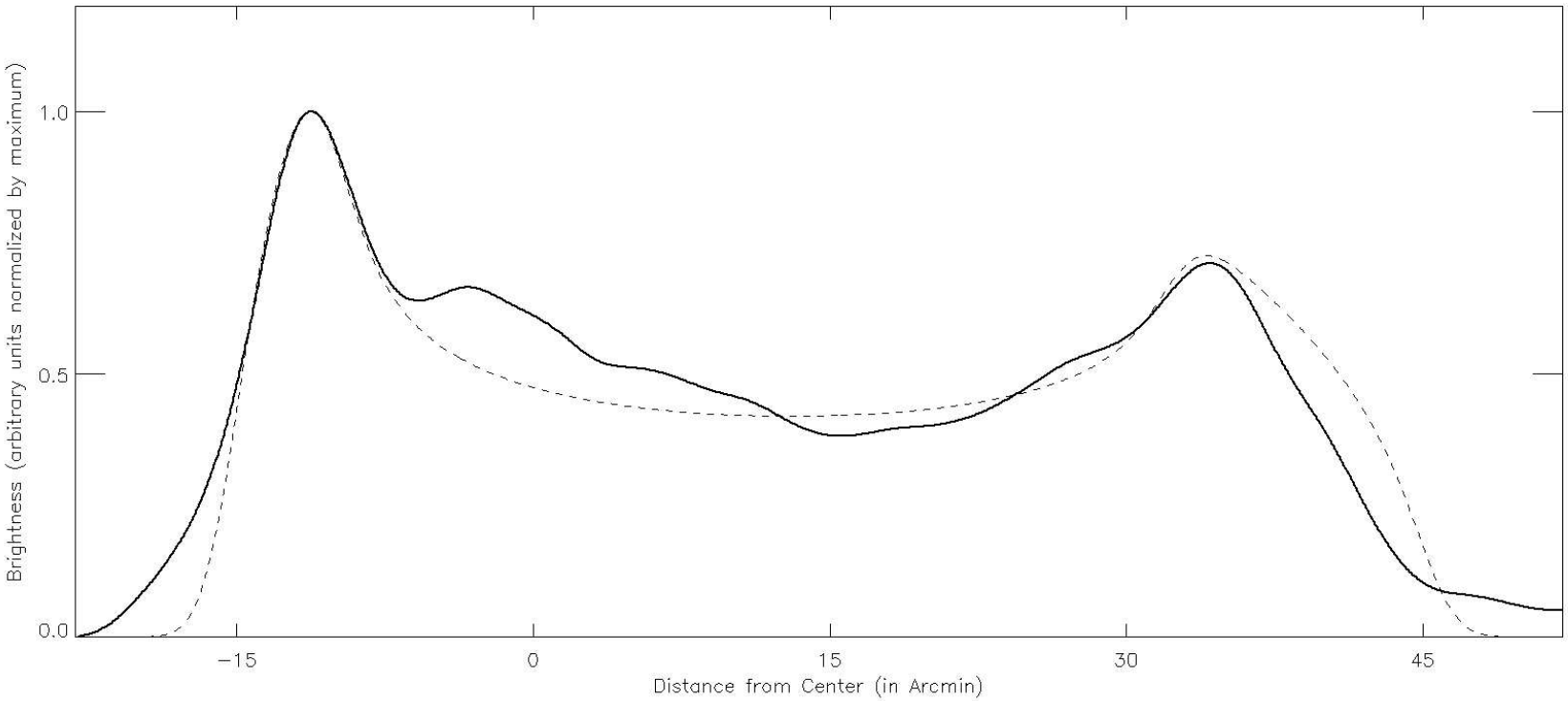

Figure 6.2: The Model Emissivity (dotted) of the elliptical cylindrical shell, and the Integrated Brightness Profile of the GCL-E and GCL-W, 14GHz GBT data. The profile and the model have been smoothed to 3'.

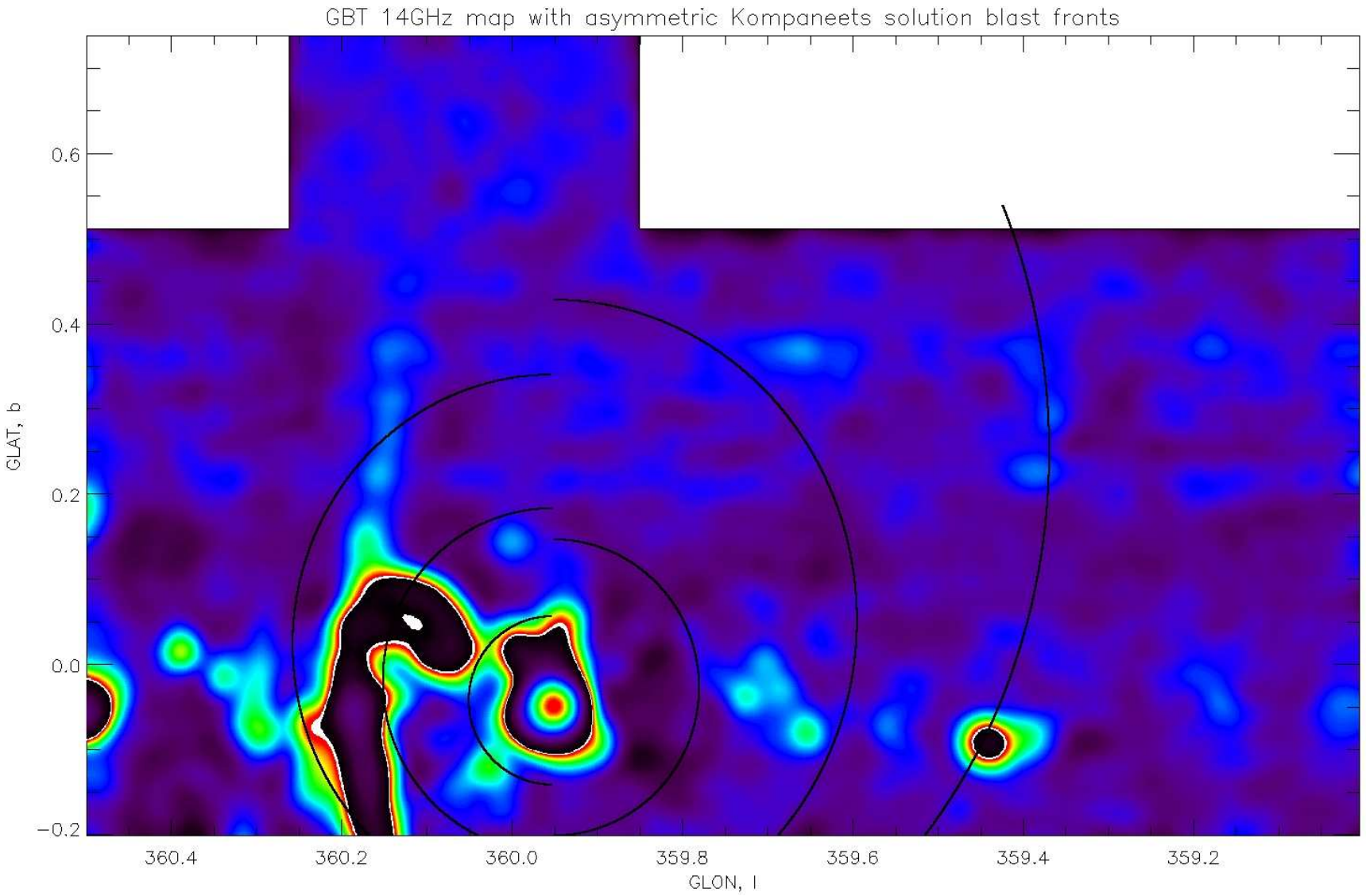

Figure 6.3: 14GHz GBT image with the equal time steps of the Kompaneets asymmetric lateral density distribution model superimposed.

the east side of the GCL. Additionally, the EMR is inclined about 75 degrees down. And thus, the density below the plane of the galaxy would be less than the density above the plane. This would mean that we would more likely see a bubble forming in the less dense region south of the galactic plane than the denser region north of the galactic plane, and yet we *do* see the GCL north of the galactic plane. There does not appear, in any waveband, a southern counter-part to the GCL, at least not as a coherent bubble. There is a southern extension of the Galactic Center Arc (see below/above) and there is some thought that the Sgr C complex south of the galactic plane is related to the West spur of the GCL (Sofue, 1985).

There are also arguments to explain the asymmetry observed between the two spurs of the GCL. The gas disc which powers the central engine need not be symmetric. So, if there is an asymmetry with the inflow source (the gas disc) and the outflows are related to the B-fields associated with the inflow source, then the outflow from the power source may be asymmetric as well, because the collimation of the B-field is associated with the infall material.

The evidence is very convincing, however, that the GCL-W is indeed a contact discontinuity and shock front. That there is a velocity discontinuity (see (Uchida *et al*, 1990), their Fig. 3) at the edges connecting (in projection) AFGL5376 observed at 24um and the GCL-W observed in our GBT map suggests that there is shock front at their interface. Uchida et al (1990, 1994) contend that the gas from the EMR is impacting an obstruction and being deflected out of the plane of the Galaxy. This deflection of gas is manifested as the GCL-W. The hot, shocked gas would push the cooler, denser dust out, away from the origin of the flow. Thus, as the radio-emitting plasma sweeps up the IR emitting dust, there would be a discontinuity between the radio and IR maps. This is precisely what is seen in our new image of the GCL-W. The filamentation in the IR suggests that there are several layers or fronts to the shock.

I argue that in order to have a nuclear wind Kompaneets-like blast wave as the origin to the GCL (being a wind-blown limb-brightened cylindrical bubble), then the density contrast between East and West of the galactic center must be on order 3. That this is inconsistent with the nature and orientation of the Expanding Molecular Ring implies that the blast-wave origin of the GCL is not a sufficient model. An explanation for the density configuration that is also consistent with the EMR would be in order, or else one or both of the spurs must be abandoned as wind-blown limb-brightened shells.

It is more likely, then, that the spurs of the GCL are not a connected, single structure, but two different structures, perhaps sharing origin mechanism, but not causally related. Indeed, the

preponderance of evidence of the differences between the GCL-E and the GCL-W suggest that even their origin mechanisms may be different.

6.1.2 The SgrB-Complex Spur

In searching for a new understanding of the GCL, we look again at the filtered Sofue map (see Fig. 6.4). The radio extension above the SgrB-complex looks promising in light of the dissimilarities between the GCL-E and the GCL-W. If the SgrB-complex extension is indeed similar to the GCL-W, a limb-brightened shell wall, then the integrated profile plots should be similar. We have summed the slices of constant galactic latitude from b=0.29 to b=1.29, excising a set of slices that correspond to the thermal point source located at (l,b)=(350.65,0.63). For comparison, and to note the effect of the RFT, we also plot the integrated flux profile for the same region in the unfiltered map (Fig. 6.5). The SgrB-complex spur and the GCL-W have about the same integrated flux density peak above the background of 0.34 $Jy \cdot arcmin^{-2}$ and 0.33 $Jy \cdot arcmin^{-2}$. This corresponds respectively to about 4.5σ and 4.9σ above the background, which was determined to be 0.235 $Jy \cdot arcmin^{-2}$, and the σ_{rms} is 0.060 $Jy \cdot arcmin^{-2}$. The above-background integrated flux height of the GCL-E is 0.60 $Jy \cdot arcmin^{-2}$, a 7.5σ detection above background. The half-widths of the SgrB-complex spur and GCL-W are 0.17 degrees and 0.20 degrees, respectively. The half-width of the GCL-E is much wider here because of the bend in the GCL-E where it is interacting with the DHN, but its half-width is about 0.17 degrees. The SgrB-complex spur is approximately located 0.7 degrees east of Sgr A*, and the GCL-W is 0.59 degrees west of SgrA*, while the GCL-E is 0.16 degrees east of SgrA*. Since the diffuse background structure between the east and west spurs of the GCL enhance the emission relative the background emission around the Sgr B-complex spur, it is difficult to compare the detection criteria for the Sgr B-complex spur to the GCL spurs. Especially note the contrast between the background on either side of the GCL spurs, comparred to on either side of the Sgr B-complex spur.

We now examine the spectral characteristics of the SgrB-complex spur. The 90cm VLA maps from the LaRosa survey acquired via the VLA archive are useful for flux comparisons. Because they are not combined with single dish data, they still have a lack of sensitivity to large scale diffuse structure, like all interferometric data. The largest angular size to which they are sensitive is 45'. In order to construct a proper spectral index map with Sofue's 10.5GHz single-dish data, the Sofue map must be filtered to remove all structures larger than 45', comparable to the VLA. To this end I have used Rudnick's filter to remove the 45' scale diffuse structure. I have then

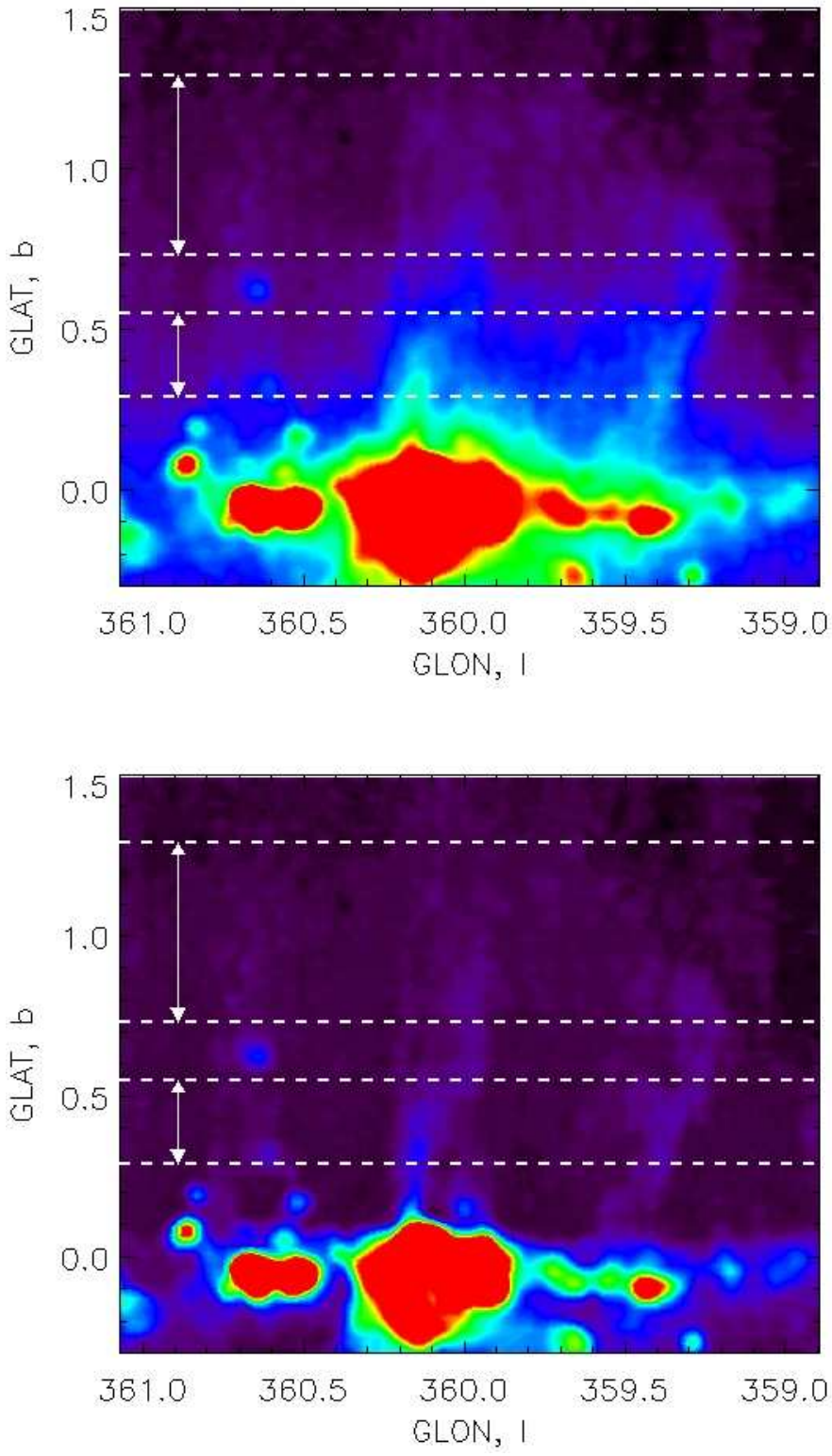

Figure 6.4: The regions of the integrated profile plots are displayed, note that the latitudes that contain the thermal point source in the Sgr B-complex spur have been omitted from the integrated profile plot.

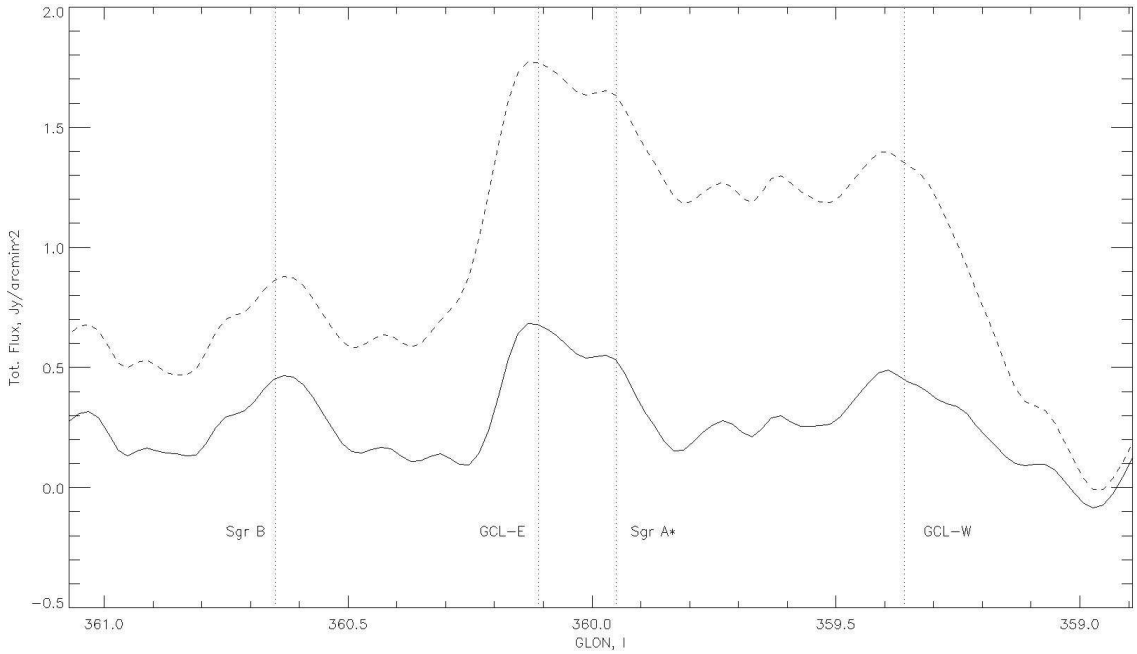

Figure 6.5: Both the unfiltered (dashed) and filtered (bold) Sofue maps' integrated profile plots are shown. The slices have been integrated over the regions shown in Fig. 6.4. The x-axis is Galactic Longitude, and vertical line, show the location of the SgrB, GCL-E, GCA and GCL-W regions.

rescaled each image to match pixel size (of 0.01 degrees per pixel), I then convolved each map to a beam size slightly higher than the Sofue map's beam size. The convolved beam size is 3arcmin. At this point the 90cm VLA image and the 10.5GHz Sofue image have the same beam size, pixel scale, and comparable sensitivity to large-scale diffuse structure, and spectral index maps can be made on a pixel-by-pixel basis.

By using the RFT, those regions of diffuse emission will, in the filtered map, be regions of exactly zero emission. The spectral index, by definition, cannot be calculated in these regions, and is removed (set to 0) at these points in the spectral index map.

The spectral index map (Fig. 6.6) is dominated by thermal ($\alpha < 0$) regions. Looking at the SgrB northern spur there is comparable emission in each map at the base of the spur, and farther up in the plume. At the base of the SgrB spur the spectral index ($S \sim \nu^{-\alpha}$) α is between -0.3 and -0.4 indicating a shallow (thermal) spectrum. This is consistent with the thermal nature of the GCL-W spur, whereas the central GCL-E spur is non-thermal in character (Figs. 6.7 and 6.8 respectively). .

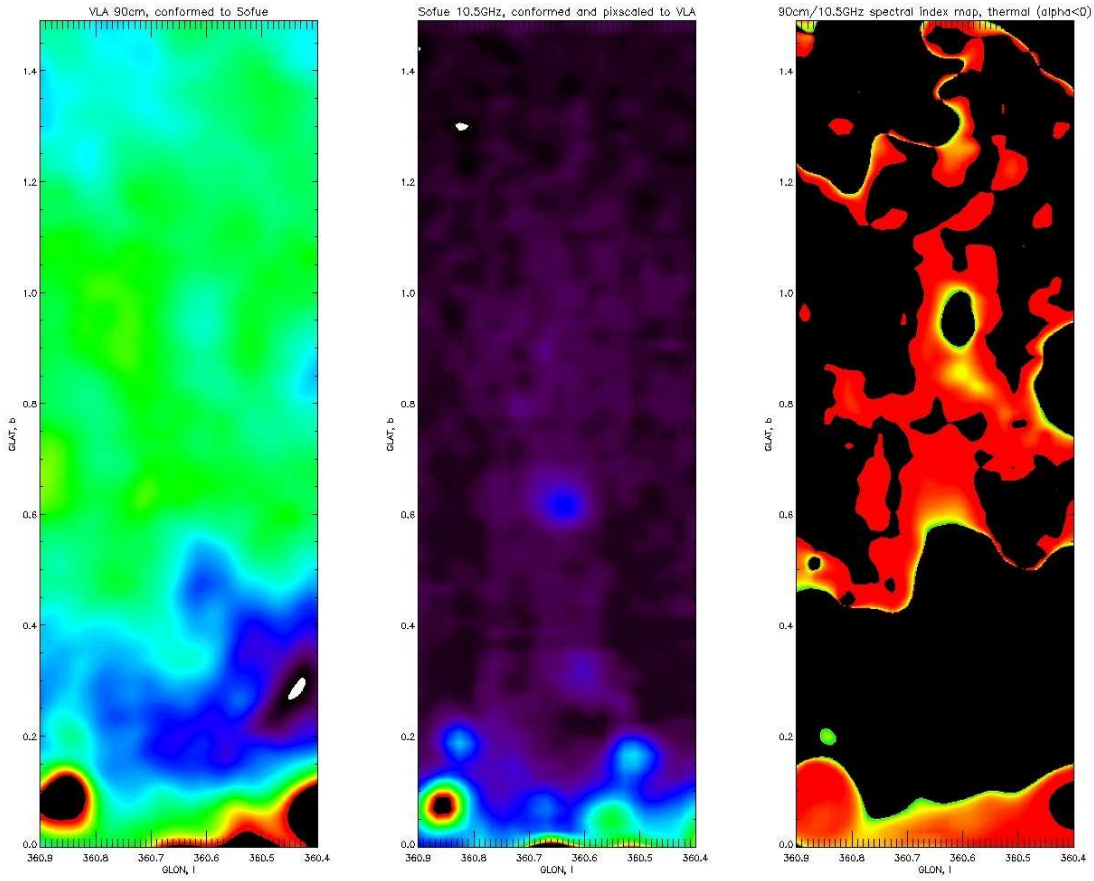

Figure 6.6: The RFT filtered and matched 90cm VLA image in the SgrB region (left), the RFT filtered Sofue map (center) and the negative ($\alpha < 0$) part of the spectral index map map from the two filtered images (right) are shown. The black regions in the (right) image are regions with ($\alpha > 0$) spectral index. All color regions have a negative (thermal) spectral index in the range of -0.5 to 0 spectral index.

6.1.3 A new Model

Given the density requirements to form a bubble whose walls are the GCL-E and the GCL-W it is reasonable to abandon this model of a coherent, causally connected structure, the GCL. The evidence that the spur over the SgrB-complex is the limb-brightened shell counterpart to the GCL-W is not overwhelming, but it need not be. Indeed, the density arguments for the formation of a wind-blown bubble need not produce a substantial limb on both sides of the galactic center. It seems likely that the Eastern side of the galactic center is substantially less dense, thus not lending itself to as magnificent a spectacle as the GCL-W. The fact remains, though, the SgrB-complex spur is a much better counterpart candidate on symmetry and matter density arguments alone. Therefore a new model for manifestation of galactic outflow (the true-GCL) would be a wind-blown limb-brightened superbubble whose edges are the GCL-W, and perhaps the SgrB-complex

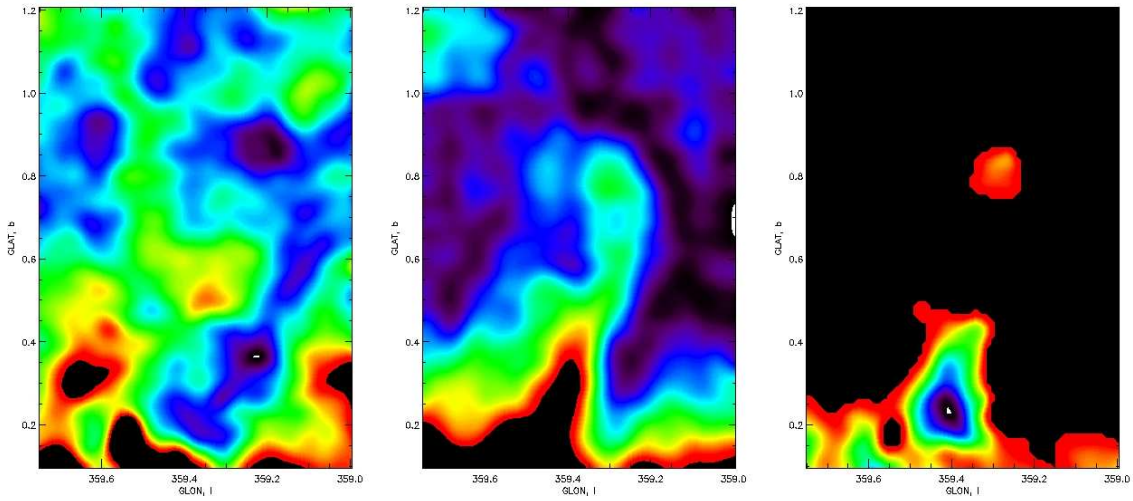

Figure 6.7: The RFT filtered and matched 90cm VLA image in the GCL-W region (left), the RFT filtered Sofue map (center) and the negative ($\alpha < 0$) part of the spectral index map map from the two filtered images (right) are shown. The black regions in the (right) image are regions with ($\alpha > 0$) spectral index. All color regions have a negative (thermal) spectral index in the range of -0.4 to 0 spectral index.

spur. What, then, is the nature of the GCL-E?

6.2 The Nature of the GCL-E

6.2.1 The interaction between the GCL-E and the DHN

There is strong supporting evidence that there is an interaction between the GCL and the DHN. There is a bow-shock-like arching structure clutching the seed of the DHN. The seed is a cool, dense gas cloud consistent with emitting thermal emission as it has a near flat spectral index. This is consistent with the simulations of Schiano, Christiansen & Knerr (1995) [hereafter SCK] simulations of the acceleration of ram pressure confined cool, dense clouds embedded in a hot, low density, supersonic wind. In the simulations, clouds are accelerated to well beyond their internal sound speeds, and are kept from being destroyed by ablation of cloudlettes of matter formed from hydrodynamic instabilities. The ablation of the cloudlettes actually stabilizes the cloud from destruction.

6.2.2 The wind/cloud simulations of SCK

The simulations in SCK are important enough that they warrant summary. The work is about the acceleration of ram pressure confined cool, dense clouds embedded in a hot, low density, supersonic

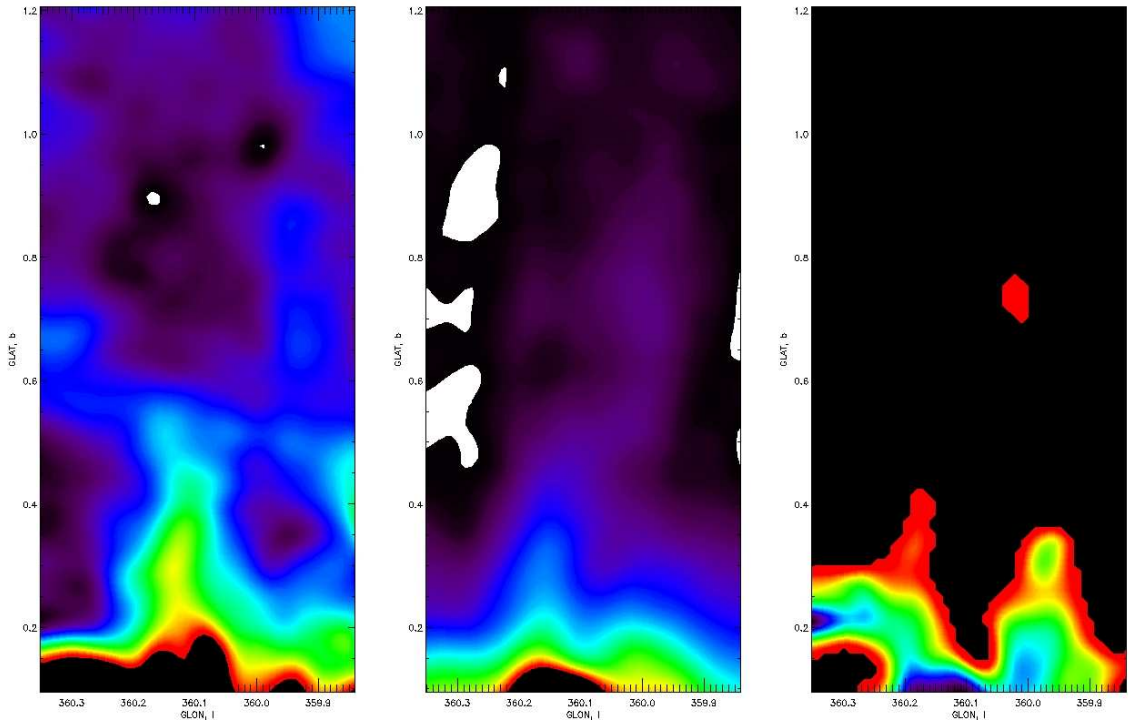

Figure 6.8: The RFT filtered and matched 90cm VLA image in the GCL-E region (left), the RFT filtered Sofue map (center) and the negative ($\alpha < 0$) part of the spectral index map map from the two filtered images (right) are shown. The black regions in the (right) image are regions with ($\alpha > 0$) spectral index. All color regions have a negative (thermal) spectral index in the range of -0.3 to 0 spectral index.

wind. Because of hydrodynamic instabilities this makes analyzing the interaction analytically very difficult. The instabilities are non-linear, so they must be numerically modeled. The main question of the work is: can winds accelerate clouds to about the wind speed (magnitudes above the internal sound speed of the clouds) without being destroyed. The theoretical arguments against and for this assertion come primarily from Allen (1984) and Christiansen et al (1977), respectively. Allen (1984) asserts that the clouds would be destroyed by the instabilities before acceleration can occur. Christiansen et al (1977) asserts that ablation of material from the cloud, due to instabilities, actually stabilizes the cloud, allowing time to accelerate the bulk motion of the cloud. These arguments are based on the fact that a cloud interacting with a supersonic wind is different than one interacting with a strong shock. This is intrinsically a three-dimensional problem with tangential flow as opposed to the restricted one-dimensional problem of a planar shocked cloud accelerated by a low density one-dimensional wind.

A cloud is impacted by a supersonic wind. A bow shock forms from the front of interaction. This bow shock is peaked at the stagnation point along the front of the cloud, and matter streams

around the cloud forming it into a tear-drop shape. Because of the ram pressure acceleration of the cloud this set up is the same as having a gravitational field pointing from the cloud to the wind. This sets up a stratification in the wind, similar to an atmosphere. This is equivalent to having a hot, low-density fluid pushing on a cool, high-density fluid. These circumstances promote Rayleigh-Taylor (RT) as well as Kelvin-Helmholtz (KH) instabilities.

From Allen (1984)'s argument, the formation of the RT instabilities would out pace the acceleration of the bulk cloud, and thus the cloud would be destroyed before it was accelerated to a speed comparable to the wind speed. But Allen's argument, based on 1D analysis, allows no tangential flow parallel to the shock front. Things are different in 2 and 3 dimensions, because the RT instabilities can move along parallel to the shock front. RT instabilities would result in projections of cloud material into the wind that would get caught up in the wind. This is ablation. The cloudlettes formed from RT instabilities would then get sheared away from the front of the cloud and accelerated downstream, removing them from the cloud and smoothing its surface. The blobs ablated from the cloud (or 'ablata') would themselves be subject to RT instabilities, further dissipating the destructive effects of the wind giving the cloud time enough to accelerate to near the wind speed, several times the internal sound speed, and also stabilizing the cloud so it does not mix with the wind.

The parameters for the wind/cloud simulations were the following: The cloud density was $\rho_C \sim 10^5 cm^{-3}$, the temperature was $T \sim 10^4 K$, the radius of the cloud was R_c $10^{14} cm$, the wind speed was $v_c \sim 400 km \cdot s^{-1} \sim 0.001c$, and the density contrast between the cloud and the wind was on order ~ 200.

The results of the simulations (only high-resolution) are summarized: On the nose-side of the cloud, as the wind impacts the cloud and RT instabilities form, shoulders of material jut out from either side of the central stagnation point. Any protrusions that occur are quickly ablated or stripped from the body of the cloud and accelerated downstream. When this mass is shed, the cloud reforms its smooth, tear-drop shape. This process they refer to as 'fire-polishing'. This cycle continues, as cloudlettes form, are ablated, and accelerated away from the cloud. Meanwhile, the bulk motion of the cloud continues to be accelerated by the wind pressure. By the time the simulations end, the cloud is moving an order of magnitude greater than the internal sound speed of the cloud, and comparable to the wind speed. The ablation of cloudlettes formed by RT instabilities and are sheared off by the wind allow enough time for bulk acceleration of the cloud, thus stability in large-scale structure is obtained from instability in small-scale structure

(see Fig. 6.9 which is SCK's Fig. 9).

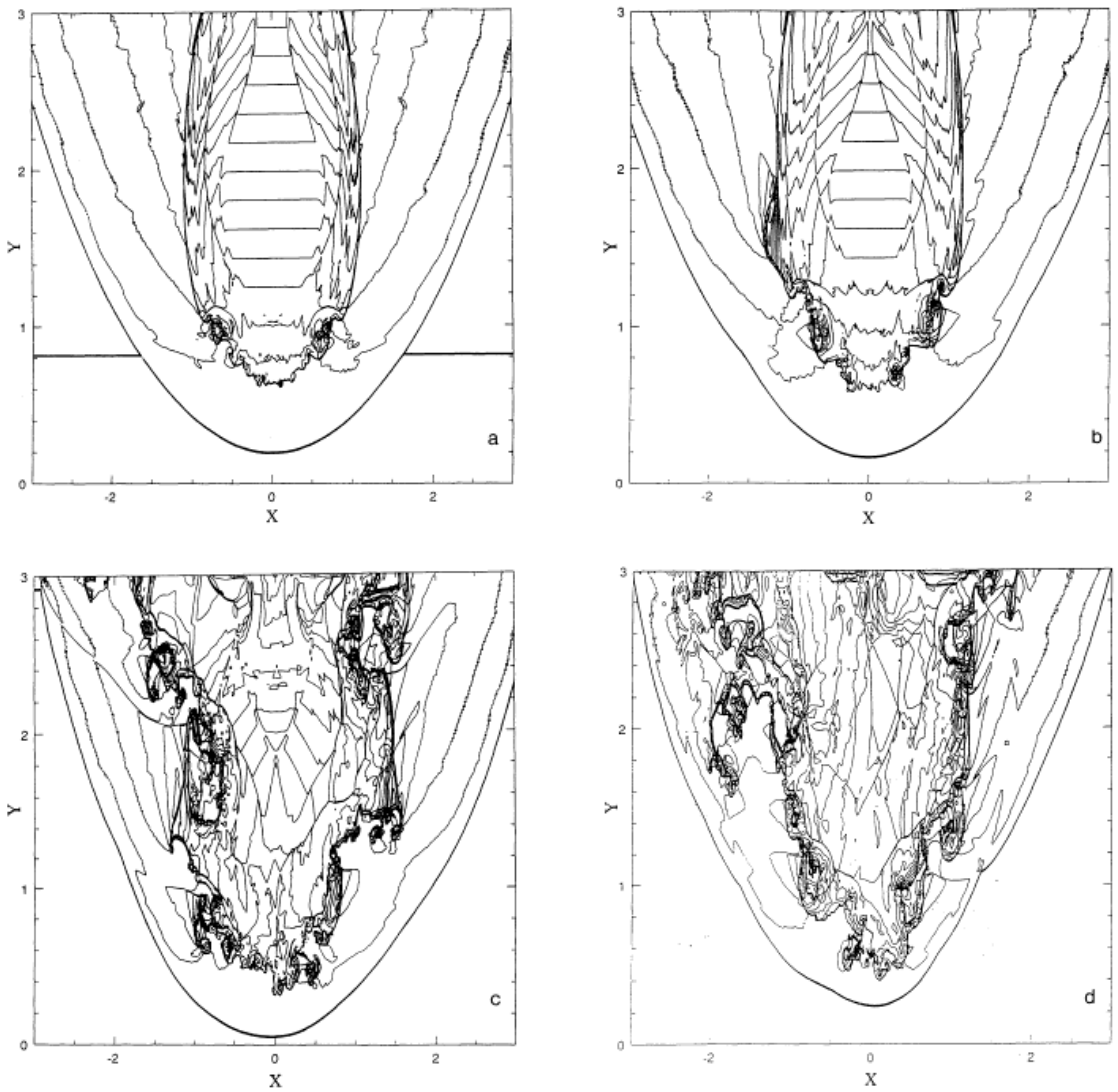

Figure 6.9: Fig. 9 from (Schiano, Christiansen & Knerr, 1995) showing the effect of a supersonic wind on a cool gas cloud. Contours levels indicate equal mass density. Time increases in (a)-(d) from 1.7 to 4.9 sound-crossing-times of the cloud.

It is argued that the simulation is robust for a wide range of extreme conditions. That in fact higher wind speeds and density contrasts enhance the stability of the ablation effect. In more extreme conditions, the formation of RT instabilities is balanced by the increased rate that 'ablata' are sheared and accelerated away from the cloud. So the two effects cancel. Also RT instabilities would not be able to penetrate as deep into the cloud, lowering the mass-loss, and increasing the stability of the cloud.

As the resolution of the simulations increases, the size of the 'ablata' decreases. SCK do a

fractal analysis of the simulations at different resolutions to determine if it displays fractal behavior. They examine contours of constant density to determine how their 'coastline' (i.e. perimeter) scales as a function of the enclosed area. From (Feder 1988) if the perimeter-to-area ratio ζ scales as: $\zeta = L^{1/D}/[A^{1/2}]$ with D being the 'fractal' dimension, then the model displays fractal behavior, characterized by a hierarchical distribution of scales, with smaller scales dominating over larger scales. SCK finds that, for the simulations, they exhibit a fractal dimension of $1.33 < D < 1.42$. This means that as the resolution increases the smaller scale instabilities dominate, increasing the overall stability of the bulk clouds.

6.2.3 Our data in light of the SCK simulations

We see in the Spitzer map the helical structure called the Double Helix Nebula. This is consistent with the SCK model of a cloud embedded in a wind having matter ablated off, trailing in a stream behind it, away from the wind. In the radio, a curved structure, that looks like a bow shock, is located at the head of the DHN. Indeed, the stream of the radio emission wraps around the head of the IR cloud. There seems to be mixing of the 'ablata' of the cloud with the wind/bow shock around the back of the infalling cloud. The bow shock would consist of the high-temperature wind, compressed as the bow shock forms. This compression of the wind plasma would compress the magnetic field, showing the bow-shock structure in high-energy synchrotron emission, observed in the radio. The radio bow-shock and the IR cloud would not be co-incident in space, which is consistent with what is observed, the bow shock and the seed cloud anti-correlate in the images.

The central seed of the DHN is a dust or gas cloud. It is not hot, or else it would not be visible as it is in the mid-IR. Morris et al (2006) strongly supports the thermal character of the seed, at least in IR. The DHN is not visible in any of the radio images. The strands of the DHN follow outside the radio, in fact in all radio images the wall of the GCL bends at the point that the seed of the DHN begins. The fact that there are two streamers would be understood as the contrails that are being ablated by the supersonic wind.

'Ablata' are indeed heated in the SCK simulations, but it is reasonable that they are not heated to well above their original temperatures, so there is not a substantial difference to the flux density in the strands compared to the seed cloud.

The simulations of SCK do not incorporate the magnetic field in the plasma and the wind. However, the hydrodynamics can easily accommodate a passive magnetic field (Christiansen, private communication). Provided our new model of the outflow bubble is correct, this or previous

epochs of outflow could systematically comb an incoherent B-field as it passes through, that is exactly what the plasma discontinuity does. So, it is not unexpected to find an ordered B-field outside the observed discontinuity if there have been several epochs of outflow.

We do not yet observe the DHN in the radio. Since the radio power scales as the square of the relativistic electron energy and the square of the B-field, this is not too surprising. If either or both of these factors have, for some reason, diminished significantly then there will be little to no synchrotron emission detectable. For example, it is possible that in the DHN the relativistic populations of electrons have suffered significant synchrotron losses. Also, because the ablating material from the DHN is embedded in the bow shock flow, the entrained B-field can reconnect and, therefore, will have large variations in intensity with the helical filaments representing enhanced B-fields and the gaps between filaments possibly representing the weak residual fields after reconnection. The B-field would thus be in the streamers, but the relativistic electrons in the GCL-E could not easily diffuse into this because the electrons would have to diffuse *across* field lines. As a result there could be a filamentary B-field in the DHN streamers causing the helical structure, but lacking the relativistic electrons necessary for synchrotron emission in the radio.

6.2.4 Properties of the DHN and assumed wind/jet parameters

The linear extent of the DHN is approximately 50 pc in projection. The seed cloud has a diameter of about 10 pc and the streamers are at most about 3.5 pc wide. The cloud is located about 100 pc from the galactic center. Morris *et al* (2006) estimate the temperature of the DHN to be between 300 - 700 K and particle density of $5cm^{-3}$. The internal sound speed of the DHN is therefore $2-3km\cdot s^{-1}$. We can assume the general properties of the wind as derived in Bland-Hawthorne & Cohen (2003), such that the wind velocity is between $1700-3000km\cdot s^{-1}$ and the particle density of the wind is $1cm^{-1}$.

6.2.5 Hydrodynamic Luminosity

We can estimate a lower limit for the outflow hydrodynamic luminosity from the energy flux impinging on the bow-shock at the seed cloud of the DHN. The energy deposited at the bow-shock is $P_{ram}\times A_c\times v_w$; where P_{ram} is the ram pressure of the wind ($P_{ram}=\rho_w\times v_w^2$), A_c is the cross-sectional surface area of the cloud, and v_w is the wind speed. Thus the energy deposition rate in the bow shock by the jet is: $L_{hydro}=\rho_w\times v_w^2\times A_c\times v_w$ and we obtain an energy deposition

rate of $4 \times 10^{40} ergs \cdot s^{-1}$. An upper limit can be estimated by simply assuming a spherical wind permeating the $R_{DHN} \sim 100pc$ volume outside the GC where the DHN is located. In that case $L_{hydro} = 4\pi R_{DHN}^2 \cdot \rho_w \cdot v_w^3 \sim 4 \times 10^{42} ergs \cdot s^{-1}$, which would be in the high range of a weak AGN. For comparison, the required black hole accretion rate, for the Galaxy's massive black hole, the lower limit would be $10^{-6} M_\odot \cdot yr^{-1}$ and the upper limit would be $10^{-4} M_\odot \cdot yr^{-1}$. Both of these values are greater than that inferred from the spectra of SgrA* (Melia & Falke, 2001), which is about $10^{-8} M_\odot \cdot yr^{-1}$. On the other hand, the SN rate which would be necessary in Galactic Center region would require a lower limit of 1 SN every 100 yrs, and an upper limit of 1 SN per year (assuming an average type II SN explosion with $E = 10^{50} ergs$). If we assume a dynamical timescale for the DHN of 30-60 kyrs (see sec. 6.2.8), this amounts to an energy deposit of $10^{52-54} ergs$ up to an three (3) orders of magnitude below the required energy to create the GCL as a single structure, $10^{55} ergs$ (Bland-Hawthorne & Cohen, 2003).

6.2.6 The Wind as a Cloud Filter

Following (Christiansen, 1969) we now examine the effect that the wind has on lofting the cloud through the Galaxy's gravitational field. If we assume that the acceleration of the cloud is due only to the ram pressure of the wind on the cross-sectional area of the cloud and the acceleration due to the Galaxy's gravitational field (i.e. we do not take into account orbital motion) we have:

$$\rho_w \cdot v_w^2 \cdot \pi \cdot r_c^2 - M_c \cdot g = M_c \cdot a \tag{6.3}$$

where ρ_w is the wind density, v_w is the wind speed, r_c is the cloud size, g is the acceleration from gravity and M_c is the mass of the cloud. The critical point between the cloud being ejected and falling into the disk is that a=0. Thus we have

$$\rho_w \cdot v_w^2 \cdot \pi \cdot r_c^2 = M_c \cdot g \tag{6.4}$$

The mass of the cloud, M_c is $\frac{4}{3}\pi r_c^3 \cdot \rho_c$, the critical size of the cloud is

$$r_\circ = \frac{3 \cdot \rho_w \cdot v_w^2}{4 \cdot \rho_c \cdot g} \tag{6.5}$$

and therefore: $r_c < r_\circ$ results in the cloud being ejected from the galaxy, whereas $r_c > r_\circ$ results in the cloud falling into the galaxy. Thus, the wind acts as a filter, such that small clouds are

ejected from the galaxy, and large clouds fall into the galaxy.

However, the cloud is having mass striped from it by ablation, so, even if the cloud is large enough to fall into the galaxy, the stripping of mass may reduce the size of the cloud sufficiently to have it again rise up and be ejected over time. From SCK's simulation, it is observed that the rate that mass is striped from the cloud is approximately constant. Thus the mass as a function of time is:

$$M(t) = M_\circ - \dot{m} \cdot t = \frac{4}{3}\pi \cdot r_c^3 \cdot \rho_c \tag{6.6}$$

where $\dot{m}$ is held constant. And solving for $\rho_c = \frac{M_\circ - \dot{m} \cdot t}{\frac{4}{3}\pi \cdot r_c^3}$. We plug this into the equation for the critical cloud size, $r_\circ$ and obtain a new relation for the critical size of the cloud, taking into account ablation:

$$r_\circ^2 = \frac{g \cdot (M_\circ - \dot{m} \cdot t)}{\pi \rho_w \cdot v_w^2} \tag{6.7}$$

and again, where the size of the cloud, $r_c^2 < r_\circ^2$ the cloud is ejected out of galaxy, and $r_c^2 > r_\circ^2$, the cloud falls into the galaxy.

The internal ambient matter has an approximate enclosed mass of the relation $3 \times 10^6 \cdot r_\star \cdot M_\odot$ where $r_\star$ is the radial distance from the GC, expressed in pc (Morris & Serabyn, 1996). Therefore the gravitational acceleration at the distance to the seed cloud of the DHN ($\sim 100pc$), is $g = \frac{G \cdot M_{enclosed}}{R^2} = 4 \times 10^{-9} m \cdot s^{-2}$. Thus the critical size of the cloud, to float in the wind, is $r_\circ = 1500pc$. This is quite a large cloud, given that the DHN is only about 10pc in extent. Thus, nearly any cloud in the galactic wind will be accelerated away from the disk. But at what rate?

6.2.7 The Cloud's Equation of Motion

We can treat an individual cloud accelerated and confined by ram pressure. The acceleration is, as before:

$$\rho_w \cdot (v_w - v_c)^2 \cdot \pi r_c^2 = M_c \cdot a_c \tag{6.8}$$

We can make a substitution for the relative velocity, such that, $u = v_w - v_c$ and therefore: $a_c = \frac{dv_c}{dt} = -\frac{du}{dt}$. As the cloud accelerates, the relative speed between the cloud and wind decreases, thus the ram pressure decreases, and the cloud expands, since it is ram pressure confined. We assume this is a self-similar expansion, thus the energy per unit mass (ε), scales with the radius, thus: $\varepsilon = \varepsilon_\circ \cdot \frac{r_\circ}{r_c}$. The subscript, '$\circ$', indicates the initial conditions (e.g. $r_\circ$ is the initial size of the cloud). The energy per unit mass can be written $\varepsilon = \frac{a_c \cdot r_c}{\pi}$ and we can substitute the initial energy density with the sound speed in the cloud squared ($\varepsilon_\circ = c_s^{\circ 2}$). We can now write the cloud

size: $r_c^2 = \frac{c_s^2 \cdot \pi r_\circ}{a_c}$ and plug this into the acceleration condition.

$$a_c^2 = \frac{\rho_w \cdot \pi^2 c_s^2 \cdot r_\circ \cdot u^2}{M_c} = (-\frac{du}{dt})^2 \tag{6.9}$$

and solving for $(\frac{du}{dt})$ we obtain:

$$\frac{du}{dt} = \pm\pi u \sqrt{\frac{\rho_w \cdot c_s^2 \cdot r_\circ}{M_c}} \tag{6.10}$$

which has the solution:

$$ln(u) = \pm\pi \sqrt{\frac{\rho_w \cdot c_s^2 \cdot r_\circ}{M_c}} \cdot t + (const) \tag{6.11}$$

for t=0, the relative velocity, u, is v_w, since the cloud has not yet been accelerated, and substituting $M_c = \frac{4}{3}\pi r_\circ^3 \cdot \rho_c$ and $T_l^{-1} = \frac{c_s^\circ}{r_\circ}\sqrt{\frac{\pi\rho_w}{\rho_c}}$ gives

$$u(t) = v_w \cdot e^{-\frac{t}{T_l}} = (v_w - v_c) \tag{6.12}$$

and thus,

$$v_c(t) = v_w \cdot (1 - e^{-\frac{t}{T_l}}) \tag{6.13}$$

Integrating again to obtain the distance traveled by the cloud, l_c, in a time t and putting back in our substitutions, we obtain:

$$l_c(t) = (\frac{\rho_c}{\rho_w})^{\frac{1}{2}} \cdot (c_s^\circ \cdot t - r_\circ \cdot (\frac{\rho_c}{\rho_w})^{\frac{1}{2}} \cdot \frac{1}{\sqrt{\pi}} \cdot (1 - e^{-\frac{c^\circ}{r_\circ}\cdot\sqrt{\frac{\pi\rho_w}{\rho_c}}\cdot t})) \tag{6.14}$$

and using the parameters for the cloud, and wind we obtain:

$$l_c(t) = 6.6 \cdot t_{Myr} - 28 \cdot (1 - e^{0.18 \cdot t_{Myr}}) \tag{6.15}$$

where t is in Myr and l is in pc. The timescale for the DHN to be lofted by about a cloud size (i.e. $\sim$10pc) is then about 0.3Myr, less than the orbital time of the DHN of $\sim$ 1Myr (see sec. 6.2.8). If we assume that the cloud is completely ejected at some arbitrary distance from the galactic plane, for instance 1 kpc, the ejection time is about 20 Myr.

6.2.8 Timescales

Since the SCK simulations indicate a fractal distribution (with a fractal diminsion of 1.4, see Knerr Thesis Fig. 4.10) in the size of ablated cloudlettes with small scale predominating, they find that

the stream of 'ablata' quickly accelerates up to the wind speed, v_w (see Knerr Thesis, Fig. 4.11). Thus, we can estimate the time required for 'ablata' to travel the length of the streamers of the DHN. Assuming a windspeed of $1500 - 3000km \cdot s^{-1}$ and an 'ablata' length of about 50pc, the travel time would be between $30 - 60kyr$.

At the location of the DHN, if it is assumed to be orbiting the galactic center, the circular orbit has a orbital speed of $110km \cdot s^{-1}$ which is much less than the wind speed. So, minimal curvature would be seen in the 'ablata' stream as is also evident from the fact that the 'ablata' travel time is much less than the orbital period of ~ 1 Myr.

6.2.9 The Bloby Nature of the GCL-E

Inspecting at the 90cm, 20cm, 10GHz, and 14GHz maps of GCL-E, the bloby nature of the GCL spur is evident. The bloby, knotted nature of the length of the GCL-E may be explained as accelerating or ejected packets of plasma along the length of a jet. Plasmons that are ejected/accelerated/etc. light up (in radio) because of hydrodynamic instabilities from being pushed/accelerated/etc. This transfers some of the bulk kinetic energy to in situ particle acceleration essentially lighting them up in non-thermal radio emission (Christiansen et al 1977)

6.2.10 The Galactic Center Arc (GCA)

The favored creation mechanism (Yusef-Zadeh et al, 1989) for the galactic center arc is the solar flare analogy. In solar flares on the Sun, bundles of magnetic field are ejected from the Sun, where the field lines cross they reconnect, expelling energy, and taking with it matter that is ejected. There is a magnetic field left over after the reconnection which is now organized. Similarly, it is thought in the Galactic Center Arc that the differential rotation of the galaxy or mere turbulence can cause twisting and ejection of magnetic field from the nucleus out to large scales (50pc like the GCA). Relaxing (reconnection) of magnetic fields results in particle acceleration and an ordering of the magnetic field, so there is an ordered magnetic structure that a non-thermal (synchrotron) emitter.

6.2.11 Evidence for past outflow in the GCA region

The correlation of radio and IR filaments in the selectively filtered VLA 20cm and the 24um Spitzer map (see Fig. 5.18) are evidence for shells from previous starburst events in or near the

'sickle' star forming region. The magnetic prominences of the vertical filaments would be the site of the matter that would be accelerated into a jet above and below the GCA

This may also result in a jet-like stream of particles above the GCA as they break out of the concentric shells accelerated along the coherent magnetic field in the GCA. The polarized lobes observed by Seiradakis et al (1985) above the GCA correspond to the GCL-E, indicating that the coherent magnetic fields continue into the GCL-E.

6.2.12 Summary

The build-up of high temperature X-ray emitting plasma at the center of a disk galaxy leads to an outflow, in general. The highly ordered magnetic fields in the Galactic Center Arc (GCA), nearly coincident with the X-ray emitting plasma contained within the GCA, give that plasma an avenue to escape the plane. The GCA collimates the streaming plasma, breaking through the previous shells of outflow as evidenced by the radial filaments. The collimated, bloby, jet-like extension GCL-E impacts a gas or dust cloud resulting in the transient phenomenon of the Double Helix Nebula (DHN).

Chapter 7

Summary and future work

7.1 Summary

The GCL has been mostly thought to be an outflow structure, both sides of which were formed from the same phenomenon, generally a supersonic (or stalled) nuclear wind. However, mounting evidence does not support this model, as each 'spur' of the GCL is unique in its morphology, spectral characteristics, and interactions with the ambient media. The GCL-E is likely a jet-like structure intimately connected with the Galactic Center Arc (GCA), and not a limb brightened wall of an expanding bubble. Whereas the previous interpretation of the GCL-W 'spur' is likely to be correct. However, the current hypothesis is that the counterpart wall to the GCL-W is the spur of emission above the SgrB-complex. Both the GCL-W and the SgrB projection are more symmetric around the Sgr A complex than the GCL-E, both in location (in projection) and power. There is suggestive evidence both in low-frequency radio maps (90cm) and Chandra X-ray images (although this last image is incomplete) to support this hypothesis. The nature of the GCL-E, on the other hand, is consistent with a jet formed from the northern extension of the Galactic Center Arc that is impacting the Double Helix Nebula, wrapping around it and being deflected past it.

7.2 Future Work

The obvious next observation is a more sensitive observation of the proposed SgrB projection to verify – in higher-resolution, higher-frequency maps (presumably with the GBT) – the hypothesis that it is a limb-brightened bubble wall. Additionally, the symmetric bubble pattern of low-latitude (galactic coordinates) X-ray emission suggests that the high-temperature plasma traces

out the inner edges of the SgrB/GCL-W superstructure, and so a higher latitude X-ray survey of the GC region would appropriate.

An investigation into the North/South asymmetry is in order. There is suggestive evidence that there are southern extensions of the bubble below Sgr C, and perhaps a southerly extension of the Galactic Center Arc as well (in our new model, presumably related to the GCL-E). A mapping survey of the southern region of the GC, including the Sgr B-complex, would illuminate these possibilities; again, the GBT would be well suited for these observations.

An unanswered question regarding the GCL-E/GCL-W association is the nature of the 'cap' at the apex of the GCL, apparently bridging the gap (perhaps only partially) between the two spurs. This is curious, given the new model. However, this may be part of the bridge (or cap) connecting the GCL-W/SgrB bubble walls, or some other interesting structure. To answer this question requires further investigation. With our unique techniques for mapping faint emission with the GBT this observation would be well suited for the GBT.

Another major focus for further observations is the interaction between the GCL-E and the DHN. This is a unique, nearby, laboratory for complex hydrodynamic interactions that heretofore have not been observed. X-rays may be emitted at the stand-off bow-shock of the interaction where the flow is interacting with the cool cloud. Chandra observations of the GCL-E/DHN area may elucidate the observed bow-shock-like structure.

References

Allen, A. J. 1984, MNRAS, 210, 147

Anantharamaiah, K. R., Pedlar, A., Ekers, R. D., & Goss, W. M. 1991, MNRAS, 249, 262

Bland-Hawthorn J., Cohen M., 2003, ApJ, 582, 246

Boldyrev, S., & Yusef-Zadeh, F. 2006, ApJ, 637, L101

Bosch-Ramon, V., Romero, G. E., Paredes, *et al.* 2006, A&A, 457,1011

Cecil, G., Bland-Hawthorn, J., & Veilleux, S. 2002, ApJ, 576, 745

Cecil, G., Bland-Hawthorn, J., Veilleux, S., & Filippenko, A. V. 2001, ApJ, 555, 338

Chevalier, R. A., & Clegg, A. W. 1985, Nature, 317, 44

Christiansen, W. 1969, MNRAS, 145, 327

Christiansen, W. A., Pacholczyk, A. G. 1977, Nature, 266, 593C

Encrenaz, P. J., Penzias, A. A., & Wilson, R. W. 1970, A&A, 9, 51

Feder, J. 1988, Fractals (New York: Plenum Press)

Knerr, J. M., PhD Thesis, The University of North Carolina at Chapel Hill, 1993

Kompaneets, A. S. 1960, Dokl. Akad. Nauk SSSR, 130, 1001 [Soviet Phys. Dokl., 5, 46]

LaRosa, T. N., Kassim, N. E., Lazio, T. J. W., & Hyman, S. D. 2000, AJ, 119, 207

Melia, F., & Falcke, H. 2001, ARA&A, 39, 309

Morris M, Uchida K and Tuan D 2006 Nature 440 308

Oort, J. H. 1977, ARA&A, 15, 295

Pacholczyk, A. G. 1970, Radio Astrophysics (San Francisco: Freeman)

Pedlar, A., Anantharamaiah, K. R., Ekers, R. D., Goss, W. M., van Gorkom, J. H., Schwarz, U. J., & Zhao, J-H. 1989, ApJ, 342, 769

Reich, W. 1982, A&AS, 48, 219

Reich, W., Sofue, Y., & Frst, E. 1987, PASJ, 39, 573

Rudnick, L.: 2002, PASP 114, 427

Schiano, A. V. R., Christiansen, W. A., & Knerr, J. M. 1995, ApJ, 439, 237 (SCK)

Schiano, A.V.R.: Astrophys. J. 299, 24 (1985)

Seiradakis, J. H., Lasenby, A. N., Yusef-Zadeh, F., Wielebinski, R., & Klein, U. 1985, Nature, 317, 697

Shibata, K. 1989, in IAU Symp. 136: The Center of the Galaxy, ed. M. Morris (Dordrecht: Kluwere), 313

Shopbell, P. L., & Bland-Hawthorn, J. 1998, ApJ, 493, 129

Shore, S. N., & LaRosa, T. N. 1999, ApJ, 521, 587

Sofue, Y. 1985, PASJ, 37, 697

Sofue, Y. 2000, ApJ, 540, 224

Sofue, Y. 2003, PASJ, 55, 445

Sofue, Y., & Handa, T. 1984, Nature, 310, 568

Sofue, Y., & Reich, W. 1979, A&A, 38, 251

Stolovy, S., et al. 2006, J. Phys. Conf. Ser., 54, 176

Strickland, D. K., & Stevens, I. R. 2000, MNRAS, 314, 511

Tsuboi, M., et al. 1986, AJ, 92, 818

Uchida, K. I., Morris, M., & Serabyn, E. 1990, ApJ, 351, 443

Uchida, K. I., Morris, M., Serabyn, E., & Bally, J. 1994, ApJ, 421, 505

Uchida, Y., Sofue, Y., & Shibata, K. 1985, Nature, 317, 699

Veilleux, S., Cecil, G., & Bland-Hawthorn, J. 2005, ARA&A, 43, 769

Wang, Q. D., Gotthelf, E. V., & Lang, C. C. 2002, Nature, 415, 148

Williams, R. E., & Christiansen, W. A. 1985, ApJ, 291, 80

Yusef-Zadeh, F. 1989, in IAU Symp. 136: The Center of the Galaxy, ed. M. Morris, (Dordrecht: Kluwere), 243

Yusef-Zadeh, F., & Knigl, A. 2004, in ASP Conf. Ser. 322, Formation and Evolution of Massive Young Star Clusters, ed. H. J. G. L. M. Lamers, L. J. Smith, & A. Nota (San Francisco: ASP), 201

Yusef-Zadeh, F., & Morris, M. 1987a, ApJ, 322, 721

Yusef-Zadeh, F., Hewitt, J., & Cotton, W. 2004, ApJS, 155, 421

Yusef-Zadeh, F., Morris, M., & Chance, D. 1984, Nature, 310, 557

Yusef-Zadeh, F., Morris, M., Slee, O. B., & Nelson, G. J. 1986, ApJ, 310, 689